Distribution Agreement

In presenting this thesis or dissertation as a partial fulfillment of the requirements for an advanced degree from Emory University, I hereby grant to Emory University and its agents the non-exclusive license to archive, make accessible, and display my thesis or dissertation in whole or in part in all forms of media, now or hereafter known, including display on the world wide web. I understand that I may select some access restrictions as part of the online submission of this thesis or dissertation. I retain all ownership rights to the copyright of the thesis or dissertation. I also retain the right to use in future works (such as articles or books) all or part of this thesis or dissertation.

Signature:

_____

Savannah J. Johnson Date

AMYLOID CONFORMATIONAL DIVERSITY ACCESSED BY TRUNCATIONS OF A NATIVE PROTEIN FOLD

By

Savannah J. Johnson
Doctor of Philosophy
Chemistry

_____

Dr. David G. Lynn
Advisor

_____

Dr. R. Brian Dyer
Committee Member

_____

Dr. Stefan Lutz
Committee Member

Accepted:

_____

Lisa A. Tedesco, Ph.D.
Dean of the James T. Laney School of Graduate Studies

_____ Date

AMYLOID CONFORMATIONAL DIVERSITY ACCESSED BY TRUNCATIONS OF A NATIVE PROTEIN FOLD

By

Savannah J. Johnson

B. S., Piedmont College, 2008

Advisor: David G. Lynn, PhD.

An abstract of

A dissertation submitted to the Faculty of the

James T. Laney School of Graduate Studies of Emory University

in partial fulfillment of the requirements for the degree of

Doctor of Philosophy

in Chemistry

2012

Abstract

Amyloid Conformational Diversity Accessed By Truncations of a Native Protein Fold

By Savannah J. Johnson

Neurodegenerative diseases have gained more attention in the last decade due in part to advances in genomic information, structural definition and imaging technology. The development of devastating neurodegenerative conditions, such as Alzheimer's disease (AD), is associated with the deposition of amyloid fibers and neuronal apoptosis. These fibers are predominantly comprised of the amyloid β peptide, Aβ(1-42), and its truncations, Aβ(1-40) and Aβ(1-39). Recently, Aβ amyloid formation in retinal diseases such as glaucoma and macular degeneration have been shown to eventually lead to neuronal cell death and subsequent irreversible blindness, and recent data has correlated an increase in development of glaucoma or macular degeneration of patients with AD. Although many theories have been postulated regarding the true cause of these retinal diseases, including increased intra-ocular pressure and oxidative stress resulting in mitochondrial damage and the release of cytochrome c, the relationship between AD and glaucoma has only recently been investigated. Genomic studies of patients with the most common form of glaucoma has shown that mutations in three particular genes highly expressed in the ocular tissues (optineurin, myocilin, and WDR36) result in pre-glaucomatous conditions that degrade the optic nerve over time. WDR36 has a membrane-bound β-propeller and, similar to the well-known signal transduction associated β-propeller

G-protein, each propeller blade is made of a repeating WD-unit that folds into a β-meander composed of four strands. My hypothesis is that β-propeller structures, such as the β subunit of the G Protein and WDR36, provide a nucleation site for converting the Aβ peptide into amyloid fibers resulting in damage to retinal ganglion cells. Here, I show that subunits and β-strand fragments of the β-propeller fold modulate the morphology Aβ(16-22), the nucleating core of the amyloid β peptide, allowing for the self-assembly of diverse conformations. These observations may provide insight to both the tissue-specificity of amyloid strains as well as the heterogeneous nature of the amyloid deposits found in the disease state. Understanding sequence contributions and having the ability to control the morphology and dimensions of self-assembling peptide nanostructures has relevance to disease etiology, development of therapeutics and the design of future bio-inspired nanomaterials.

AMYLOID CONFORMATIONAL DIVERSITY ACCESSED BY TRUNCATIONS OF A NATIVE PROTEIN FOLD

By

Savannah J. Johnson

B. S., Piedmont College, 2008

Advisor: David G. Lynn, PhD

A dissertation submitted to the Faculty of the

James T. Laney School of Graduate Studies of Emory University

in partial fulfillment of the requirements for the degree of

Doctor of Philosophy

in Chemistry

2012

For Mom and Dad

Acknowledgements

I am greatly indebted to my advisor, Dave, for teaching me the importance of teaching and inspiring others. He has always patiently challenged me both in the lab and in life, encouraging me to learn and grow, and I will forever appreciate his enthusiasm, good humor and great humility. I appreciate the feedback given by my committee members, Stefan Lutz and Brian Dyer, as well as from my unofficial committee member, Vince Conticello. I have benefited greatly from our scientific discussions. Virginia Shadron has been an amazing friend and colleague throughout my graduate career, and I am lucky to have had her company even after her retirement.

Lingfeng "Kitty" Liu was the first person to make time for me at Emory, and I am grateful for her kindness. Her friendship made my transition to grad school more enjoyable. Through her, I was able to meet Seth Childers, a great lab mate and friend. I will always be thankful for their excitement for science and for their friendship when I needed it the most. I have also been very lucky to work with Anil Mehta, a stellar teacher and an insightful scientist. Special thanks to Anil for his review of my thesis and helpful feedback. Seth and Anil taught me many lab techniques, but their most helpful moments were talking me through thought experiments over coffee. Without their friendship and encouragement, I may have chosen to leave graduate school long ago. I was also very fortunate to know Rong Ni, Yi-Han Lin, Yue Liu and Phoebe Young, who made coming to lab a true pleasure.

Chenrui Chen has been a remarkable friend and science sister—we have been through so much together, and I would not trade a single moment that I have had with her. I know that much joy and happiness is in store for her! Many thanks to my bench mate, Tolu Omosun, for her unabashed honesty, loyalty and true friendship. I have enjoyed sharing in our many adventures together. Dibyendu Das has always been able to cheer me with his optimism and I am glad to have him as a colleague and friend. Lisa Li has been a great help to me, and I have benefited from her strength and friendship. I have learned as much from her as she has from me. Junjun Tan, Lisa Li and Chenrui Chen are great officemates and I have enjoyed our time together. Special thanks to friend Neil Anthony from Physics for teaching me about fluorescence microscopy and British rhyming slang. The Lynn lab is a special place thanks to Jay Goodwin, Li Zhang and Ting "Fish" Pan working their synthetic black magic. I have enjoyed working with the new members of Team Peptide—Rolando Rengifo, Chen Liang and Alexandra Brosius. I look forward to your future discoveries!

Special thanks to Lakshmi Anumukonda for integrating me into her high school class for several semesters and letting me flex my teaching muscles. She is a great inspiration to me. I am grateful to Shaoxiong Wu for letting me be the NMR service instructor. His infectious energy and great sense of humor make him a great asset to our department. Thanks to Hong Yi and Jeanette Taylor for helping with my microscopy and diffraction experiments. Fred Strobel, Ken Hardcastle, John Bacsa, Patti Barnett and Steve Krebs have been instrumental in making my science happen. I would also like to acknowledge my previous advisors for their support and

encouragement—Luther Elrod, Sean Carrigan, and Tim Lytle from Piedmont College; Jeff Urbauer from the University of Georgia; Stéphane Petoud from the University of Pittsburgh and Beat Meier at ETH-Zürich. I am grateful to Irena Mamajanov, Betül Arslan and Sara Walker for introducing me to astrobiology and for being very enthusiastic about their science. I would not have made it through the last few years without good friends Ana Alcaraz, Gordon Wells, Amy Dalton, Uliana Danilenko and Valarie Truax.

My greatest gratitude is for my amazingly fearless, artistic, and whimsical parents for their endless support, love and encouragement each and every day. Everything good I have done has its ultimate source in their teaching me to love learning new things and connecting with ideas and people. Finally, my life would be a much darker place without the joy and love that my dog, Normand, brings to me as my shadow and best friend.

Table of Contents

List of Figures

Chapter 1

Chapter 2

Chapter 3

Chapter 4

Chapter 5

Chapter 6

Chapter 7

List of Tables

Abbreviations

Aβ	amyloid-β
AD	Alzheimer's disease
AFM	atomic force microscopy
APP	amyloid precursor protein
Arg	arginine
CD	circular dichroism
CHCA	Cyano-4-hydroxycinnamic acid
CR	Congo red
DCC	N,N'-dicyclohexylcarbodiimide
DCM	dichloromethane
DIPEA	N,N-diisopropylethylamine
DMF	dimethylformamide
DMSO	dimethyl sulfoxide
EDT	1,2-ethanedithiol
FMOC	9-fluorenylmethoxycarbonyl
FRET	fluorescence resonance energy transfer
FT-IR	Fourier Transform Infrared Spectroscopy
GPB1	G Protein Blade 1
GPBS	G Protein Beta Subunit

H-bond	hydrogen-bond
HBTU	2-(1H-Benzotriazol-1-yl)-1,1,3,3-Tetramethyl Uronium hexafluorophosphate
HFIP	hexafluoroisopropanol
HPLC	high-performance liquid chromatography
IE-IR	isotope-edited FT-IR
Lys	lysine
MALDI-TOF	matrix assisted laser desorption ionization - time of flight mass spectrometry
MD	molecular dynamics
min	minute
mM	millimolar
mL	milliliter
PrP	Prion Protein
Rho110	Rhodamine 110
RP-HPLC	reversed-phase high-performance liquid chromatography
SELDI	surface-enhanced laser desorption/ionization
SEM	scanning electron microscopy

STEM	scanning and transmission electron microscopy
TEM	transmission electron microscopy
TFA	trifluoroacetic acid
TLC	thin layer chromatography
UV	ultra-violet
μL	microliter
μM	micromolar

Chapter 1

Protein Misfolding and Amyloid Tissue Specificity

Self-Assembly is a Hallmark of Living Systems

Biomolecules utilize a variety of chemical interactions and recognition elements to organize into their functional networks. DNA and RNA rely on base-pairing and stacking to transfer information digitally with high fidelity. Lipids self-assemble by clustering hydrophobic regions to create a bilayer capable of serving as a container for other cellular components as well as allowing or preventing the diffusion of small molecules into and out of the system. Proteins serve as catalysts, transforming and maintaining populations of raw materials, and also as scaffolds for the organization and maintenance of many cellular functions. The many combinations of secondary and tertiary protein folds afford a wide variety of quaternary units that can interchange depending on the required function.

Protein folding is a highly orchestrated process that depends on both inter- and intra-molecular forces and, in some cases, the assistance of protein-folding chaperones. α-helices and β-sheets comprise the majority of protein secondary structure in nature. β-sheets, in particular, have been highlighted due to their involvement in certain diseases, such as Alzheimer's and Parkinson's. When a protein misfolds or is partially digested to a less stable form, it can interact with itself or other peptides to form intracellular aggregates. The cell can use enzymes to digest smaller aggregates or push them into the extracellular environment, but some aggregates cause detrimental effects leading to apoptosis or cell death (Markesbery

1997; Wirths, Multhaup et al. 2004; Lee, Zhu et al. 2006). Peptide aggregates that hydrogen-bond into extended β-sheets and laminate to one another can form fibrils with an ordered cross-β structure, where cross-β refers to the perpendicular diffraction lines formed when the fibrils are analyzed using X-ray or electron diffraction (Wormell 1954; Eanes and Glenner 1968; Sunde, Serpell et al. 1997; Nelson, Sawaya et al. 2005). These cross-β aggregates are called amyloids and have been implicated in the development of neurodegenerative diseases such as Alzheimer's.

In efforts to develop methods to detect and treat Alzheimer's disease, lab-produced amyloids formed *in vitro* have been shown not to recapitulate the toxicity of the aggregates formed within the brain (Podlisny, Stephenson et al. 1992; Meyer-Luehmann, Coomaraswamy et al. 2006). Though the amyloid β peptide is expressed ubiquitously throughout the body, its deposition is much higher within neurons in the brain(Verdier, Zarándi et al. 2004). The family of amyloid diseases has recently been expanded with the finding that proteins specific to other tissue types can also misfold into amyloid and are correlated with disease, such as Parkinson's disease (Conway, Harper et al. 2000), Huntington's disease (Scherzinger, Sittler et al. 1999; McGowan, van Roon-Mom et al. 2000), Type II diabetes (Höppener, Ahrén et al. 2000; Hull, Westermark et al. 2004) and amyotrophic lateral sclerosis (Kolde, Bachus et al. 1996; Elam, Taylor et al. 2003). These findings suggest that protein misfolding and amyloid self-assembly is greatly dependent on the tissue type and the cellular environment.

Glaucoma: An Ocular Amyloidosis

As previously discussed, protein misfolding into amyloid can lead to cell death and there are many diseases that share the cross-β amyloid structure, though the originating misfolded protein may differ (Soto 2003). This family of misfolded proteins includes prions in diseases such as Cruetzfeld-Jacobs, amyloid β in Alzheimer's disease plaques, and, most recently, the aggregates found in the eye in several ocular diseases (Surguchev and Surguchov 2010). Glaucoma and glaucoma-related diseases are the leading cause of blindness worldwide and as many as half of those affected remain undiagnosed for many years. Glaucoma is a disease of the optic nerve and is often associated with increased intraocular pressure due to poor flow of the aqueous humor through the trabecular meshwork of the eye, a situation which can place added stress on the nerve (Kwon, Fingert et al. 2009)(**Figure 1-1**).

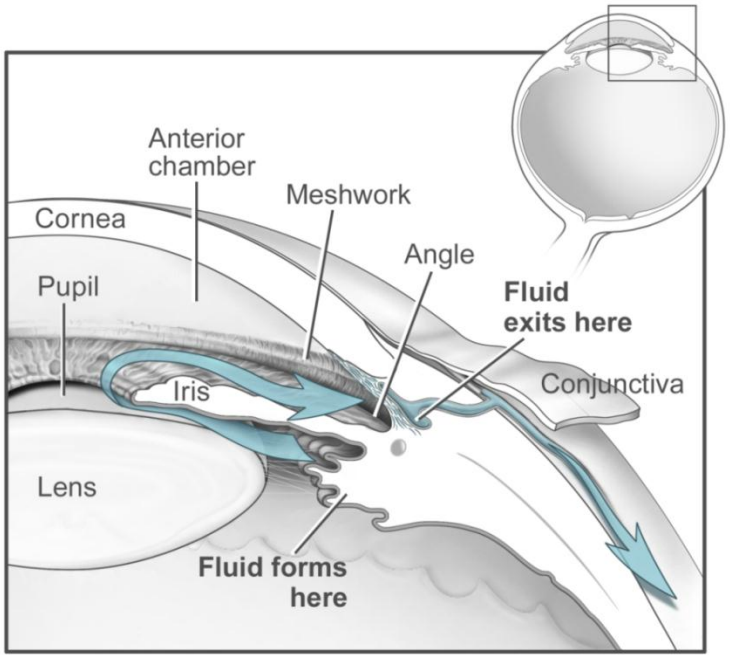

Figure 1-1. Schematic of the interior of the eye showing normal flow of fluid out of the trabecular meshwork (TM). In glaucomatous eyes, the TM is blocked by aggregates, increasing pressure on the optic nerve. Courtesy: National Eye Institute, National Institutes of Health (NEI/NIH). (NIH)

The aqueous humor is constantly being replaced in normal eyes and increased fluid buildup can cause irreversible blindness in some patients (Band, Hall et al. 2009). Currently, loss of vision cannot be restored and the typical treatments require a lifetime of medications, eye drops, and, in some cases, advanced laser surgeries, to maintain a healthy intraocular pressure. For these reasons, much work has been done recently in attempts to elucidate the role of genetic mutations in proteins associated with the development of this disease (Yin 2008). Amyloidogenic

aggregates have been recorded in multiple cases of glaucoma and some ophthalmological researchers now refer to glaucoma as ocular amyloidosis (Nelson, Edward et al. 1999; Surguchev and Surguchov 2010) (**Figure 1-2**).

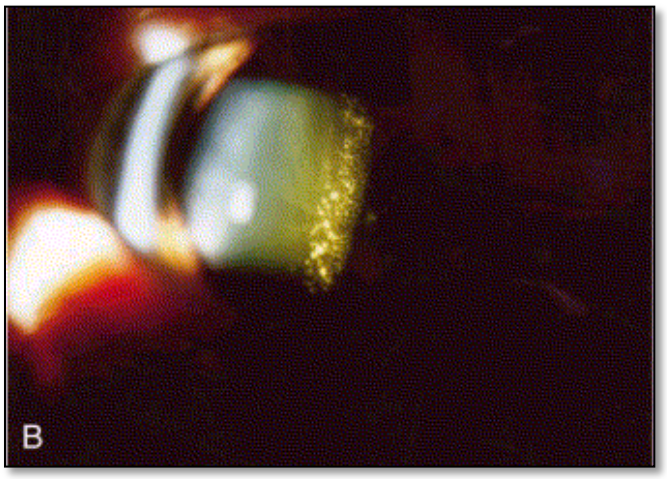

Figure 1-2. A slit-lamp photograph showing extensive fibrillar amyloid deposits seen over the anterior lens surface. (Nelson, Edward et al. 1999)

Plaques removed from the lenses of glaucoma patients were composed of the amyloid β peptide, also found in the neuronal plaques of Alzheimer's patients (Bayer, Keller et al. 1999; Nelson, Edward et al. 1999; Goldstein, Muffat et al. 2003) (**Figure 1-3**). These plaques can be stained with Congo Red, a common histological dye used to identify amyloid structure, and form fibrils visible by transmission electron microscopy, though they are heterogeneous (Nelson, Edward et al. 1999).

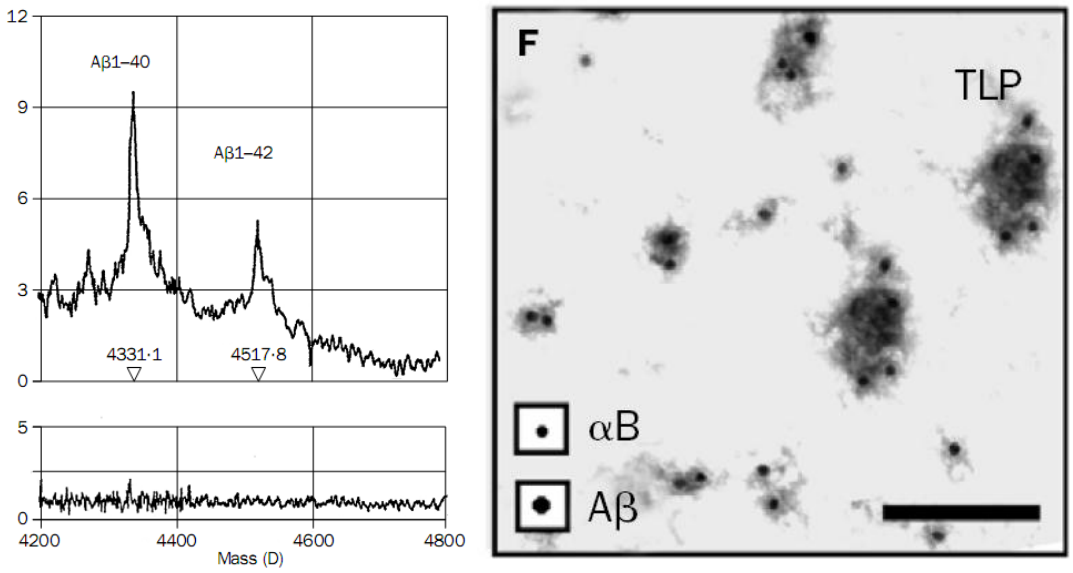

Figure 1-3. (Left) Anti-Aβ SELDI mass spectrometry of human lens extract showing that the amyloid β peptide is a major component of the aggregates removed from the lenses of glaucoma patients. (Right) Total lens protein extracted from the plaques forms heterogeneous protofibril aggregates and bind anti-Aβ coated nanoparticles in an immunogold electron microscopy experiment (black dots are nanoparticles). Scale bar=100nm. (Goldstein, Muffat et al. 2003)

When these lens aggregates were analyzed, they were shown to be much less toxic in cell assays than the amyloid extracts acquired postmortem from Alzheimer's patients (Goldstein, Muffat et al. 2003; Guo 2007). This difference in toxicity may be due in large part to the two aggregates having two distinct amyloid conformations. These differences in conformation would likely be influenced by the environment of the peptide as it is assembling into the fibrils. The physiological environments of the eye and the brain are quite similar, with optic neurons and brain neurons having a near

identical cellular morphology, pH and salt distribution (Chesler 2003). There are dramatic differences, however, in the types of genes upregulated and proteins expressed in these two cell types (Balaratnasingam, Morgan et al. 2009).

Due to it being the only organ in the body not protected by a layer of skin, the eye is constantly assaulted by UV irradiation. Because of this, the cells in the optic tissue have evolved many defenses, including being able to produce and quickly utilize antioxidant small molecules as well as housing an army of proteins dedicated solely to capturing reactive oxygen species (Carper, Sun et al. 1999; Akpek and Gottsch 2003; Shamsi, Chaudhry et al. 2007; Lassen, Black et al. 2008). Other proteins that are much more common in the eye also include those responsible for repairing damaged biopolymers (both nucleic acids and proteins) and degrading nonfunctional proteins that have misfolded (Akpek and Gottsch 2003; Surguchev and Surguchov 2010). Due to the cellular environments of the eye and the brain having very different proteome compositions, I considered whether the interactions of amyloid β with specific native protein folds unique to each cell type could play a role in the differing morphologies and relative toxicities of the final aggregates. Specifically, I predicted that the great propensity of amyloid-β to form β-sheet aggregates would make it likely to interact with proteins containing preorganized β-sheets within their structures. Little is known about how the amyloid-β peptide interacts with other proteins as the plaques are typically heterogeneous and difficult to analyze (Miller, Papayannopoulos et al. 1993). Some proteins may interact nonspecifically with the amyloid after it has already formed a fibril, but others may

interact with the amyloid monomers or oligomers to provide a nucleating site for the propagation of amyloid aggregates with new conformations.

Amyloid Assembly is Context Dependent

For reasons not entirely known, under the right conditions, proteins can assemble into amyloid (Chiti and Dobson 2009) and certain misfolded proteins have been correlated with damage to certain types of cells (Carrell RW 1997). The development of drugs and therapeutics to combat this aggregation has been difficult due to the heterogeneous nature of amyloid plaques. Investigations of peptide sequences derived from amyloid β, which forms fibril aggregates around neurons, reveal that metal-ion binding and small molecule interactions may tune the toxicity of the fibrils, suggesting ion levels in different types of cells may induce a more toxic fibrillar arrangement (Dong 2007; Ryu, Girigoswami et al. 2008; Hindo, Mancino et al. 2009).

To understand formation of these misfolded amyloid aggregates, previous studies have been focused on discerning the pathway of the formation of highly-ordered cross-β structure from peptide monomers. This process of assembly has several intermediate steps: upon an increase in local concentration peptides cluster together to exclude water and create molten globule aggregates (also referred to in the literature as oligomers or particles) (Kayed, Head et al. 2003; Glabe 2006; Cheon, Chang et al. 2007; Fawzi, Ying et al. 2010). These oligomers are proposed to serve as environments where the peptide can desolvate and transition into a more ordered

crystalline β-sheet arrangement that templates the addition of monomer (Liang, Guo et al. 2008; Childers, Anthony et al. 2012). There has been debate as to which of these structures is the most toxic in AD, but recent evidence suggests that oligomers themselves are as toxic, if not more toxic, than the fibrils (Glabe 2006; Cheon, Chang et al. 2007; Haass and Selkoe 2007; Yin, Chen et al. 2008; Laganowsky, Liu et al. 2012).

Crystalline-phases within the aggregates form in a nucleation-dependent manner wherein there is a lag phase after the monomers associate and before the elongation of the fibrils from the β-sheet nucleus (Harper and Lansbury 1997; Stine, Dahlgren et al. 2003; Hellstrand, Boland et al. 2009). This lag phase can be bypassed by addition of a nucleating species which serves as a template (Lomakin 1996; Cruz, Urbanc et al. 2005; Lazo, Grant et al. 2005; Shorter 2005; Hills and Brooks 2007; Linse, Cabaleiro-Lago et al. 2007; Liang, Lynn et al. 2010) (**Figure 1-4**).

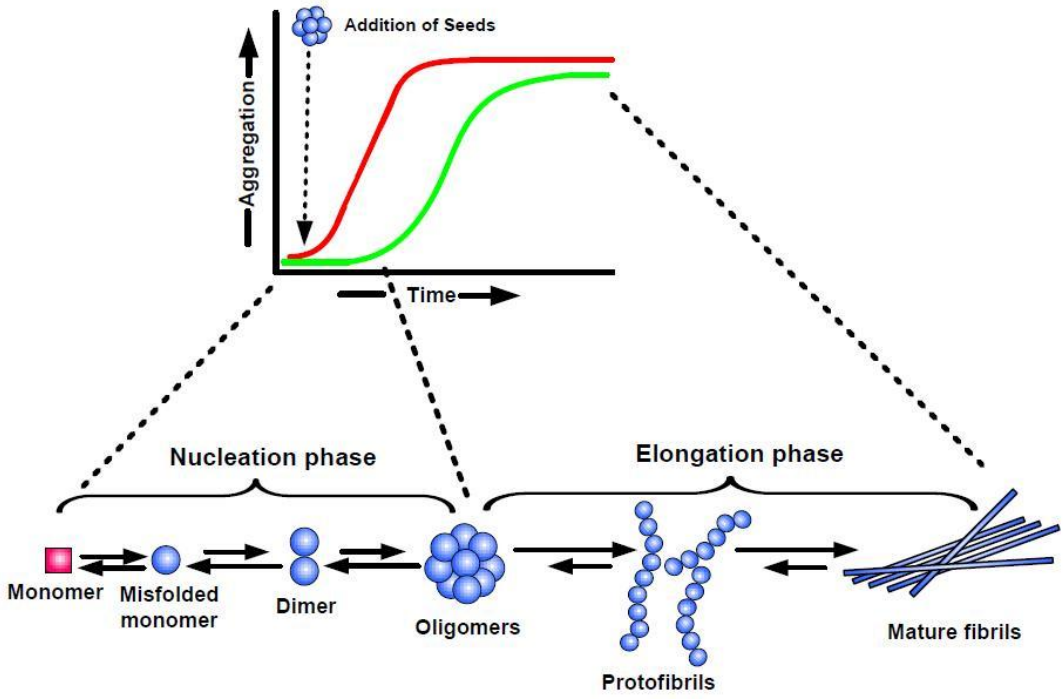

Figure 1-4. Amyloid self-assembly is a nucleation-dependent process. Fibers form only after lag phase in reactions that are not seeded (green). By contrast, fibers form rapidly without a lag phase upon addition of preformed nuclei (red). (Kumar 2011)

The nucleation, or seeding, of amyloid structures has been studied extensively. Addition of short preformed fibers can initiate fiber growth bypassing the lag phase (**Figure 1-4**). Surface interactions, including air-solvent, metal and interactions at lipid membranes, can significantly change both the pathway of the assembly and the conformation of the structures formed (Giacomelli and Norde 2005; Ryu, Girigoswami et al. 2008; Evers, Jeworrek et al. 2009). Interactions such as these have the potential to alter the nucleus, which may also lead to a change in the final structure.

The amyloid β peptide found in Alzheimer's plaques aggregates contain both the full-length, Aβ(1-42), as well as 1-40 and 1-39 truncations. Through mutational studies the region most crucial for nucleation of the assembly was found between amino acids 13-22, with the minimum nucleating species being residues 16-22 (Wurth, Guimard et al. 2002). Aβ(16-22), Ac-KLVFFAE-NH_2, is able to assemble into fibril structures at neutral pH that are morphologically similar to those formed by the full-length amyloid β peptide (Balbach, Ishii et al. 2000; Mehta, Lu et al. 2008) (**Figure 1-5a**). Aβ(16-22) fibrils have been extensively characterized using multiple biophysical techniques and are composed of antiparallel in-register β-sheets that hydrogen-bond along the long axis of the fibril which then laminate together through side chain interactions, which contributes to the width of the structures (Liang, Pingali et al. 2008; Mehta, Lu et al. 2008). When the peptide is allowed to incubate in acidic conditions, it assembles into hollow peptide nanotubes with extended β-sheet lamination (Lu, Jacob et al. 2003; Mehta, Lu et al. 2008) (**Figure 1-5b**).

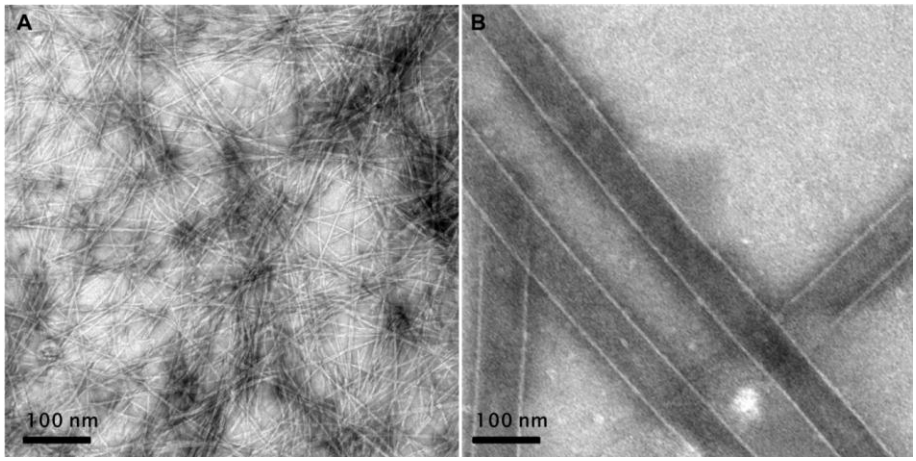

Figure 1-5. TEMs of 2mM Ac-KLVFFAE-NH_2 which forms fiber when incubated at neutral pH (a) and nanotubes at acidic pH (b).

The sheets helically coil to form tubes with the H-bonds of the β-sheets running at an angle of 23° (**Figure 1-6**). The extended lamination of the β sheets in the tubes is due to the change in peptide registry to antiparallel out-of-register, to better accommodate the packing of Val-Ala and Phe-Phe residues(Liang, Pingali et al. 2008; Mehta, Lu et al. 2008). The transition to nanotubes is accomplished by protonation of the Glu22 and breaking of the stabilizing salt-bridge that is formed with the Lys16 of the adjacent peptide. The breaking of the salt bridge can also be accomplished by replacing the V18 side chain with a t-butyl group, forcing the peptides to adopt an antiparallel out-of-register conformation even at neutral pH (Liang, Pingali et al. 2008). By making an E22L mutation, the peptide assembles into nanotubes with an antiparallel out-of-register arrangement and this nanotube formation is pH independent. Our current knowledge is consistent with in-register antiparallel or parallel β-sheets always self-assembling into a fibril morphology and out-of-register antiparallel β-sheets forming nanotubes (Kun Lu, Thesis 2005) (**Figure 1-6**).

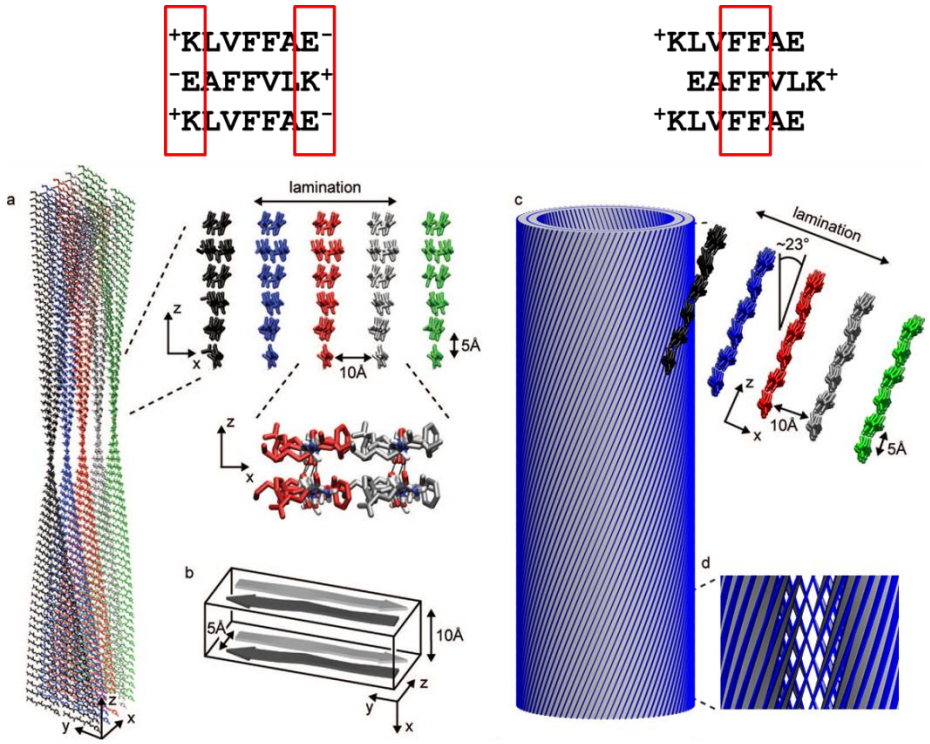

Figure 1-6. Cartoons of Aβ(16-22) fibril formed at neutral pH (left) and nanotube formed under acidic conditions (right) showing hydrogen bonding in the z-axis and lamination of side chains in the x-axis. Side chains have been omitted for clarity. (Mehta, Lu et al. 2008)

Based on atomic force microscopy (AFM) and small-angle X-ray scattering (SAXS) data, the wall thickness of the nanotubes was determined to be 4nm, which corresponds to the distance of two peptides (2nm long) stacked end-to-end (Lu, Jacob et al. 2003; Mehta, Lu et al. 2008). This data, along with solid-state NMR data, show that the peptides in the tubes are arranged into a bilayer similar to a lipid membrane (Childers, Mehta et al. 2010). It has been shown that other chemical moieties can be covalently attached to the peptide and are incorporated into the

structures (Dong, Lu et al. 2006; Childers, Anthony et al. 2012; Ni, Childers et al. 2012). These results demonstrate that even for the short, seven-residue peptide, Aβ(16-22), morphology is context-dependent. Due to the simplicity of the sequence in comparison to Aβ(1-40), structural analyses allow for direct correlation between amino acid composition, morphology and environment. Its ease of synthesis and the critical role that Aβ(16-22) plays in nucleation of the full-length amyloid β peptide have made it a very useful model system for examining the peptide-peptide interactions critical to structural and morphological changes in amyloid assembly.

By covalently attaching a fluorophore to the N-terminus of the peptide, it has been shown that the assembly process can be followed and the ends of the tube can be located spatially with fluorescence microscopy (Liang, Guo et al. 2008; Liang, Lynn et al. 2010) (**Figure 1-7**).

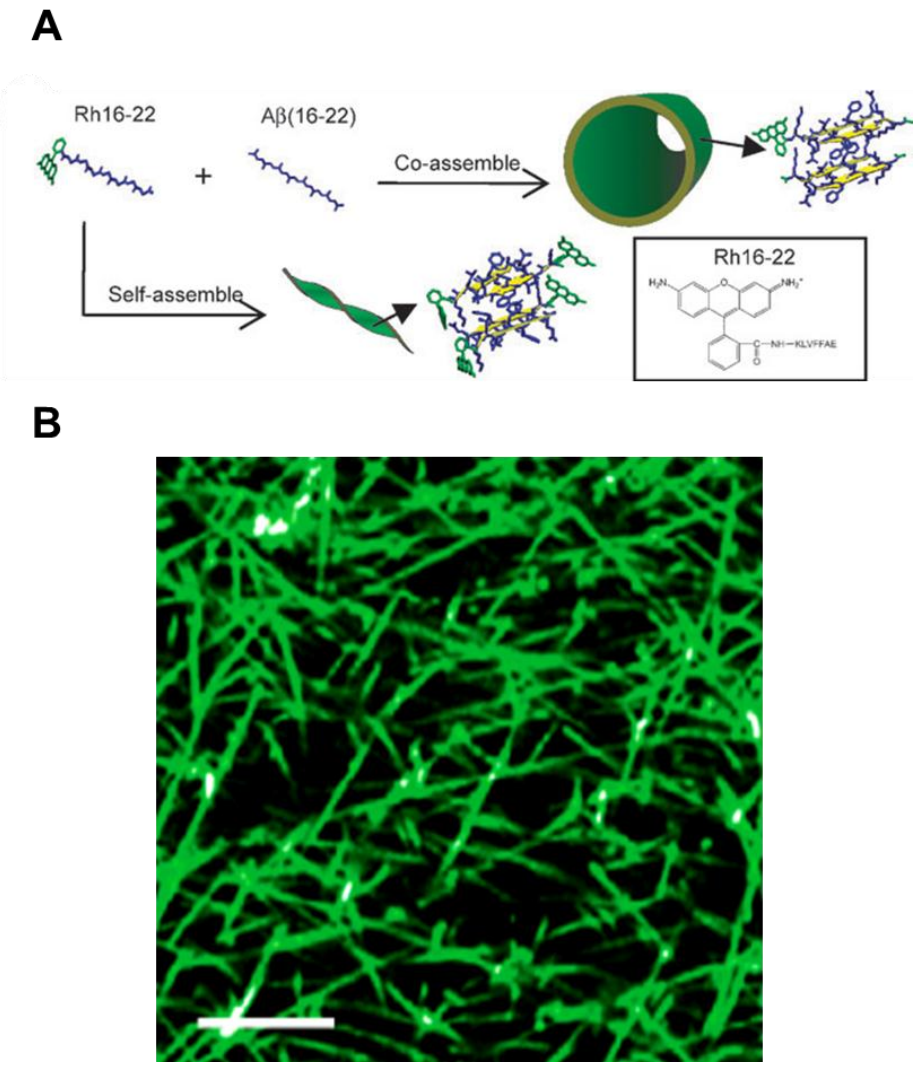

Figure 1-7. (a) Schematic of Rhodamine 110 labeled Aβ(16-22) coassembled with unlabeled Aβ(16-22) to allow for visualization of the nanotubes by fluorescence microscopy. (b) Tubes of Aβ(16–22):Rh16–22 co-assembly at 250:1 molar ratio, and λ_{ex} = 780 nm. Scale bar=10μm. (Liang, Lynn et al. 2010)

The ability of the labeled peptide to be incorporated into the peptide nanotube demonstrates that the assembly has plasticity and can accommodate heterogeneity

while still maintaining long-range order. The equilibrium that exists between monomer and the assembled structure can be tuned in a variety of ways and is reversible over measurable timescales (Childers, Anthony et al. 2012). Thus, amyloid assembly is influenced to a great extent by the environment and its conformation can differ greatly from one set of conditions to another. The assemblies can be heterogeneous, which may be caused by unique cellular environments, providing insight into the tissue specificity of the amyloid plaques and differences in their relative toxicities.

These aggregates form in a nucleation-dependent process wherein the peptide monomers need a template to organize into the cross-β fold. The pathway from monomer to aggregate is context-dependent and can be affected by pH, small molecules, air-solvent interfaces and surfaces, giving rise to a wide variety of possible conformations. In this thesis, I have asked whether amyloid β assembly might be nucleated by protein folds that are specific to the eye into a different conformation, which may help to explain why these aggregates have lower toxicity. By investigating the possible interactions between amyloid β and these native folds, I have developed a model and a new mechanism of amyloid nucleation that may provide insight to the great diversity of amyloid conformations and potentially their tissue-specific toxicity.

Chapter 2

Models of a Glaucoma-Related β-Propeller Fold

Introduction

Given the correlation between amyloid plaques and neuronal death in the brains of Alzheimer's patients, amyloid β aggregates have been analyzed using methods such as size-exclusion chromatography in an attempt to isolate the most toxic agent within the plaques (Glenner and Wong 1984; Masters 1985; Prelli, Castano et al. 1988; Iwatsubo, Odaka et al. 1994). This has proven to be quite challenging because the plaques are made up of a variety of cellular components, possibly due to the immune response of the cells trying to degrade the large structures. It has been hypothesized that the aggregates can grow long enough to puncture the cell's membrane, leading to apoptosis (Verdier, Zarándi et al. 2004; Engel, Khemtémourian et al. 2008) or that the fibrils can sequester small molecules or metals to produce reactive oxygen species (Dong, Lu et al. 2006; Dong, Canfield et al. 2007). There are also reports that the fibrils are not the toxic species, but that the oligomers are the most detrimental to the cell and that their toxicity is mitigated when they transition into fibrils (Kim 2003; Glabe 2006; Ferreira, Vieira et al. 2007; Sakono and Zako 2010).

Regardless of which form is the most toxic, the fibrils in the plaques have been shown to be primarily composed of amyloid β peptide with a combination of other proteins, such as proteoglycans, proteases and proteins used in copper

homeostasis, as well as metals, lipids and even nucleic acids (Miller, Papayannopoulos et al. 1993) (**Figure 2-1**).

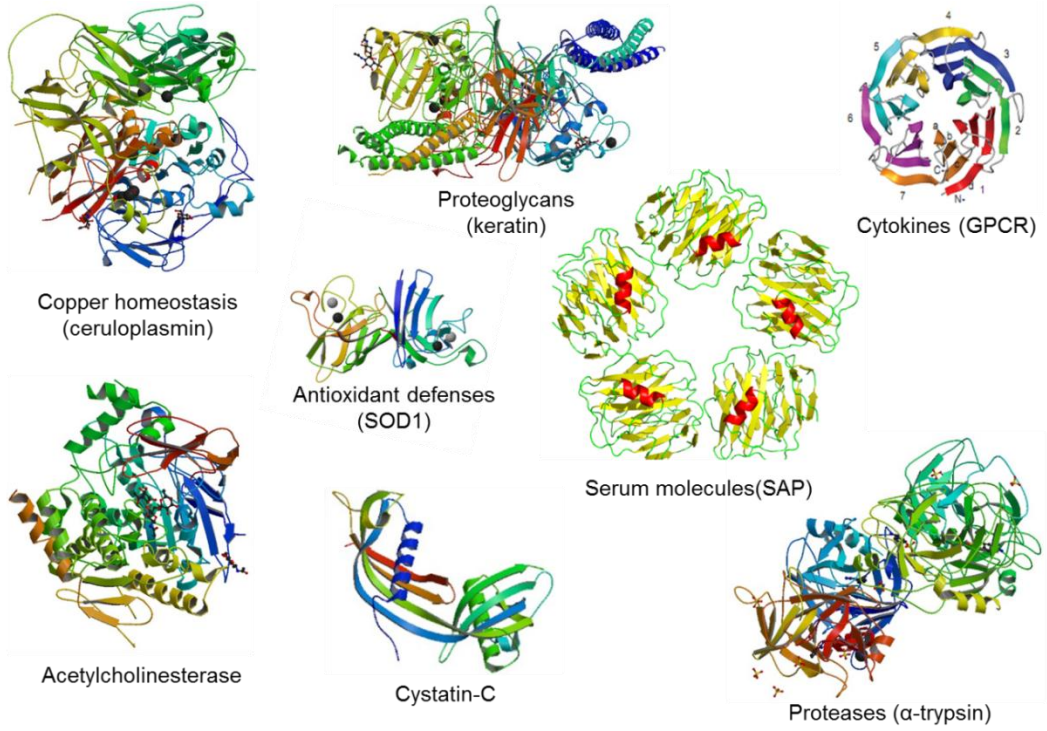

Figure 2-1. Proteins commonly found in amyloid plaques from Alzheimer's disease brain homogenate (Miller, Papayannopoulos et al. 1993).

In an attempt to alleviate stress on the cell, it has been proposed that cytokines and proteases are recruited to destroy the amyloid peptides and possibly get trapped on its hydrophobic surface rather than functioning as they would with typical misfolded proteins that are more soluble and globular (Ishii, Haga et al. 1975; Meda, Baron et al. 1999; Gitter, Boggs et al. 2000; Strohmeyer and Rogers 2001). The interactions with these proteins is postulated to occur after the amyloid

aggregates have already begun to assemble into their fibril form (Miller, Papayannopoulos et al. 1993; Iwatsubo, Odaka et al. 1994), but very little is known about the interactions of the monomeric or oligomer forms of amyloid β with native protein folds.

In the context of amyloid aggregates found in the eyes of glaucoma patients, there are several protein risk factors that could potentially interact with amyloid β. Human genetic screens have identified several proteins with mutations that are correlated with an elevated incidence of glaucoma disease including myocilin (MYOC), optineurin (OPTN) and WDR36 (WDR36 gene) (Stone, Fingert et al. 1997; Rezaie, Child et al. 2002; Monemi, Spaeth et al. 2005; Nakano, Ikeda et al. 2009). Both myocilin and optineurin affect the severity of primary open-angle glaucoma (POAG), the most common form of the disease, though their functions and their involvement in the disease state remains under investigation (Libby, Gould et al. 2005). Of these, the most well-studied is myocilin (Tamm 2002; Nagy 2003; Fautsch, Vrabel et al. 2006), a highly-expressed 55-57kDa glycoprotein in the human trabecular meshwork that surrounds the lens of the eye. Mutations in myocilin correlate with slower clearance of the protein, resulting in higher intraocular pressure (Jacobson, Andrews et al. 2001; Tamm 2002). Mutations in optineurin correlate with normal-tension glaucoma, a less common variant of the disease. Indeed these mutations were found in individuals without glaucoma, suggesting that optineurin is primarily a modifier of the disease onset and severity (Rezaie, Child et al. 2002; Alward, Kwon et al. 2003; Libby, Gould et al. 2005).

WDR36, or WD repeat domain 36, which also appears to be a modifier of the disease (Hauser, Allingham et al. 2006; Hewitt, Dimasi et al. 2006; Miyazawa, Fuse et al. 2007) is expressed as a 100kDa monomer containing a guanine nucleotide-binding WD40 repeat, a reductase-like domain, an AMP-dependent synthase/ligase, and a Utp21-like WD40 repeat (Monemi, Spaeth et al. 2005). Studies in zebrafish have shown that this protein is critical for rRNA processing, is involved in nucleolar stability and accumulates in highest levels in the eye and central nervous system (Skarie and Link 2008). Loss of the WDR36 homologue in zebrafish results in activation of the p53 stress-response pathway, disruption in nucleolar morphology and RNA processing. Mutations in WDR36 can cause functional defects in a yeast system (Footz, Johnson et al. 2009), and cause disruption in retina homeostasis in a POAG mouse model (Chi, Yasumoto et al. 2010), both thought to be due to the destabilization of the hydrogen-bonding network that is key to keeping the WD40 domain properly folded. This WD40 β-propeller domain appears to be vital to the stability of the protein and to its function, which led me to investigate this fold in more detail.

The proteins in the WD40 repeat family have β-propeller tertiary folds. The propellers can contain multiple blades that contain four antiparallel β-strands each (**Figure 2-2**).

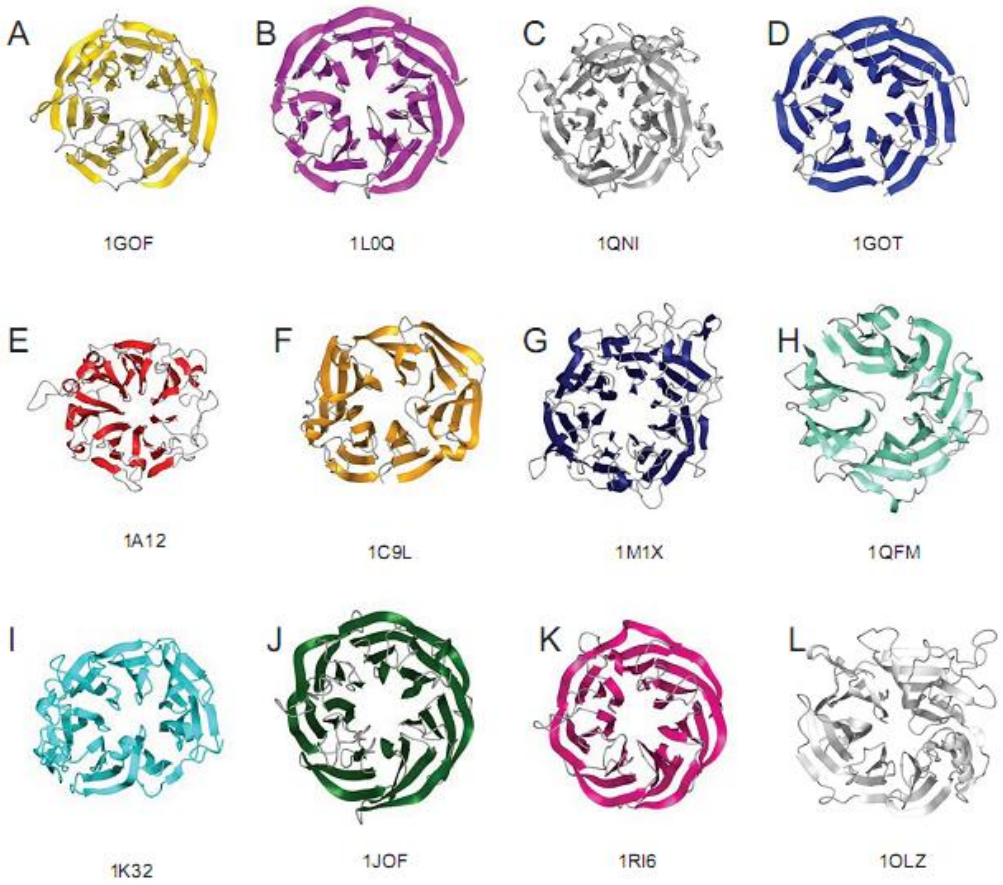

Figure 2-2. Representative members of the WD repeat family of β-propellers, including the β subunit of the G Protein Coupled Receptor (D) (Valeyev, Downing et al. 2008).

This family of proteins provide unique docking sites for multiple protein complexes involved in cell signaling (Fülöp and Jones 1999; van Nocker 2003; Chen, Spiegelberg et al. 2004; Nikkhah, Jawad-Alami et al. 2006; Schuetz, Allali-Hassani et al. 2006; Chaudhuri, Söding et al. 2008). As discussed in Chapter 1, amyloid fibers are detected in the ocular cavity of patients with glaucoma and, so I hypothesize that mutations in one or all of the proteins (myocilin, optineurin and WDR36) result in

destabilization of the native protein fold and provide a template for amyloid β assembly. With no structure available for the WDR36 protein, I have used homology modeling to predict the structure, properties and conformational changes of this protein upon mutation (Footz, Johnson et al. 2009; Chi, Yasumoto et al. 2010). In this chapter, I have created homology models of the three major proteins implicated in glaucoma using established homology modeling protocols and demonstrate that the β-propeller is destabilized by mutations that may allow it to form a more conformationally-flexible surface that may interact with the Aβ peptide.

Results

Building Homology Models of Proteins Implicated in Glaucoma

A set of homology models were produced for optineurin (OPTN), myocilin (MYOC/TIGR), and WDR36 using HHPred (http://toolkit.tuebingen.mpg.de/hhpred). Homologues for each sequence were found using Basic Local Alignment Search Tool (BLAST) and the structural PDB information from the highest-scoring protein was used to thread the desired sequence through the PDB structure. This structure was then minimized and scored to evaluate how well the threaded sequence fit on the homologous protein scaffold. The percent identity varied depending on whether the entire sequence or truncations were used for the BLAST search. Their percent compositions are: OPTN (58.93% helical/2.08% extended/38.99% random coil), MYOC (33.73% helical/21.63% extended/44.64% random coil), and WDR36 (28.08% helical/48.16%

extended/23.76% random coil). Myocilin contains two conserved domains, one of unknown function that is present in many bacteria and another that is an Olfactomedin-like (OLF) domain. As the highest scoring sequence in the PDB for the full-length sequence had only 19.6% similarity, I chose to make a model for both the full-length (**Figure 2-3**) as well as the OLF domain that had a higher-scoring homologue with 29.6% similarity (E-value = 0.0049, 0.14) (**Figure 2-4**).

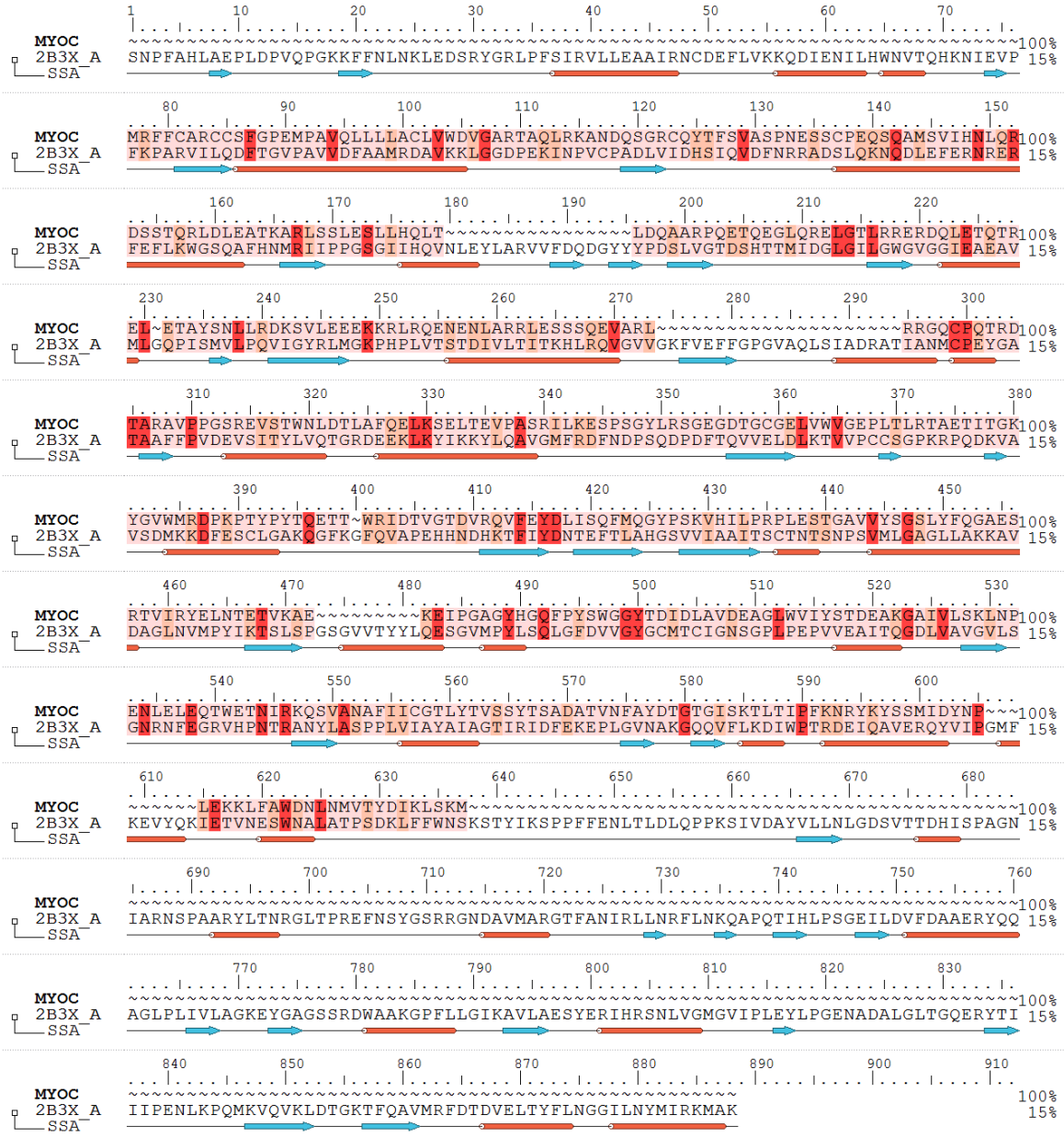
MYOC
2B3X_A
SSA
SNPFAHLAEPLDPVQPGKKFFNLNKLEDSRYGRLPFSIRVLLEAAIRNCDEFLVKKQDIENILHWNVTQHKNIEVP
MRFFCARCCSFGPEMPAVQLLLLACLVWDVGARTAQLRKANDQSGRCQYTFSVASPNESSCPEQSQAMSVIHNLQR
FKPARVILQDFTGVPAVVDFAAMRDAVKKLGGDPEKINPVCPADLVIDHSIQVDFNRRADSLQKNQDLEFERNRER
DSSTQRLDLEATKARLSSLESLLHQLT~~~~~~~~~~~~~~~~~LDQAARPQETQEGLQRELGTLRRERDQLETQTR
FEFLKWGSQAFHNMRIIPPGSGIIHQVNLEYLARVVFDQDGYYYPDSLVGTDSHTTMIDGLGILGWGVGGIEAEAV
EL~ETAYSNLLRDKSVLEEEKKRLRQENENLARRLESSSQEVARL~~~~~~~~~~~~~~~~~~~~~~RRGQCPQTRD
MLGQPISMVLPQVIGYRLMGKPHPLVTSTDIVLTITKHLRQVGVVGKFVEFFGPGVAQLSIADRATIANMCPEYGA
TARAVPPGSREVSTWNLDTLAFQELKSELTEVPASRILKESPSGYLRSGEGDTGCGELVWVGEPLTLRTAETITGK
TAAFFPVDEVSITYLVQTGRDEEKLKYIKKYLQAVGMFRDFNDPSQDPDFTQVVELDLKTVVPCCSGPKRPQDKVA
YGVWMRDPKPTYPYTQETT~WRIDTVGTDVRQVFEYDLISQFMQGYPSKVHILPRPLESTGAVVYSGSLYFQGAES
VSDMKKDFESCLGAKQGFKGFQVAPEHHNDHKTFIYDNTEFTLAHGSVVIAAITSCTNTSNPSVMLGAGLLAKKAV
RTVIRYELNTETVKAE~~~~~~~~~KEIPGAGYHGQFPYSWGGYTDIDLAVDEAGLWVIYSTDEAKGAIVLSKLNP
DAGLNVMPYIKTSLSPGSGVVTYYLQESGVMPYLSQLGFDVVGYGCMTCIGNSGPLPEPVVEAITQGDLVAVGVLS
ENLELEQTWETNIRKQSVANAFIICGTLYTVSSYTSADATVNFAYDTGTGISKTLTIPFKNRYKYSSMIDYNP~~~
GNRNFEGRVHPNTRANYLASPPLVIAYAIAGTIRIDFEKEPLGVNAKGQQVFLKDIWPTRDEIQAVERQYVIPGMF
~~~~~~LEKKLFAWDNLNMVTYDIKLSKM~~~~~~
KEVYQKIETVNESWNALATPSDKLFFWNSKSTYIKSPPFFENLTLDLQPPKSIVDAYVLLNLGDSVTTDHISPAGN
IARNSPAARYLTNRGLTPREFNSYGSRRGNDAVMARGTFANIRLLNRFLNKQAPQTIHLPSGEILDVFDAAERYQQ
AGLPLIVLAGKEYGAGSSRDWAAKGPFLLGIKAVLAESYERIHRSNLVGMGVIPLEYLPGENADALGLTGQERYTI
IIPENLKPQMKVQVKLDTGKTFQAVMRFDTDVELTYFLNGGILNYMIRKMAK
~~~~~~

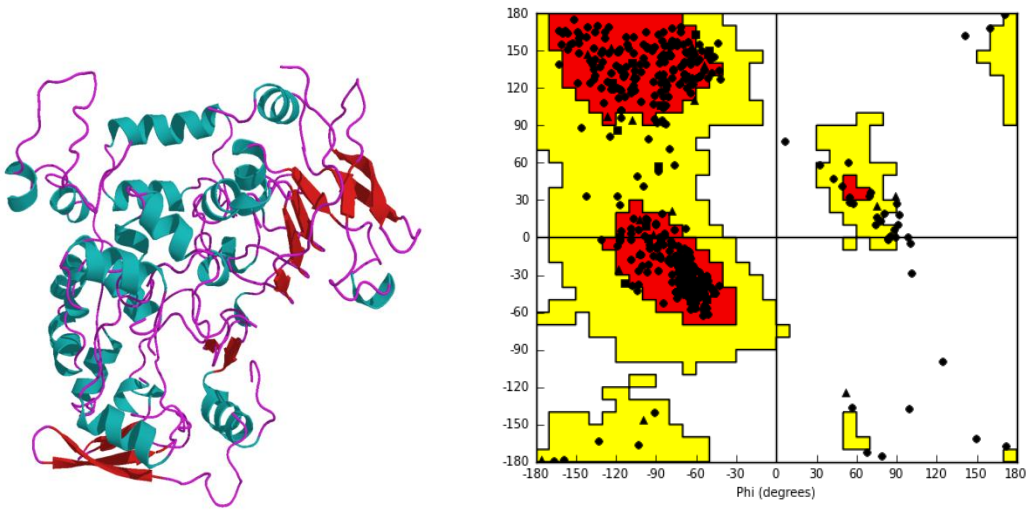

Figure 2-3. Myocilin full-sequence alignment (top), homology model from iron-responsive element binding protein 1 from *H. sapiens* (PDB# 2B3X) (left) and Ramachandran plot (right) showing mixture of α-helical and β-sheet character.

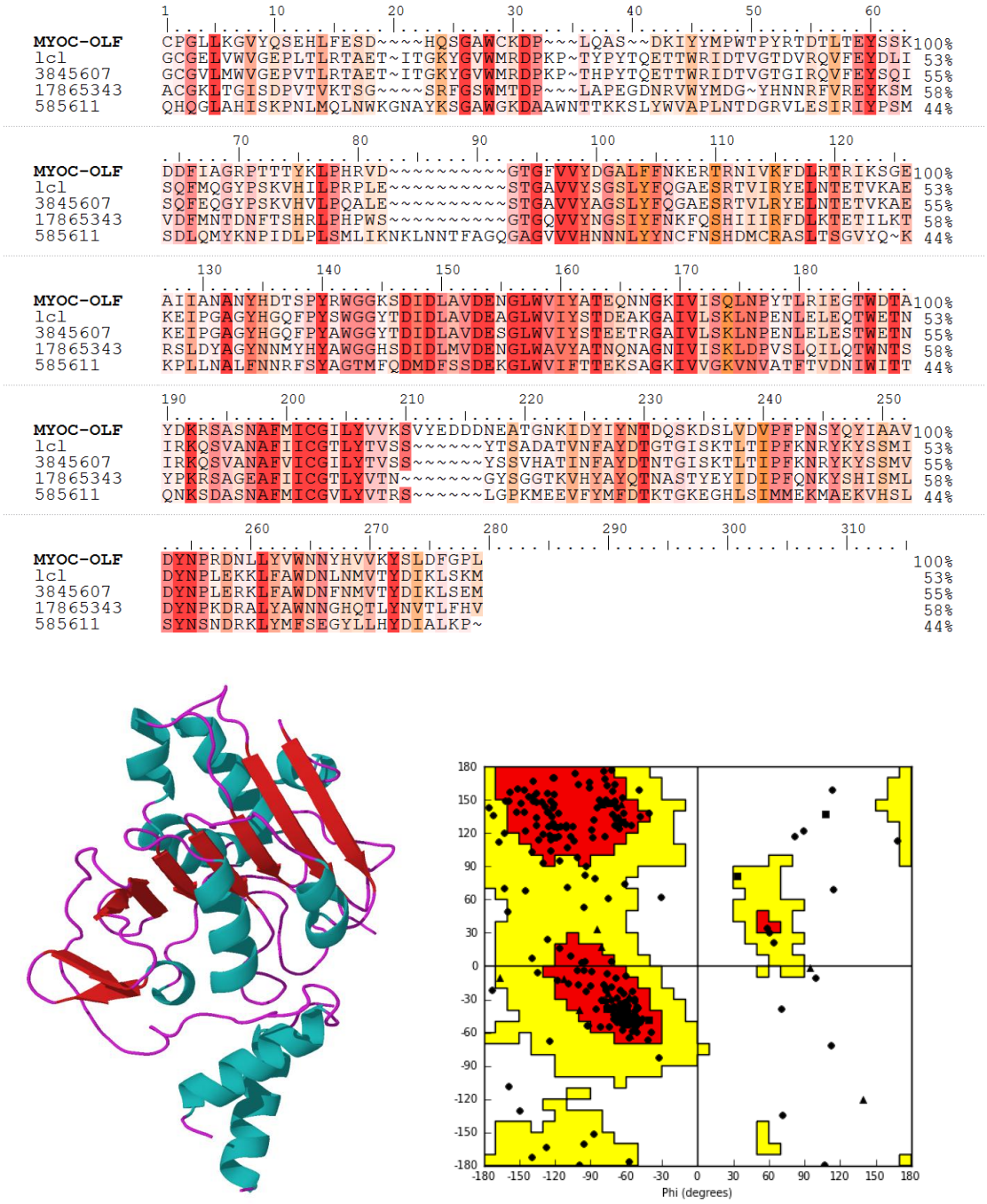

Figure 2-4. Alignment of the OLF domain of myocilin with highest-scoring homologues in the OLF domain family (top), homology model from MNMC2 from

Aquifex Aeolicus (PDB# 3VYW) (left) and Ramachandran plot (right) showing mixture of α-helical and β-sheet character.

For the optineurin sequence *E. coli* Colicin IA (PDB# 1CII) was identified as the highest-scoring structural homologue with 30.2% similarity (E-value = 0.18). Alignments were created for optineurin and Colicin IA to generate the structural model (**Figure 2-5**). Optineurin is proposed to be a membrane-embedded protein and the extended coil-coil shown in the model supports this hypothesis since it has two domains at either end that could function as sites for interactions with other proteins or small-molecules(Rezaie, Child et al. 2002; Bond, Peden et al. 2011).

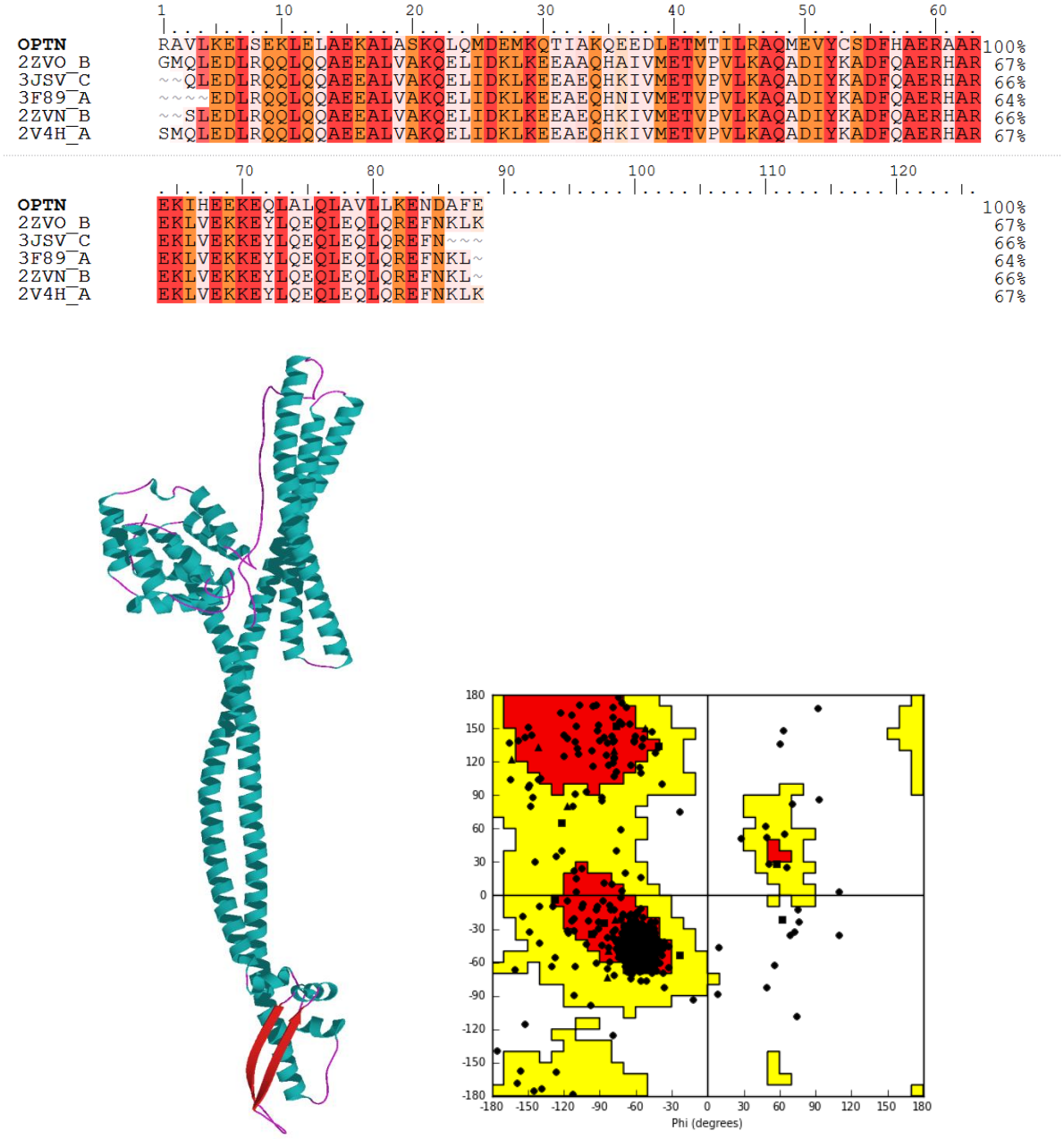

Figure 2-5. Optineurin alignments with highest-scoring homologues (top), homology model from Colicin IA from *E. Coli* (PDB# 1CII) (left) and Ramachandran plot (right) showing high degree of α-helical character.

Two homology models were constructed for the WDR36 protein based on full-length alignments and best partial alignment—one containing two β-propellers rotated by 90° with respect to each other and connected by a short coil (E-value = 8.2E-38) (**Figure 2-6**) from a sequence with 22.3% similarity, and another that contained only a single β-propeller (**Figure 2-7**) from a sequence with 27.4% similarity. Despite the discrepancy, it is clear that this protein contains at least one β-propeller domain and has a high percentage of β-sheet. For the following analyses, I use the double β-propeller model because the single propeller model left the remaining portion of the protein as a disorganized random coil, leading to difficulties in localizing ordered regions for further comparison.

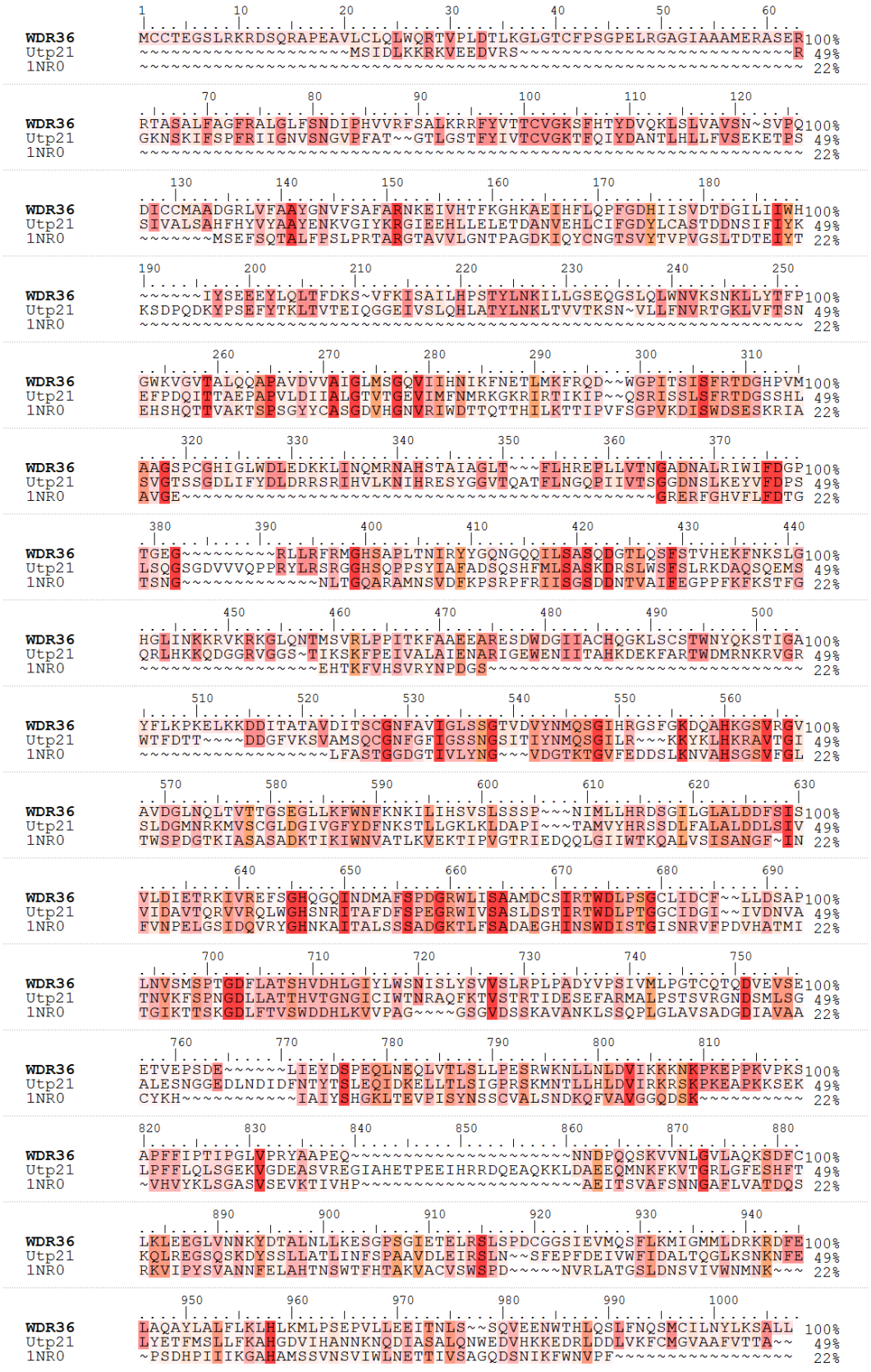
WDR36
Utp21
1NR0

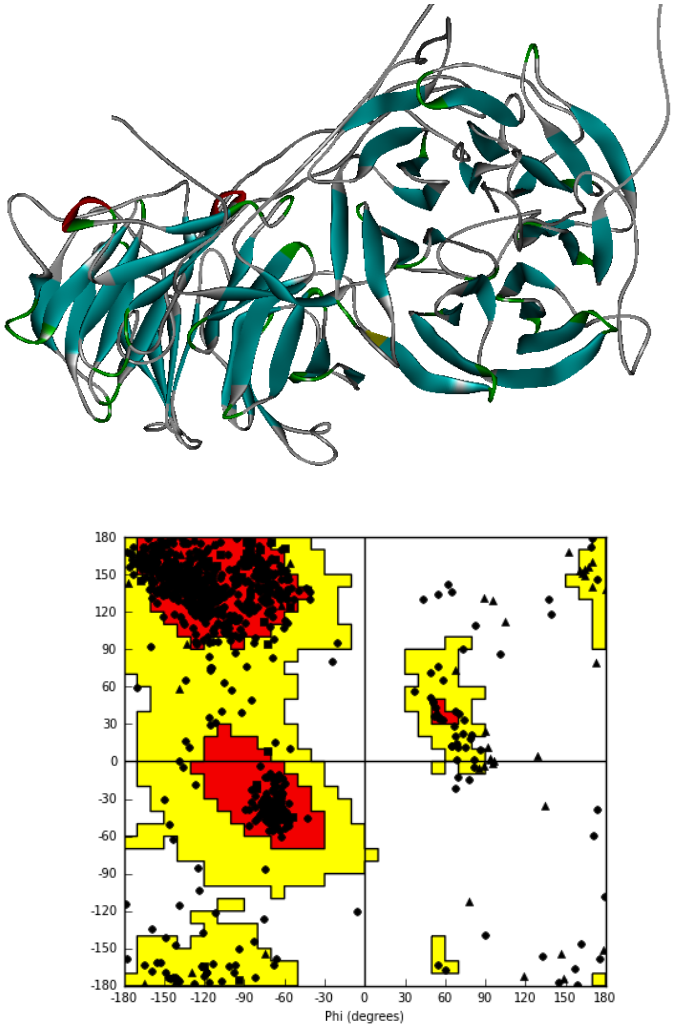

Figure 2-6. Sequence alignment of WDR36 with its closest homologue, Utp21 from yeast and AIP1 from *C. elegans* (top), homology model from AIP1 from *C. elegans* (PDB #1NR0) (middle) and Ramachandran plot (bottom) showing high degree of β-sheet character.

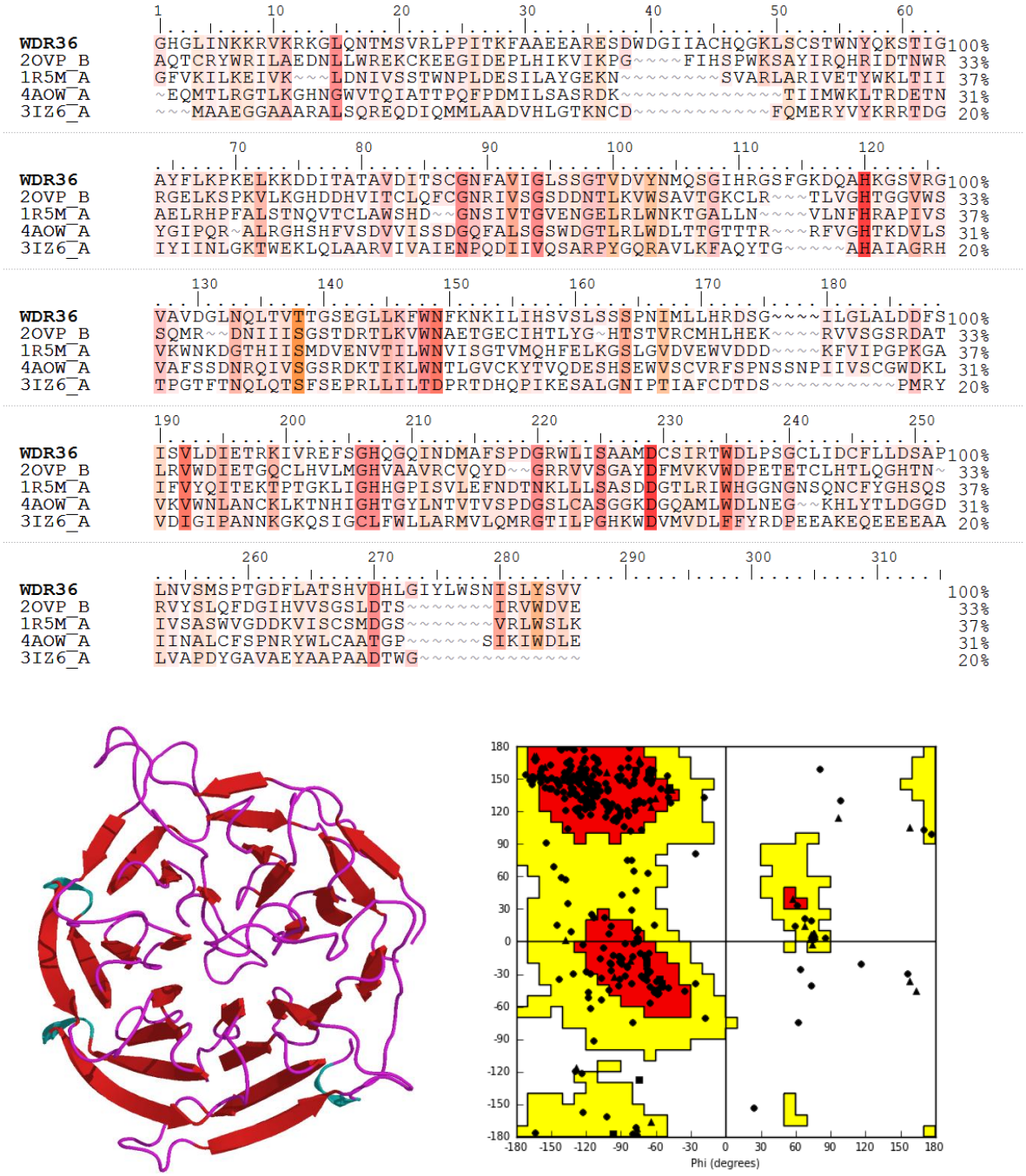

Figure 2-7. Sequence alignment of WDR36 with highest-scoring homologues with a PDB structure (top), homology model from the F-box/WD repeat protein 7 from *H. Sapiens* (PDB #2OVP) (left) and Ramachandran plot (right) showing high degree of β-sheet character.

The common feature used to characterize all amyloid is the arrangement of extended β-strands into a cross-β paracrystalline phase (Eanes and Glenner 1968; Sunde, Serpell et al. 1997). Based on this defining characteristic, I proposed that the likelihood of β-sheet rich folds, such as predicted in the WDR36 protein homology model, would serve as the best nucleating surfaces for the growth of β-sheet amyloid aggregates. Each blade of the β propeller in WDR36 is composed of four-stranded anti-parallel β sheets. These β sheets are connected to one another via connecting sequences. As shown in a representative β-propeller GPBS, the β strands are typically labeled A, B, C, and D (**Figure 2-8**) starting from the N-terminus to the C-terminus (from the center of the structure outward in a radial fashion).

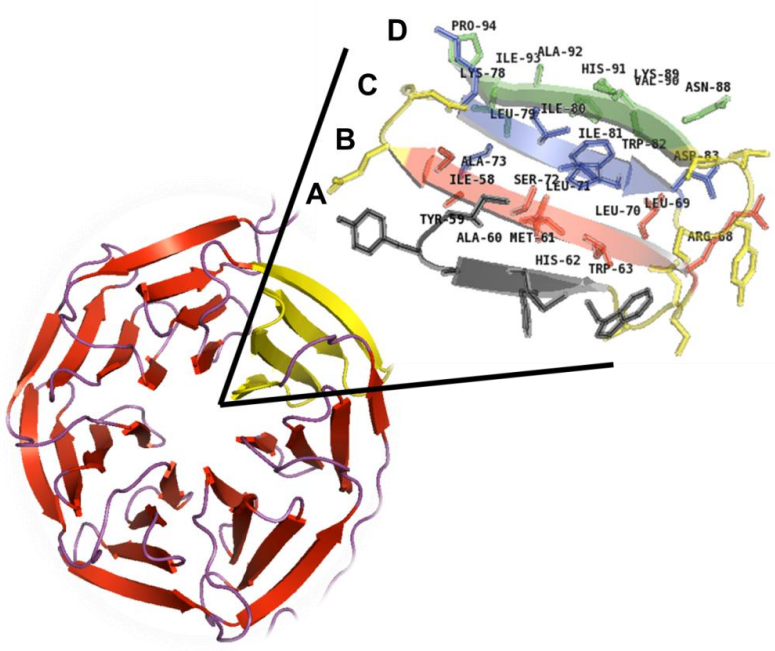

Figure 2-8. G Protein β-Subunit (GPBS: 1A0R) with blade in detail showing the common nomenclature for the strands of each β-sheet.

In many cases, the overall shape of the propeller takes on a funnel appearance and the sequences at the center of the blade interfaces are more hydrophobic than those in the center of the strands (**Figure 2-9**) (Gettemans 2003).

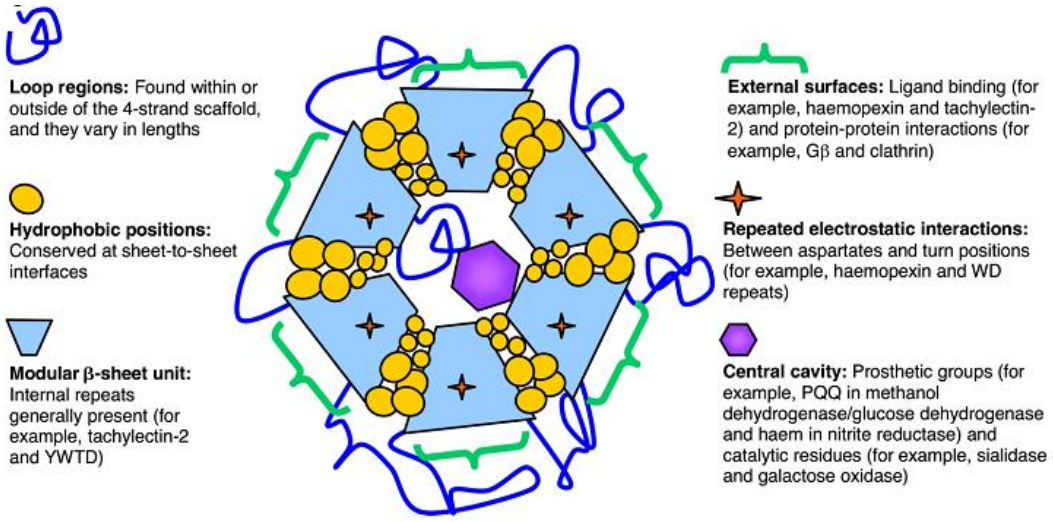

Figure 2-9. Conserved features of β-propellers of the WD40 repeat family(Gettemans 2003).

The length of strands A, B, and C are typically conserved in each blade of the propeller, but strand D is often of variable length, even among blades within the same propeller structure. This trait may have evolved to protect the outermost strand from undesirable edge-to-edge hydrogen-bonding interactions that may lead to protein aggregation and cell death(Fülöp 1999). There are many subfamilies within the superfamily of the β-propeller fold, including WD40 repeat, RCC1, kelch and others that share similar sequence motifs within their family blade portions. This fold presents an intriguing complexity of structure and diversity of function within a β-sheet rich scaffold that may serve as a preorganized template for the nucleation of amyloid β.

Homology within the β Propellers of G Proteins and WDR36 Model

As a model for studying possible interactions between β-propellers and amyloid β peptides, I also chose the crystal structure of the β-subunit from the ubiquitous G-protein coupled receptor (GPBS, PDB:1A0R), which is a well-characterized member of the WD40 repeat family of β-propellers that includes WDR36. This allowed me to distinguish β-strands from the surrounding random coil loops. The four antiparallel β-strands, delineated as A, B, C and D from the innermost to outermost strand in **Figure 2-8**, were aligned for each of the positions within the blade. Alignments were created for both the GPBS crystal structure and the WDR36 model and illustrated a greater diversity in the β strand sequences located in the outermost D strand positions. (**Figures 2-10 and 2-11**).

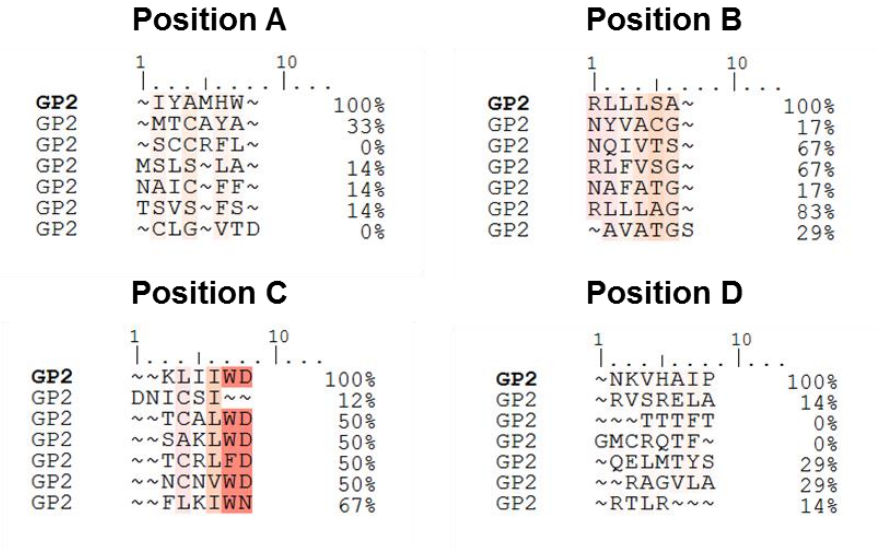

Figure 2-10. Alignment of the individual β strands from the G Protein B Subunit (GPBS) crystal structure with percent homology scoring based on the identity to the

top sequence. Color indicates regions of highest sequence similarity based on amino acid properties.

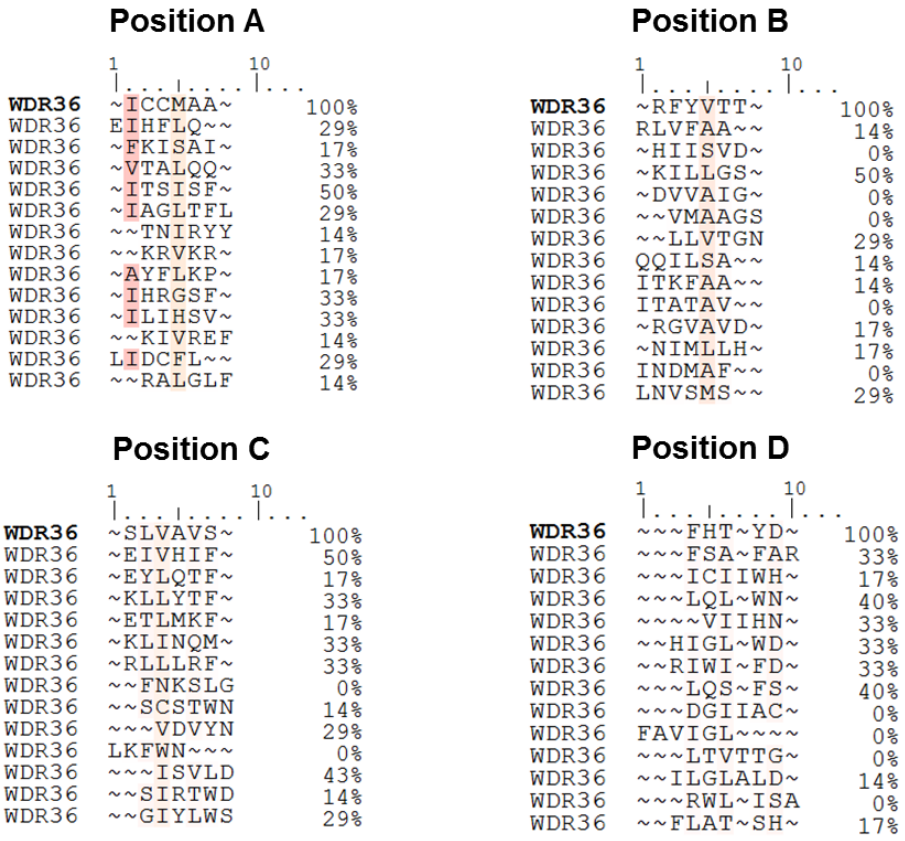

Figure 2-11. Alignment of the individual β strands from positions A, B, C and D of the double-bladed WDR36 homology model with percent homology scoring based on the identity to the top sequence. Color indicates regions of highest sequence similarity based on amino acid properties.

The A strand sequences from the GPBS typically had low homology between 14% and 33%, possibly due to the locations of residues in some sequences that have metal-coordinating functions, such as cysteine or histidine (**Figure 2-10**). The B strand sequences exhibited much higher homology up to 83% and usually contained a charged residue followed by an extended set of hydrophobic residues. The C strand sequences aligned quite well and had higher homology between 50-67% due to the WD-repeat found at the C-terminus of each strand, a characteristic that gives the name for this family of β-propellers (**Figure 2-10**). The conservation of the hydrophobic residues within the internal B and C strands may be important in stabilizing the core of the repeating blade units as they pack against the neighboring blade.

Alignments of all strands of the WDR36 double-bladed homology model were poor and showed very little sequence conservation regardless of their positions (**Figure 2-11**), which may be due to the low homology between the WDR36 sequence and the template used for threading (PDB #2OVP) (**Figure 2-7**). This was also true for the single-bladed WDR36 model. Given the ability for the sequences to form a β-propeller, the ability of the individual strands to aggregate was evaluated. Predictions were made for each set of sequences at positions A, B, C and D from GPBS, 10 crystal structures of members of the β-propeller family and the WDR36 homology model using the Aggrescan server, which uses sequence information from known aggregation-prone domains to calculate the likelihood of a particular sequence to aggregate (**Figure 2-12**). The aggregation propensity for each position was compared to the central nucleating core of the Aβ peptide, Aβ(16-22). As

discussed in Chapter 1, this peptide assembles into amyloid fibers at neutral pH (Balbach, Ishii et al. 2000).

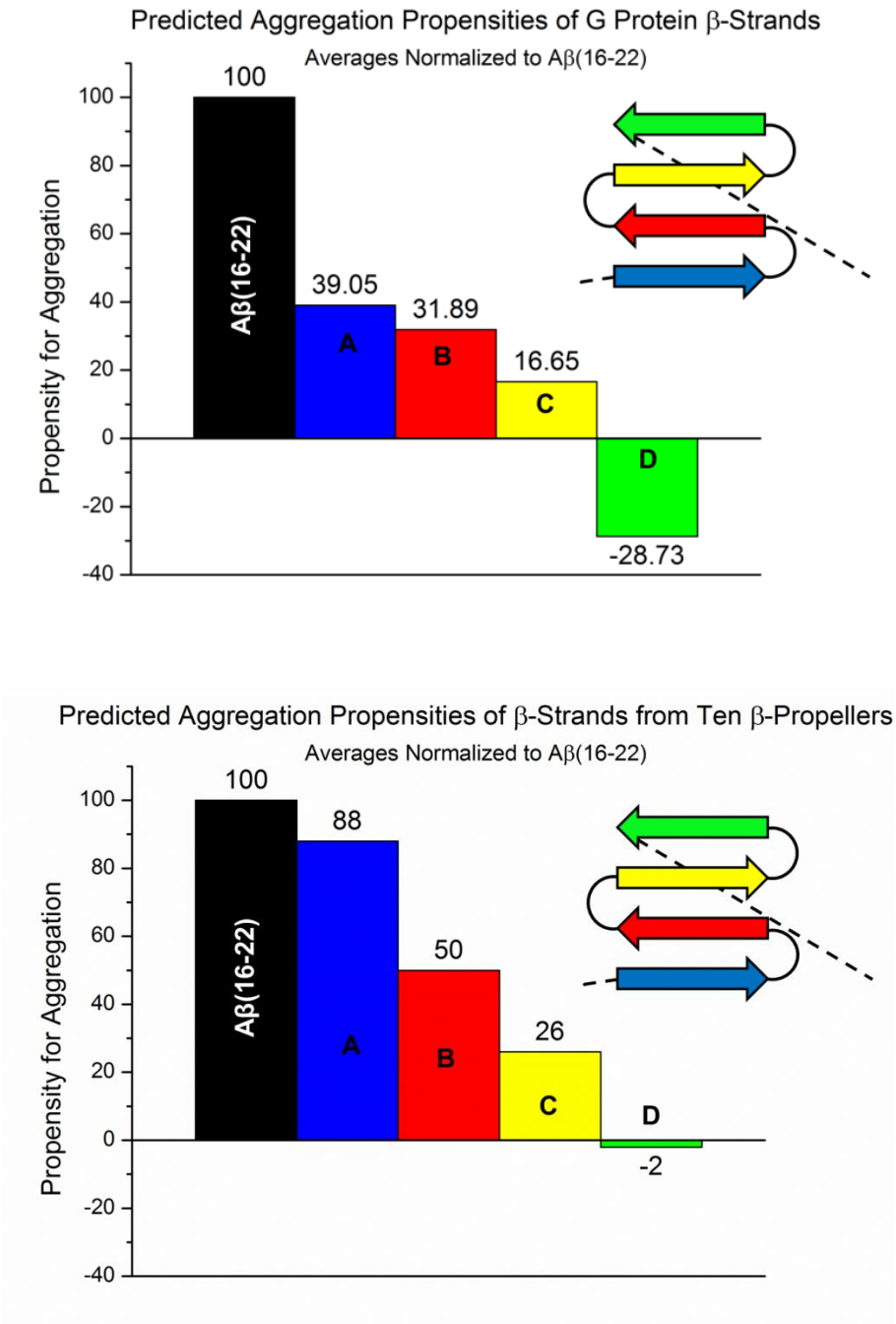

Figure 2-12. Aggrescan predicted aggregation propensities of (top) β-strands from the G Protein β-Subunit (PDB: 1AR0) and (bottom) aggregation propensities of β-

strands from PDB: 1TBG, 2TRC, 1ERJ, 1JV2, 2CE8, 1RI6, 3FGB, 3HXJ, 1DFC, 3C5M. Each column represents the average score for each set of A, B, C or D strands from each structure: sets of 7 strands for the 7-bladed GPBS and sets of 14 for the 14-bladed WDR36. Sequences used can be found in **Appendix I**.

The D strand sequences in GPBS had the lowest predicted aggregation propensities of all positions, possibly due to the high number of hydrophilic residues and prolines found within these sequences. Unlike the exposed D strands, the most internal A and B strand sequences had the highest predicted aggregation propensities, consistent with their hydrophobic sequence characteristics, though none scored as high as Aβ(16-22).

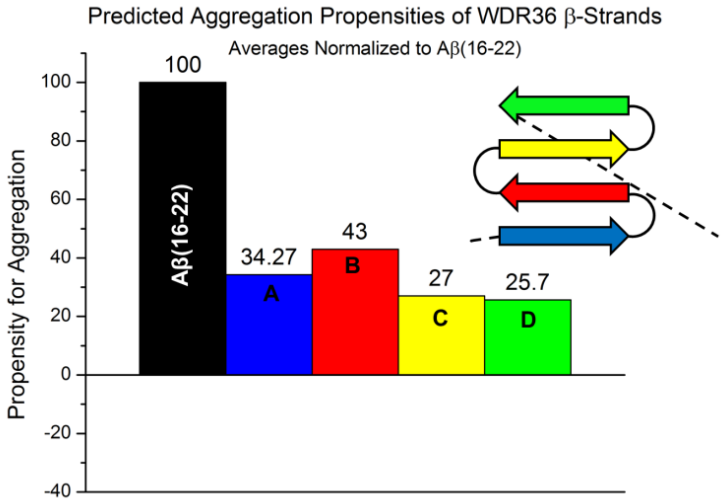

Figure 2-13. Aggrescan predicted aggregation propensities of the β-strands from the WDR36 double-bladed homology model. Each column represents the average score for each set of sequences in the A, B, C or D position from each sequence.

This pattern is consistent when the same procedure is repeated for ten other members of the β propeller family, with sets of strands being scored and averaged for each position (**Figure 2-12**). There is less distinction between the average scores for the sequences taken from different positions in WDR36 model (**Figure 2-13**). The clear outlier of the WDR36 homology model is the D strand aggregation propensity. This may be due to low template homology or the misalignment of the threaded sequence within the template crystal structure. However, WDR36 B and C strands have similar aggregation scores to the propellers in **Figure 2-12**. WDR36 strand A aggregation scores are quite different than the propellers in **Figure 2-12**, but similar to the score for the A strands in GPBS.

Mutations Destabilize the β-Propeller Fold

Using the double-bladed homology model for WDR36, the locations of disease-related mutations and their possible effects on the structural stability of the protein were investigated (**Figure 2-14**).

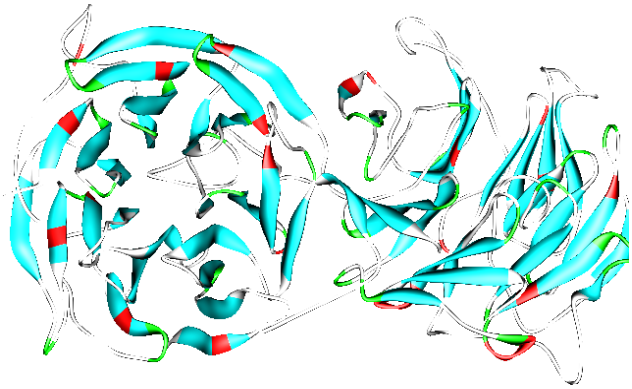

Figure 2-14. Double-bladed homology model of WDR36 with glaucoma-related mutations highlighted (red).

The mutations within this structure could lead to loss of function, as seen in the yeast homologue (Footz, Johnson et al. 2009), but could also cause loss of structural integrity by opening up the β-propeller, exposing hydrophobic β-sheet stretches that would normally be buried in the core of the structure. Though the mutations within our model seem to occur in both inner and outer β-strands, each of these could have a significant effect on the ability of the protein to maintain its compact fold (**Figure 2-15**).

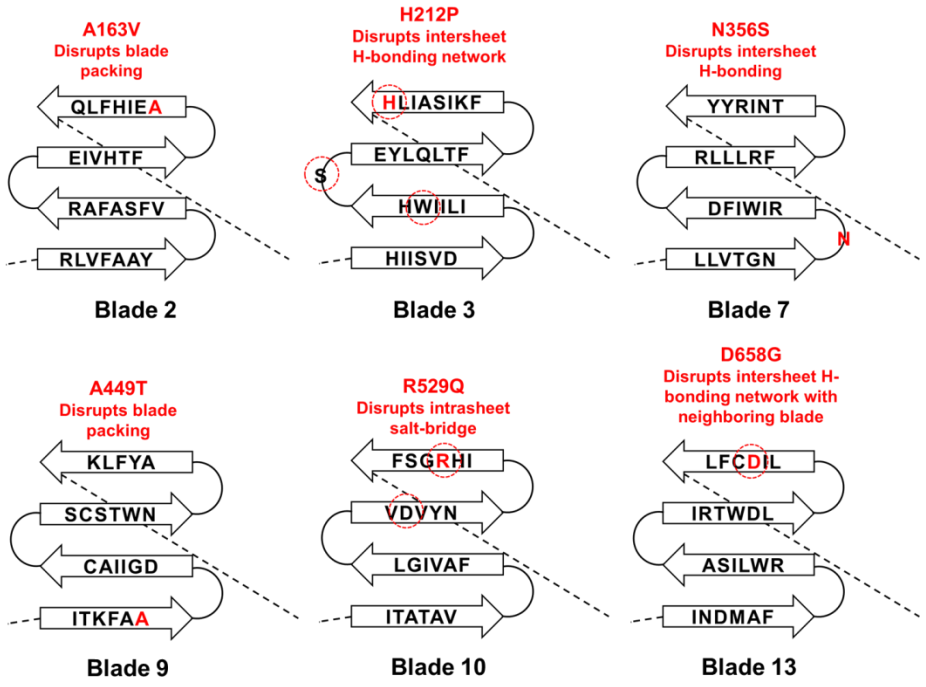

Figure 2-15. Locations of glaucoma mutations in the β-propeller WDR36 homology model and potential structural effects of their substitutions.

The interior of the β-propeller is tightly packed, with each blade within a few angstroms of the two adjacent blades, such that internal strand mutations from unbranched to branched amino acids (A163V or A449T) cause disruption in the blade packing of the model. Hydrogen bonding networks of side chains, typically Asp-His-Ser-Trp motifs or Asn, play important roles in stabilizing the tertiary structures of β-propellers (Wu, Chen et al. 2010; Wu, Zhang et al. 2010). Modifications that break this network (H212P, N356S, and D658G) greatly destabilize the folded structure in the model. Likewise, the loss of important interstrand electrostatic interactions would also affect the 'locking' of the β-strands

within the sheets, which could lead to the exposure of internal portions of the fold. Exposed regions may form extended β-strands that may serve as a template for the hydrogen-bonding of an exogenous β-sheet forming peptide, such as Aβ(1-42). This model and the positions of the disease-related mutations are comparable to models predicted by other groups, which describe the *in vivo* loss of function, destabilization and aggregation of the protein fold due to these mutations (Footz, Johnson et al. 2009; Chi, Yasumoto et al. 2010). If the protein is degraded by cellular machinery due to the effects of the mutations, it would also create a high local concentration of β-sheet-forming fragments, which could also interact with the amyloid β peptide. Thus, there are several possible mechanisms for the nucleating core of Aβ(1-42) to interact with β-strands from the β-propeller fold.

The disease-related mutations from Figure 2-15 were made within the sequence of the WDR36 homology model, the structure was minimized again and the secondary structures of the backbone angles were re-evaluated. For these mutations, there is a significant change in the backbone phi and psi angles, represented in the Ramachandran plots, corresponding to changes in the secondary structure of the mutants (**Figure 2-16**).

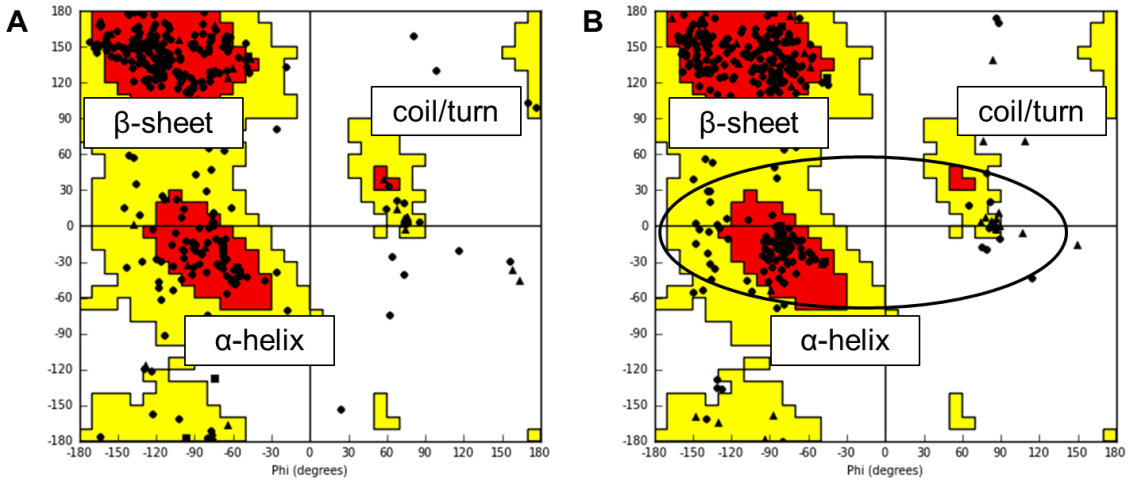

Figure 2-16. Ramachandran plots for WDR36 (single-blade model) before (a) and after making disease-related mutations (b) described in Figure 6 and minimizing the resulting structure. As the β-sheets are disrupted, they become more conformationally flexible.

These mutations in WDR36 were also studied *in vivo* in yeast, and it was found that, although some mutations lead to functional defects in the protein's ability to process RNA, this was not enough to elicit the characteristics of the glaucoma phenotype (Footz, Johnson et al. 2009). The fact that the mutations alone lead to growth impairment and not cell death point to the necessity of environmental factors or other interactions for development of the glaucoma disease state.

Discussion

Using homology modeling, I have constructed models of glaucoma disease-related proteins that have no current crystal structures in the PDB. The myocilin model shows a mixture of α-helix and β-sheet, consistent with previous reports(Jacobson, Andrews et al. 2001; Burns, Orwig et al. 2010). The optineurin model shows a primarily extended alpha-helical nature which would be consistent with the evidence that it is embedded in a membrane(Rezaie, Child et al. 2002; Park, Tibudan et al. 2007; Bond, Peden et al. 2011). The WDR36 homology model shows a pair of β-sheet rich propeller domains with short α-helices connecting the two subunits and another shows a single β-propeller structure. Since the amyloid aggregates associated with glaucoma have a different morphology and relative toxicity, perhaps the amyloid monomer interacts with a different set of proteins prior to assembly into full-length fibrils and the protein folds unique to the eye, such as the β-sheet rich WDR36, are capable of altering the pathways of amyloid assembly. This would be one explanation for differences in the aggregates between the brain and the eye. As the WDR36 protein is proposed to have a high percentage of β-sheet character, the β-propeller may be the most likely to interact with the amyloid β peptide.

When aligned, there are discrepancies in the segment alignments in the WDR36 model that are not observed in the GPBS alignments, suggesting that either WDR36 shares fewer homologous residues with the WD repeat family or improper threading through the host crystal structure. The individual aggregation propensities for the GPBS β-strands decrease from internal strands A to external strands D. This

pattern is common when ten other representative β-propeller structures are subjected to the same analysis, which may be a property evolved to provide β-sheet edge-protection, as well as to increase the solubility of the overall structure. Although this trend is not observed in the WDR36 homology model, the aggregation propensity for the A strand is similar to GPBS and B and C are similar to the ten representative β-propeller structures.

When disease-related mutations were highlighted within the model structure, I was able to determine several interactions that could be negatively impacted, leading to destabilization of the fold. To examine this further these mutations were energy minimized, with the recalculated secondary structure composition showing a greater number of coils and helices (**Figure 2-16**), consistent with the mutations destabilizing the β-sheet arrangements leading to a more conformationally flexible state. Interestingly, though the model and the positions of the mutations are consistent with those in the literature, none of these mutations or combination of mutations is enough to cause large-scale unfolding events that could lead to the disease state, suggesting that there are other contributors to the development of the glaucoma phenotype. This could also be due to the use of the Amber force field used in the minimization. More extensive molecular dynamics simulations would need to be done to be sure that this structure is not trapped in a local minimum. The observation that the more internal sequences have a much higher propensity for aggregating may mean that removal or displacement of the external D strands at any position may lead to the exposure of more aggregation-prone strands that could readily template other aggregation-prone sequences.

One model that could lead to a β-propeller structure being very prone to aggregate without complete unfolding of the propeller folds is the displacement of the external D strand. In the following chapter, I will describe this model in more detail, as well as determine the ability of the D strand to mitigate aggregation of the more aggregation-prone internal strands. Because the folds are highly homologous across the family and the aggregation propensities at each position appear to be conserved, I use the GPBS crystal structure for the following experiments as it is a well-characterized and representative member of the WD40 β-propeller family.

Materials and Methods

Glaucoma-Related Protein Sequence Alignments and Homology Modeling

Sequences of OPTN, MYOC, and WDR36 were all subjected to similar analyses: homologous sequences were found using the Basic Local Alignment Search Tool (BLAST, http://blast.ncbi.nlm.nih.gov/). The sequences were aligned using either the online ClustalW2 Multiple Alignment Tool (http://www.ebi.ac.uk/Tools/msa/clustalw2/) or the multiple sequence alignment tool available in the Maestro BioLuminate program available from Schrödinger (http://www.schrodinger.com/). Once aligned, the sequences were submitted to the HHPred (Homology detection & structure prediction by HMM-HMM comparison, http://toolkit.tuebingen.mpg.de/hhpred) server for analysis using the most current HMM database (Söding, Biegert et al. 2005). Following the second alignment in HHPred, the secondary structure of each alignment set was scored using PSIPRED (Protein secondary structure prediction based on position-specific scoring matrices) to increase alignment sensitivity (Jones 1999). The highest-scoring structural homologues (not necessarily sequence homologues) were selected and the PDBs were downloaded. Sequences of each protein were threaded through their structural homologues using either Modeller (http://toolkit.tuebingen.mpg.de/modeller) (Šali, Potterton et al. 1995) or by using the Protein Homology Model Builder within the Maestro 9.3 toolbox from Schrödinger (http://www.schrodinger.com/). This process resulted in three final PDB files, one for each threaded sequence, that were rendered using POV-Ray (Persistence of Vision Raytracer, http://www.povray.org/).

Mutations were made in the WDR36 model using Maestro and this new structure was minimized in implicit water using AMBER force-field and PRCG method for 5k iterations using a conjugate gradient with tolerance of 0.05. The Ramachandran was recalculated following minimization within the Maestro program.

Alignment of β-Propeller Blades and Aggregation Propensities

Individual β-strand sequences were located using the crystal structure of the G Protein β Subunit (PDB: 1A0R) and were collated by their position into individual text files. The sequences were submitted to the Aggrescan server (http://bioinf.uab.es/aggrescan/) as individual peptide fragments from five to eight amino acids in length (Conchillo-Sole, de Groot et al. 2007). The Aggrescan analysis gives an aggregation profile, amino-acid aggregation-propensity value average (a^4v), Total Hot-Spot Area (THSA) and a THSA per residue (THSAr), which is the THSA divided by the number of residues in the input amino-acid sequence. Only the THSAr value was used for calculating the average score for each set of sequences, one set each for strands A, B, C and D. The total average score for each position was normalized to the THSAr value for the Aβ(16-22) sequence, KLVFFAE, which was 0.680. All normalized scores were plotted as columns using OriginPro 8.6 graphing software (http://www.originlab.com/). This procedure was repeated for the WDR36 model and also for ten other β-propellers. Strands were located using the PDB files and were collated into separate files for each position prior to submission to the Aggrescan server.

Chapter 3

β-Propeller Fragment Assembly and Modulation of Self-Assembly in Peptide Chimeras

Introduction

The β-propeller structure has been the focus of many protein evolution studies because of its modular nature and the important role that these structures play in signal transduction pathways. The β-propeller fold typically requires chaperones to fold correctly when expressed due to its complexity and the blade subunits have conserved residues that sit in the overlap region between the blades to ensure the most stable packing arrangement (Witarto and Sode 2001; Springer 2002). Though a few β propellers have been shown to be relatively stable upon unfolding, it is generally observed that destabilization of the propeller fold can lead to extensive aggregation (Juhász, Szeltner et al. 2005; Nikkhah, Jawad-Alami et al. 2006; Chaudhuri, Söding et al. 2008; Wang, Huang et al. 2008). Recently, Tawfik and coworkers showed that several blade subunits of tachylectin-2, a symmetrical five-bladed β-propeller, could be truncated from the full propeller structure and then reassemble on their own, but only after using directed evolution techniques to evolve more soluble subunits (Yadid and Tawfik 2007; Yadid and Tawfik 2011). They observed the aggregation of the wild type subunits, but, as it was not the focus of their experiment, did not characterize these aggregates.

It has been proposed that the β propeller fold has evolved a negative design feature at its external β-sheet edges to decrease the propensity for edge-to-edge

hydrogen-bonding that can lead to extended β-sheet formation (Richardson and Richardson 2002). Because many external D strand (see **Figure 2-9** for strand positions) sequences contain prolines or charged residues, the surface that is most exposed in the propeller structure is more random coil in nature and may even contain short α-helices that would be unable to hydrogen bond with an extended β strand (Richardson and Richardson 2002; FarzadFard, Gharaei et al. 2008). The concept of β-sheet edge-capping is of great interest in the fields of protein evolution and designing therapeutics to prevent or decrease amyloid β assembly in models of Alzheimer's disease as well as other amyloid diseases.

The Nowick group at UC-Irvine has been successful in designing macrocyclic molecules that can inhibit the assembly of amyloid β. These molecules have two faces—one that is a recognition sequence, such as Aβ(16-22), and another that has a β-sheet blocker, designed to both stabilize the upper strand and prevent infinite β sheet hydrogen-bonding along the lower strand (**Figure 3-1**) (Khakshoor, Demeler et al. 2007). Commonly, the blocker strand named "Hao" is a tripeptide β-strand mimic that decreases the hydrogen-bonding capability of the lower strand. The identity of the side chains in both the recognition and blocking strands direct assembly into dimers and tertramers with hydrophobic interactions driving their assembly (Khakshoor, Demeler et al. 2007; Liu, Sawaya et al. 2011; Zheng, Liu et al. 2011).

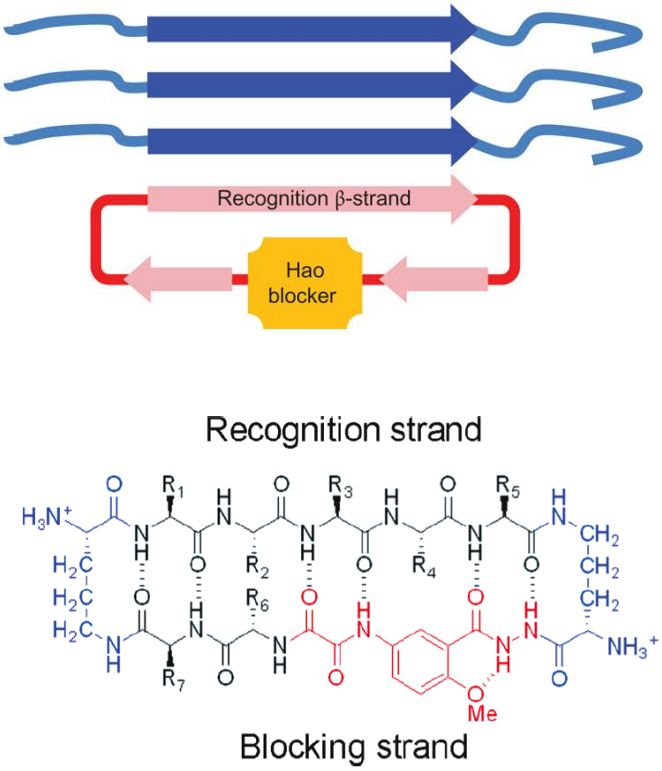

Figure 3-1. Macrocycle peptide consisting of an upper β-strand and lower β strand connected by two δ-linked ornithine turns. The pentapeptide R1-R5 is amyloidogenic while positions R6 and R7 are substituted with side chains that increase stability and solubility(Liu, Sawaya et al. 2011).

By varying the recognition sequence, they were able to show that the macrocyclic β sheet peptides were able to significantly inhibit amyloid assembly in several systems by capping the growing oligomers and protofilaments (**Figure 3-2**) (Zheng, Liu et al. 2011).

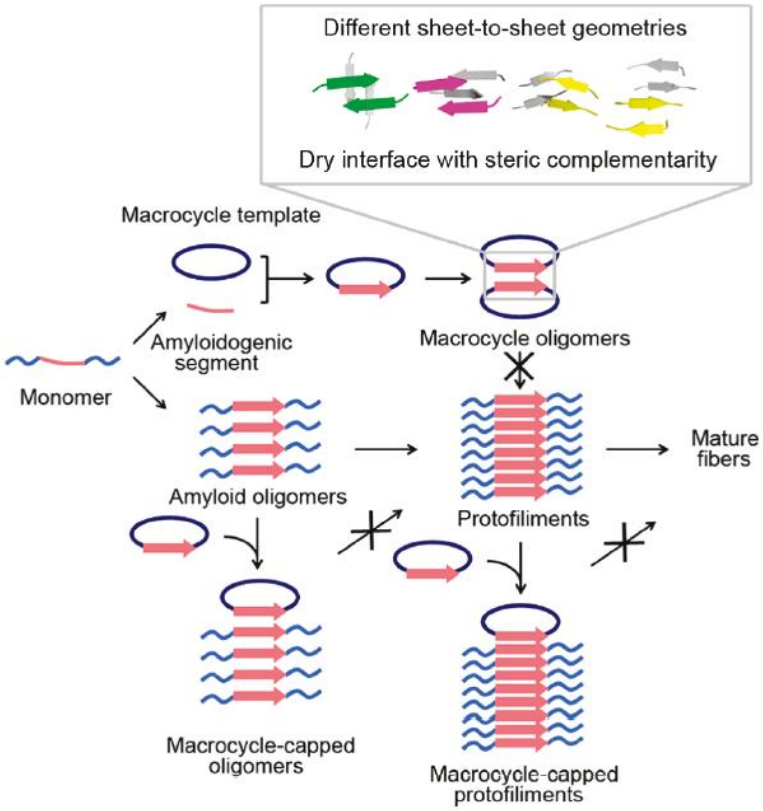

Figure 3-2. Schematic showing the capping mechanism proposed to halt the elongation of extended amyloid hydrogen bonding (Liu, Sawaya et al. 2011). If the macrocycle associates with itself (top), it can form a dimer which prevents it from interacting with the amyloid. At lower concentrations, the macrocycle can interact with the amyloid oligomers or protofilaments (bottom) to inhibit the growth of the β-sheet by blocking the hydrogen-bonding capabilities of the exposed β-strand.

Using the same principles, the external strands of the β-propeller fold in the D position of each blade may have a similar role in capping the β sheet by inhibiting extended β-sheet formation to keep the fold stable and soluble. The perturbation of

these D strands would allow for exposure of internal strands that can more readily hydrogen bond with nearby peptide monomers, such as amyloid β. I proposed that the internal strands, which have a high propensity to aggregate, were being protected and "edge-capped" by the D strands. If this was true, then the aggregation of the blade subunits should be modulated by the removal of the D strand. To determine if the blade subunits could aggregate on their own or if they could interact with the amyloid β peptide, it was necessary to break down the β-propeller fold into its blade subunits and study these as both whole units (around 40 residues) as well as to separate these further into smaller β hairpins (about 20 residues) (**Figure 3-3**).

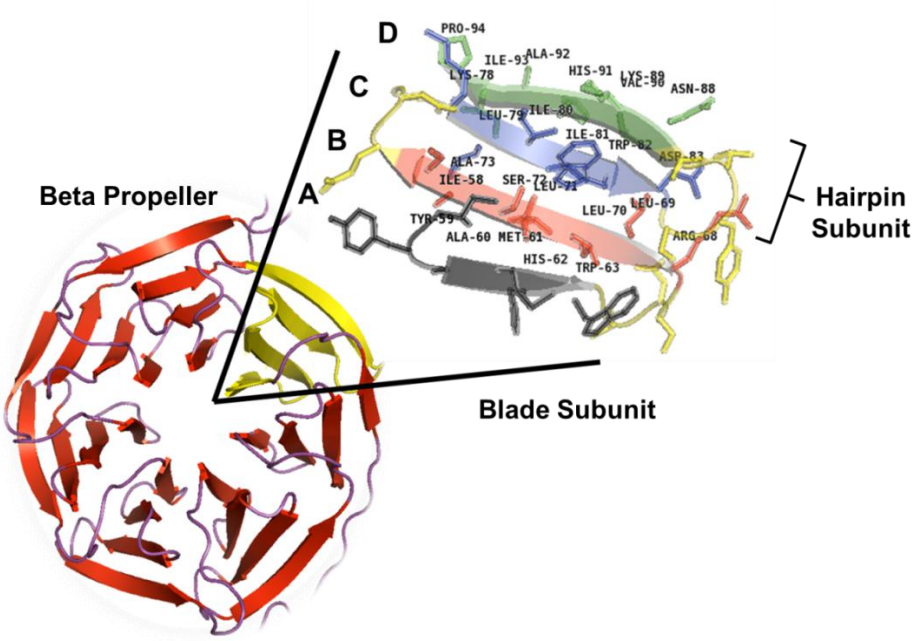

Figure 3-3. Structure of a β-propeller fold showing an individual blade subunit and an external hairpin subunit within the blade (PDB: 1A0R).

Here, I show that the blade subunits of the GPBS propeller have the ability to self-assemble into amyloid and the hairpin segments of these subunits can modulate the assembly of Aβ(16-22).

Results

Blade Fragments of G Protein Self-Assemble into Amyloid

As a crystal structure for WDR36 does not yet exist, the assembly characteristics of another well-studied member of the WD40 repeat family (as discussed in Chapter 2), the β subunit of the heterotrimeric G-coupled protein receptor, was chosen because the hypothesis that the D strand caps the core of the blade should be true for all β-propeller structures. Utilizing the sequence and crystal structure (PDB: 1A0R), I selected a blade sequence that contained a similar charge-hydrophobic-charge pattern as Aβ(16-22) (KLVFFAE), which is essential for Aβ(1-42) assembly into fibers (blue indicates positively charged side chains, grey hydrophobic and red negatively charged). Initially, the full blade was tested to determine if it would remain as a monomer in solution, form higher-mass oligomers or assemble into fibers without the protection of the surrounding blades in the fully-folded propeller structure. Several full-length blade peptides (38-42 residues) of the G protein β subunit were synthesized and characterized (**Table 3-1**).

Table 3-1. Blades extracted from the G Protein β subunit (GPBS, PDB: 1A0R) showing the β-strands in blue, α-helices in orange and random coil linker regions in gray. Blade 7 is capped by a portion at the N-terminal portion of the protein that is not directly connected in sequence to the last β strand.

Blade Position	Blade Sequence
1 (residues 58-94)	IYAMHW-GTDS-RLLLSA-SQDG-KLIIWD-SYTT-NKVHAIP
2 (residues 100-136)	VMTCAYA-PSG-NYVACGG-LDNI-CSIYNL-KTRE-GNVRS
3 (residues 146-181)	LSCCRF-LDDN-QIVTSS-GDT-TCALWD-IETG-QQTTTFT
4 (residues 187-222)	VMSLSLA-PDT-RLFVSG-ACDA-SAKLWD-VREG-MCRQTF
5 (residues 230-264)	NAICFF-PNG-NAFATGS-DDAT-CRLFDL-RAD-QELMTY
6 (residues 273-308)	ITSVSFS-KSG-RLLLAG-YDDF-NCNVWD-ALKA-DRAGVL
7 (residues 315-340 and 46-51)	VSCLGVT-DDGM-AVATGS-WDSF-LKIWN……RTRRTL

The peptide sequences corresponding to blades one, two, three and four of the GPBS were dissolved in a mixture of 60% water and 40% acetonitrile at neutral pH to keep them soluble. The concentration at which the peptides have a high enough local concentration to begin to self-associate, or critical assembly concentration, varies from peptide to peptide. For Aβ(16-22), this concentration is between 500μM and 1mM depending on batch-to-batch variations in water content of synthesized peptide. Because of these variations, a lower (1mM) and a higher concentration (4mM) were used when solvating the GPBS peptides. Aliquots were pulled over several time points for analysis by circular dichroism spectroscopy (CD), transmission electron microscopy (TEM) and infrared spectroscopy (FT-IR). After a week of incubation, the blade peptides form fibril structures at neutral pH as observed by TEM (**Figure 3-4**). TEM can be used to visualize the different morphologies present in a sample but does not report on the local environment or molecular-level arrangement of the peptides in the aggregates.

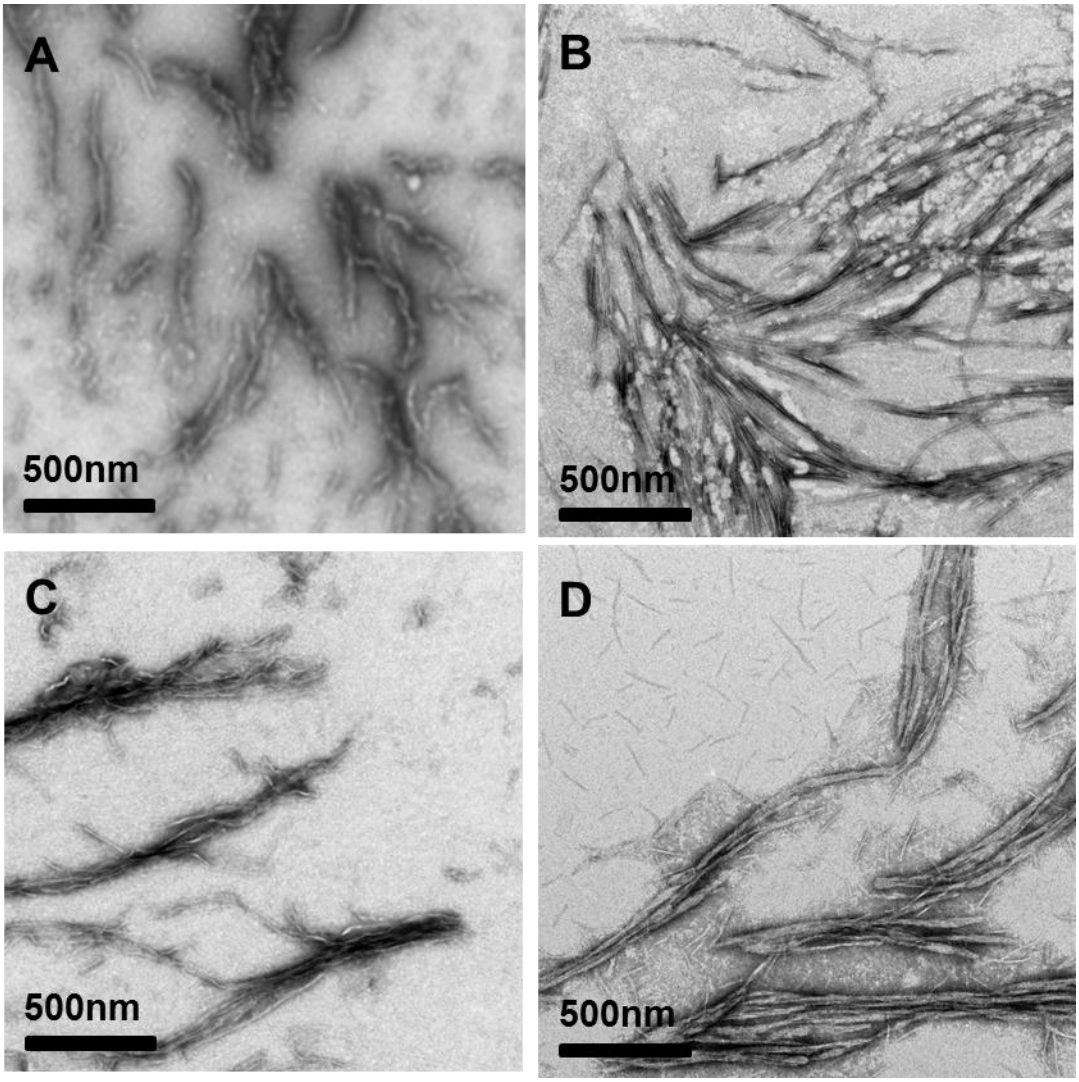

Figure 3-4. TEM micrographs of individual blades (a) one, (b) two, (c) three and (d) four of the GPBS protein (1mM, neutral pH) after incubation at room temperature for two weeks.

The TEM micrographs indicate that the peptide sequences corresponding to blades one to four of GPBS all assemble into fibers. The fibrils formed from the propeller blades of the GPBS have CD and FTIR signatures that are consistent with the peptides being arranged into β-sheets. The lack of an IR band at 1690cm^{-1}

suggests that these peptides form parallel β-sheets, though it is not clear if these have similar registry (**Figure 3-5**).

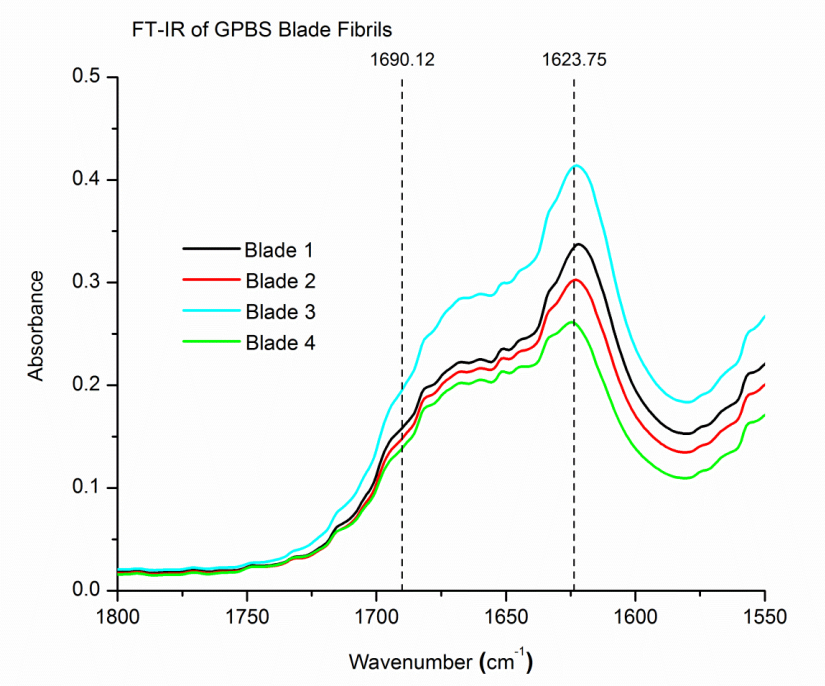

Figure 3-5. FTIR of the Amide I region of the GPBS blades assembled as fibers at 1mM at neutral pH show characteristic absorbance increase at the β-sheet stretching frequency near 1621 cm^{-1}.

Another characteristic of amyloid is the ability to bind the histological dye, Congo Red (CR). When added to these GPBS fibrils, Congo Red UV/Vis signal at 498nm increases in intensity and a red shift is observed in its UV spectrum presumably due to the organization of the molecule along the amyloid surface (Childers 2009) (**Figure 3-6**).

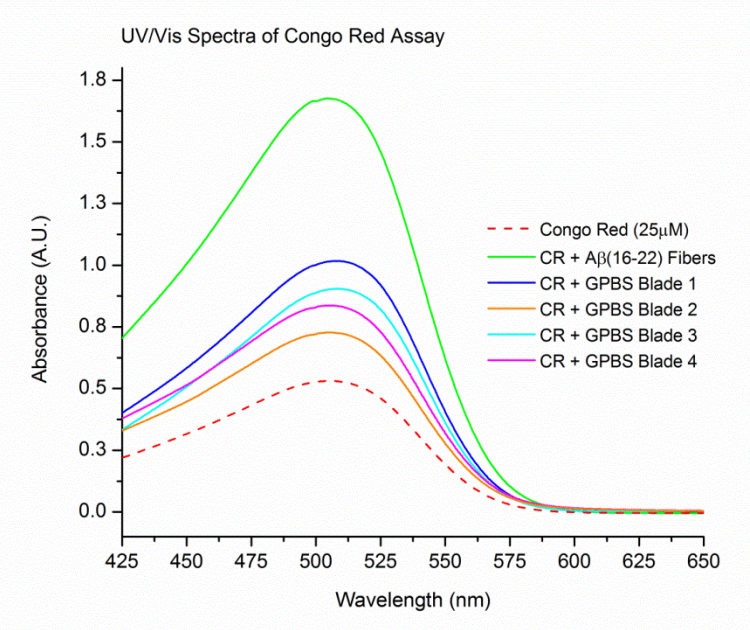

Figure 3-6. UV/Vis spectra of Congo Red alone (dashed red) and Congo Red with 200μL Aβ(16-22) fibers (1mM) (green) and 200μL GPBS blade fibrils at 1mM (blue, orange, cyan and magenta) showing the characteristic change in absorbance due to the Congo Red molecules binding to the surface of the amyloid fibrils(Childers 2009).

CD can be used to determine average populations of α-helix, β sheet, or random coil structures. β-sheet has a negative CD signature at 215nm, α-helix has a negative signature at 210nm and 220nm and the random coil signature is near 200nm. GPBS fibers exhibit the characteristic β-sheet signature when measured by CD (**Figure 3-7**), Taken together, the TEM, FT-IR, CR binding and CD results demonstrate that the fibers have high population of β-sheet secondary structure and form amyloid.

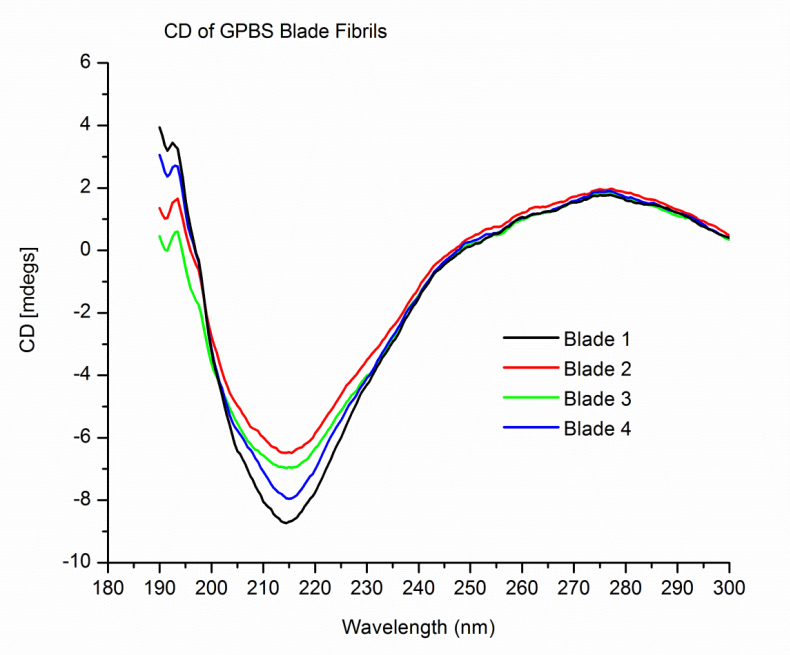

Figure 3-7. Circular dichroism (CD) spectra of the GPBS blades after 1 week of incubation (1mM at neutral pH).

Because it is likely that the blades do not fold into their antiparallel, Greek key motifs outside of the native protein fold, I have developed several models for how the full-length blade of the G protein could be assembling into fibrils. One possibility is that the hydrophobic similarities between Strand A and C become the driving force for their association and subsequent assembly, which pushes the more highly-charged strand D out into solution to create uniquely charged surface that may provide a positive charge for the negatively charged sulfonate groups of Congo Red (**Figure 3-8**). Another model is that the peptides hydrogen bond in a linear extended fashion after completely unfolding with the self-association between the individual strands.

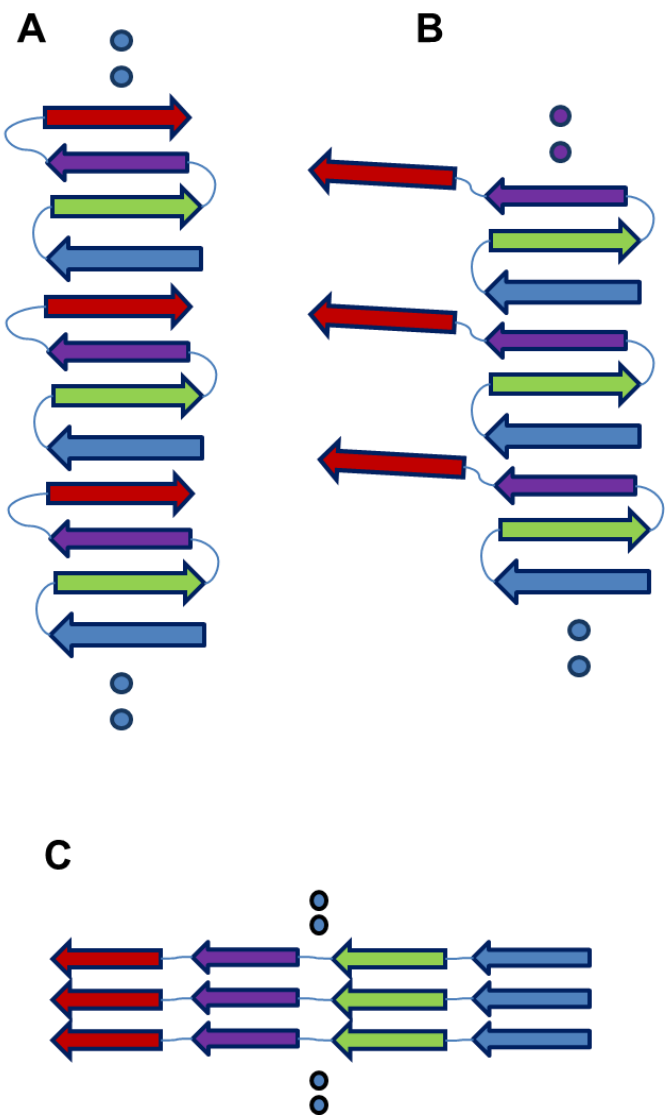

Figure 3-8. Models of GPBS fibril assembly (a) by blade stacking, (b) with D strand extended into solution and (b) with all strands forming an extended β-sheet. In this cartoon, the A strand is blue, B strand is green, C strand is purple and D strand is red.

Though more work is needed to confirm the orientation of the peptides in these GPBS blade fibrils, these models suggest that the hydrophobic internal strands of the

blades have a high propensity for aggregation that cannot be mitigated by the single hydrophilic D strand (red in **Figure 3-8**).

I proposed that the D strand may be able to inhibit the assembly in a β hairpin containing only the C and D strands. Shorter hairpin fragments of the blade subunits consisting of the C-D portion of the strand were synthesized, removing the more aggregation-prone internal strands. If the D strand were capable of blocking one face of hydrogen bonding by forming a hairpin, I proposed that these hairpin fragments should form only dimers or tetramers in solution, similar to those observed by the Nowick group(Khakshoor, Demeler et al. 2007; Liu, Sawaya et al. 2011; Zheng, Liu et al. 2011). If properly folded, these hairpins would have a recognition face with more hydrophobic residues (C strand) and a face blocking further hydrogen bonding (D strand), similar to Nowick's inhibitory β-sheet macrocycles (**Figure 3-9**).

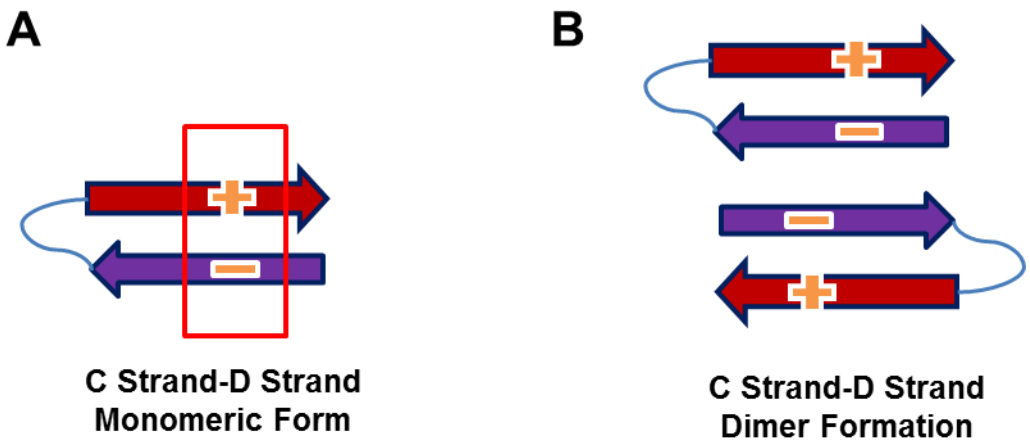

Figure 3-9. Models of only the C and D strands of the GPBS blade. (a) The C strand is connected to the D strand via a linker and the pair have complementary electrostatic side chains to stabilize the hairpin folding. (b) At higher concentration,

the more hydrophobic side chains of the C strand would cluster with the C strand of another hairpin, leading to the formation of dimers.

Secondary structure predictions from the submission of sequences to the SSPred server show that the C-D hairpin consists of a β strand followed by a sequence with high random-coil nature, consistent with the D strand being less well-defined than the C strand (**Figure 3-10**), though this gives us no indication of hairpin formation. After incubation for 2 weeks, heterogeneous fibrils were observed by TEM showing that this sequence still retains its propensity to form amyloid despite my prediction that extended β-sheet formation would be effectively inhibited by the D strand, consistent with this peptide not folding into a hairpin.

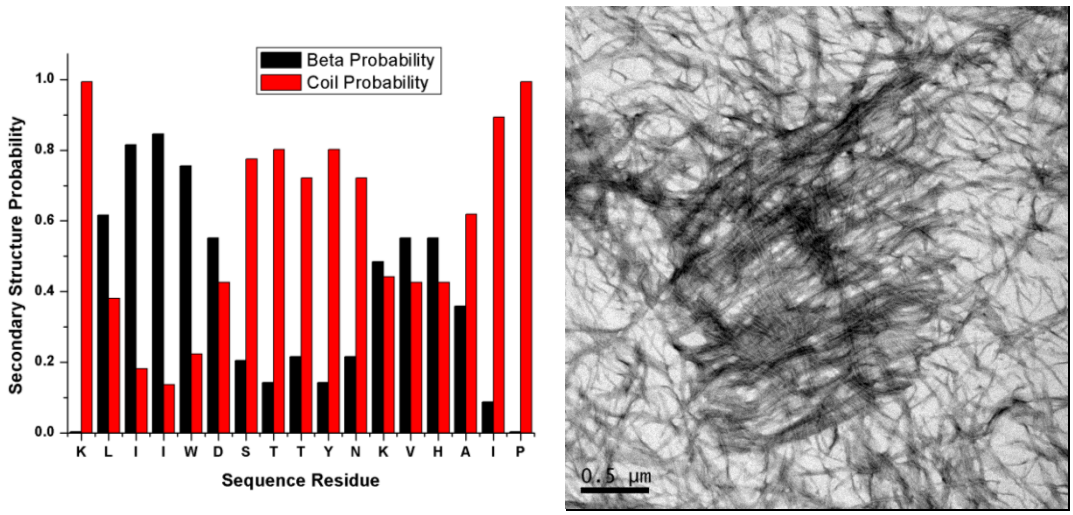

Figure 3-10. SSPred secondary structure prediction (left) and TEM (right) of C-SYTT-D fragment of GPBS after 2 weeks incubation (1mM at neutral pH).

Aβ(16-22) Assembly is Attenuated in β-Hairpins

I made several models taken from the native β-propeller fold of the GPBS of how the β hairpins could assemble or be capped by the D strand. When I covalently connected Aβ(16-22) to another Aβ(16-22) sequence via a linker, the peptide could fold into a hairpin to hydrogen bond along its peptide backbone, similar to Aβ(16-22) alone. It could also be extended, with both of the sequences being involved in intermolecular hydrogen bonding (**Figure 3-11**).

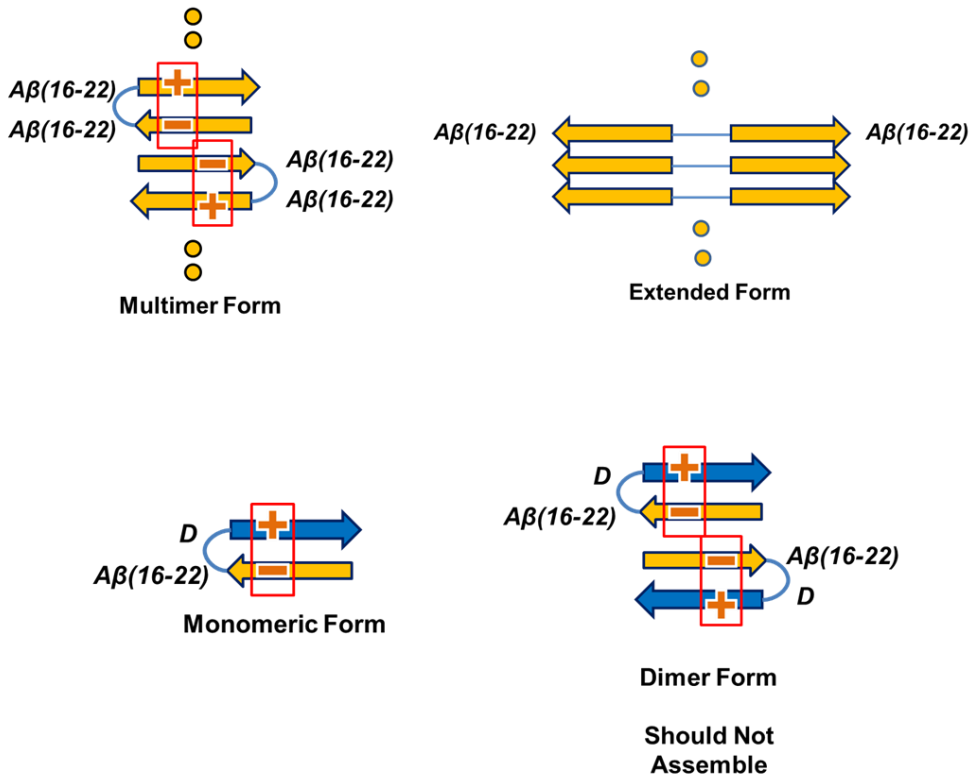

Figure 3-11. Potential arrangements of the amyloid/amyloid chimera and the amyloid/D strand chimera. Stabilizing electrostatic interactions are highlighted in red.

When the Aβ(16-22) sequence is placed in the C-D hairpin to replace the lower C strand, I predicted that the Aβ(16-22) could still hydrogen bond to form a dimer, but would not be able to form extended β sheet structures due to the interference of the D strand sequence (**Figure 3-11**). This arrangement is dependent on the closure of the hairpin via an electrostatic salt-bridge formed by side chains from the C and D strands. The D strand sequence contains a Lys that would give a complementary charge to the Glu in Aβ(16-22), forming a salt-bridge that would stabilize the β-hairpin formation (**Figure 3-12**), though the SSPred results do not indicate that these would necessarily form stable hairpins.

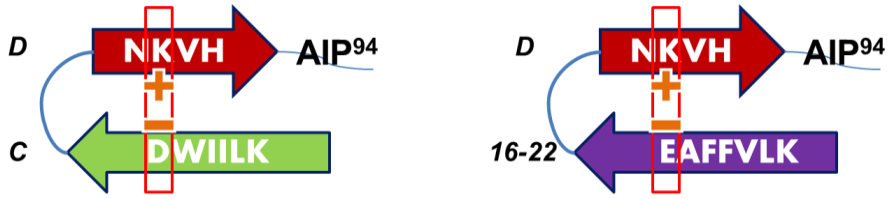

Figure 3-12. Electrostatic interactions leading to stabilized β-hairpins in the GPBS C and D segment (left) and the Aβ(16-22) chimera with the D strand (right). This would remove the need for complete cyclization as shown in the macrocyclic inhibitors mentioned previously.

To determine the effects of the D strand on Aβ(16-22) assembly, the C and D strands in this hairpin were replaced with the Aβ(16-22) sequence, KLVFFAE. The secondary structure prediction of the KLVFFAE-linker-KLVFFAE chimera was

consistent with a β strand connected to another β strand by a random coil linker (**Figure 3-13**). After incubation for 2 weeks at neutral pH, I observed a heterogeneous mixture of fibrils and particles at by TEM. The heterogeneity of the sample may be due to the linker used, which will be discussed later in this chapter.

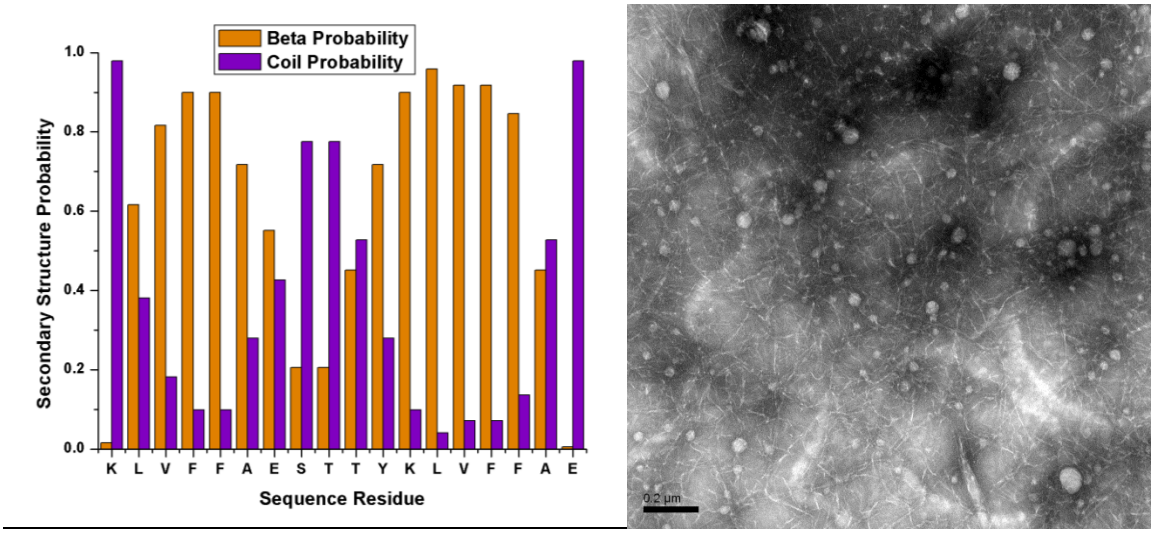

Figure 3-13. SSPred secondary structure prediction (left) and TEM (right) of KLVFFAE-SYTT-KLVFFAE chimera after 2 weeks incubation (1mM at neutral pH).

I also replaced the lower C strand in the C-D hairpin with the Aβ(16-22) sequence, KLVFFAE. The secondary structure prediction for KLVFFAE-linker-D strand sequence was almost identical to the wild type C-D hairpin sequence with a β strand followed by a random coil region (**Figure 3-14**). TEM shows that this sequence also assembles into fibrils, though the rate of assembly was much slower than KLVFFAE

alone under these conditions, suggesting that the D strand may hinder the β sheet organization.

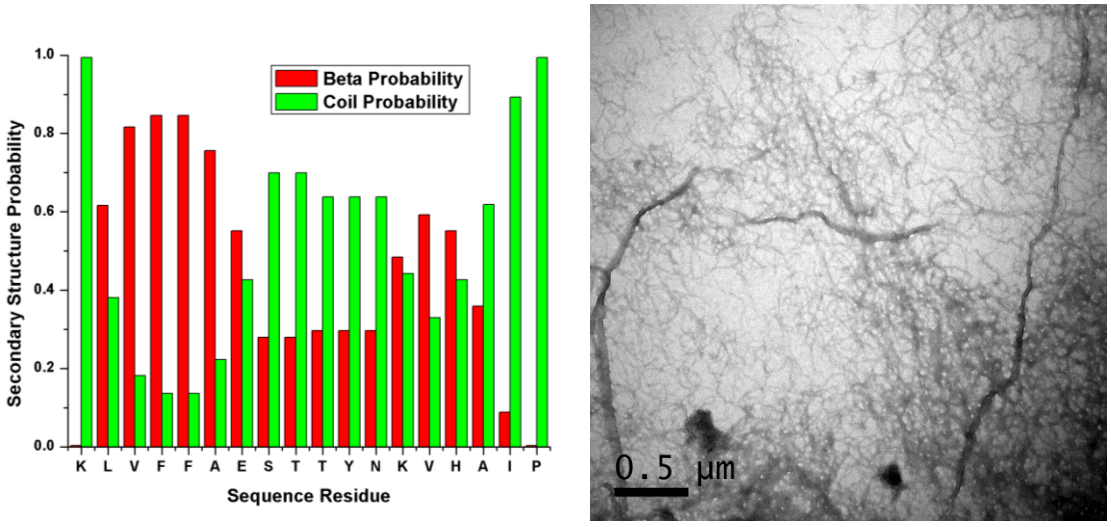

Figure 3-14. SSPred secondary structure prediction (left) and TEM (right) of KLVFFAE-SYTT-D chimera after 2 weeks incubation (1mM at neutral pH).

The KLVFFAE-linker-D strand sample also exhibited several intermediates throughout the assembly that could be observed by TEM. Whereas the KLVFFAE sequence alone self-assembles very quickly into fibrils at neutral pH (fibrils can be seen as soon as 20 minutes after solvation), this sequence formed large spherical particles after several hours that persisted for at least 2 days (**Figure 3-15**).

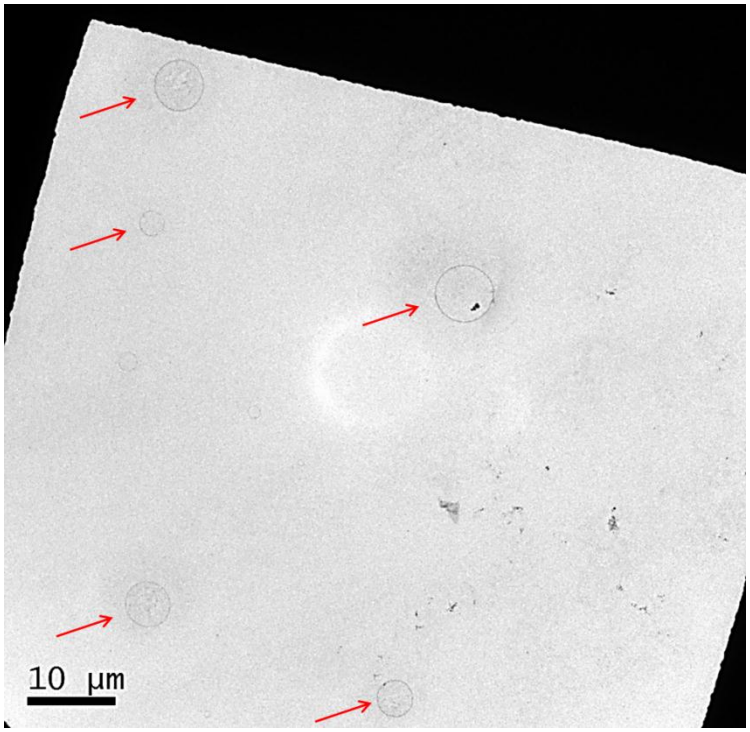

Figure 3-15. TEM of KLVFFAE-SYTT-NKVHAIP chimera after incubation for two days (1mM at neutral pH) shows that the peptide has assembled into large spherical particles (red arrows).

After 6 days, there were very small, fine fibrils visible by TEM, but also some remaining particles. The fibrils were shorter and curlier than wild type Aβ(16-22) fibrils had many branching points where fibrils twisted around other fibrils (**Figure 3-16**).

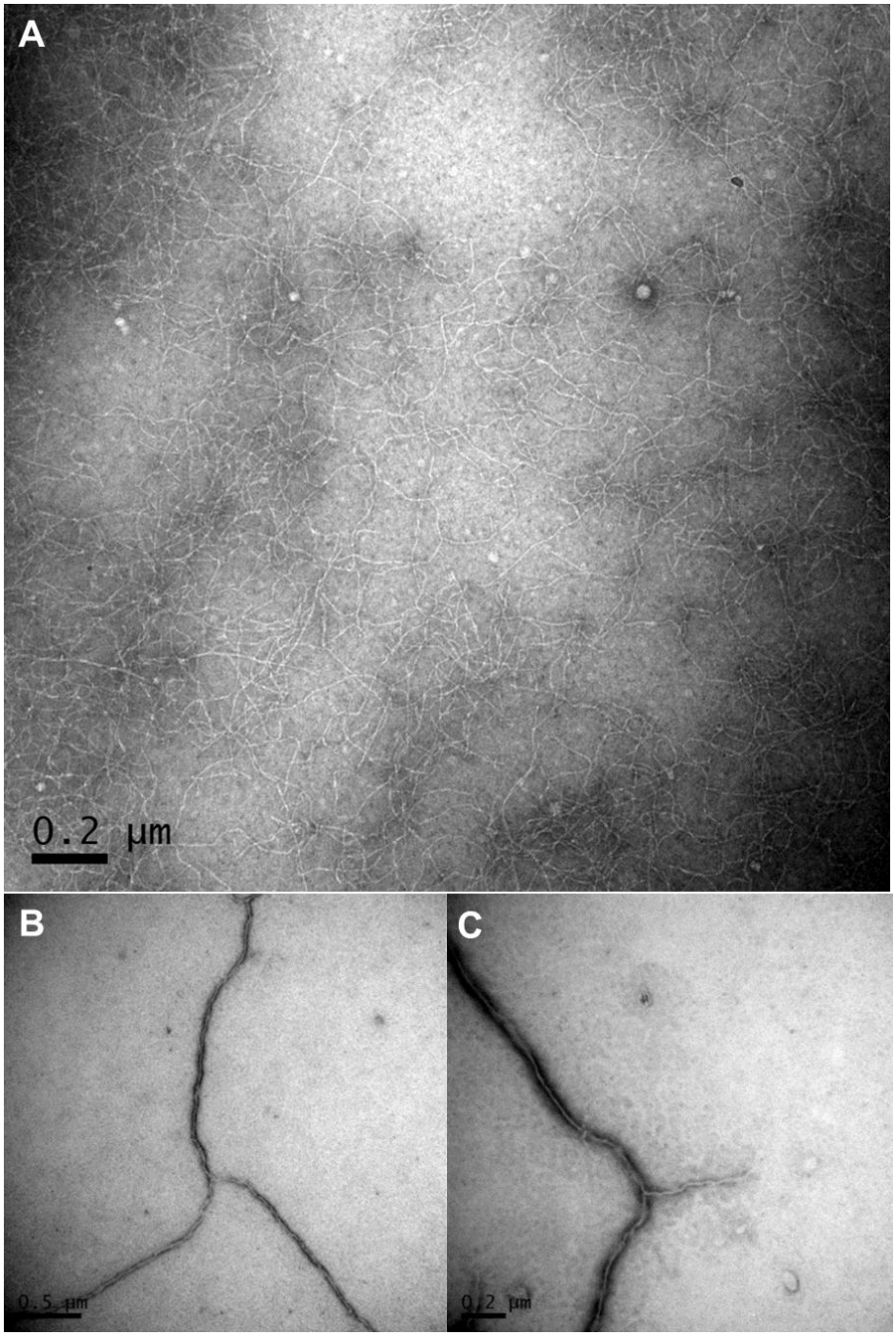

Figure 3-16. TEMs of KLVFFAE-SYTT-NKVHAIP intermediates after 6 days of incubation (1mM at neutral pH) showing twisted fibrils and particles (a) and fibril branching (b and c).

When the assembly of these chimeras was followed by monitoring the β-sheet CD signature at 215nm, it was apparent that, although the chimeras still assembled into fibrils, the presence of the D strand significantly slowed the assembly rate of Aβ(16-22) versus the chimera containing only the Aβ(16-22) sequence (**Figure 3-17**).

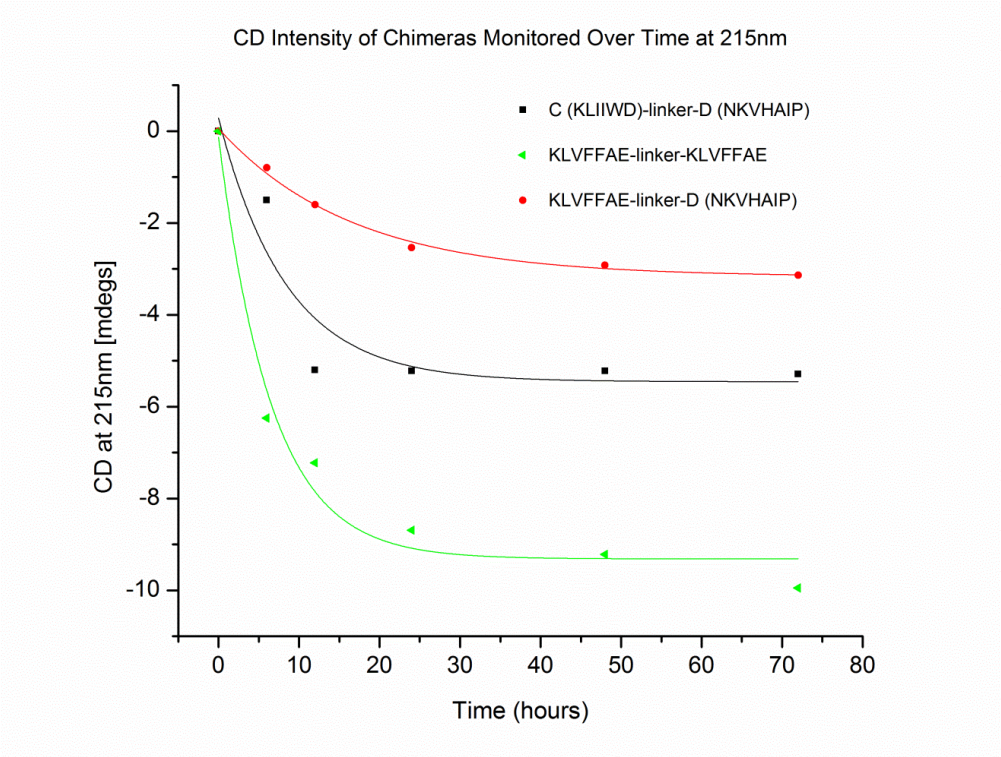

Figure 3-17. CD intensity of the chimera assemblies monitored over time at 215nm. Curves were fitted using a single exponential decay.

The slower assembly rate observed for the C-D and KLVFFAE-D chimeras does not necessarily correspond to the thermodynamic stability of the final aggregate, though it does support that the D strand addition is capable of altering the assembly pathway.

Linker Sequence Affects the Morphology of Aβ(16-22) Chimeras

Significant heterogeneity was observed in the KLVFFAE-linker-KLVFFAE peptide when using the wild type linker sequence taken from the hairpin of the GPBS (-SYTT-), so I sought to define the role of the linker in altering the morphology of KLVFFAE-linker-KLVFFAE peptide chimeras. Several variants of this peptide were synthesized with linkers based on typical β-turns (**Table 3-2**).

Table 3-2. Linkers used to make chimeras of Aβ(16-22) and the corresponding morphology observed by TEM after 2 weeks incubation. Sequences using the –GGG--, –GGS-- and –GPGG- linkers were inspired by previous work by Kun Lu (unpublished).

Fragment	Linker	Fragment	Morphology Observed
C (KLIIWD)	-SYTT- (from GPBS)	D (NKVHAIP)	Bundled fibrils
KLVFFAE	-SYTT- (from GPBS)	KLVFFAE	Mixture of heterogeneous fibrils and particles
KLVFFAE	-SYTT- (from GPBS)	D (NKVHAIP)	Short, curly fibrils
KLVFFAE	-GPG-	KLVFFAE	Short fibrils at both pH 2.0 and 7.0
KLVFFAE	-GGG-	KLVFFAE	Fibrils at pH 2.0, heterogeneous sheets at pH 7.0

KLVFFAE	-GGS-	KLVFFAE	Smooth fibrils at pH 2.0, rough fibrils at pH 7.0
KLVFFAE	-GPGG-	KLVFFAE	Similar smooth fibrils at pH 2.0 and pH 7.0

These KLVFFAE chimeras were allowed to assemble at 1mM at both pH 2.0 and pH 7.0 for 2 weeks. Though most still form fibrils, they are more heterogeneous than Aβ(16-22) fibrils previously observed (**Figure 3-19**).

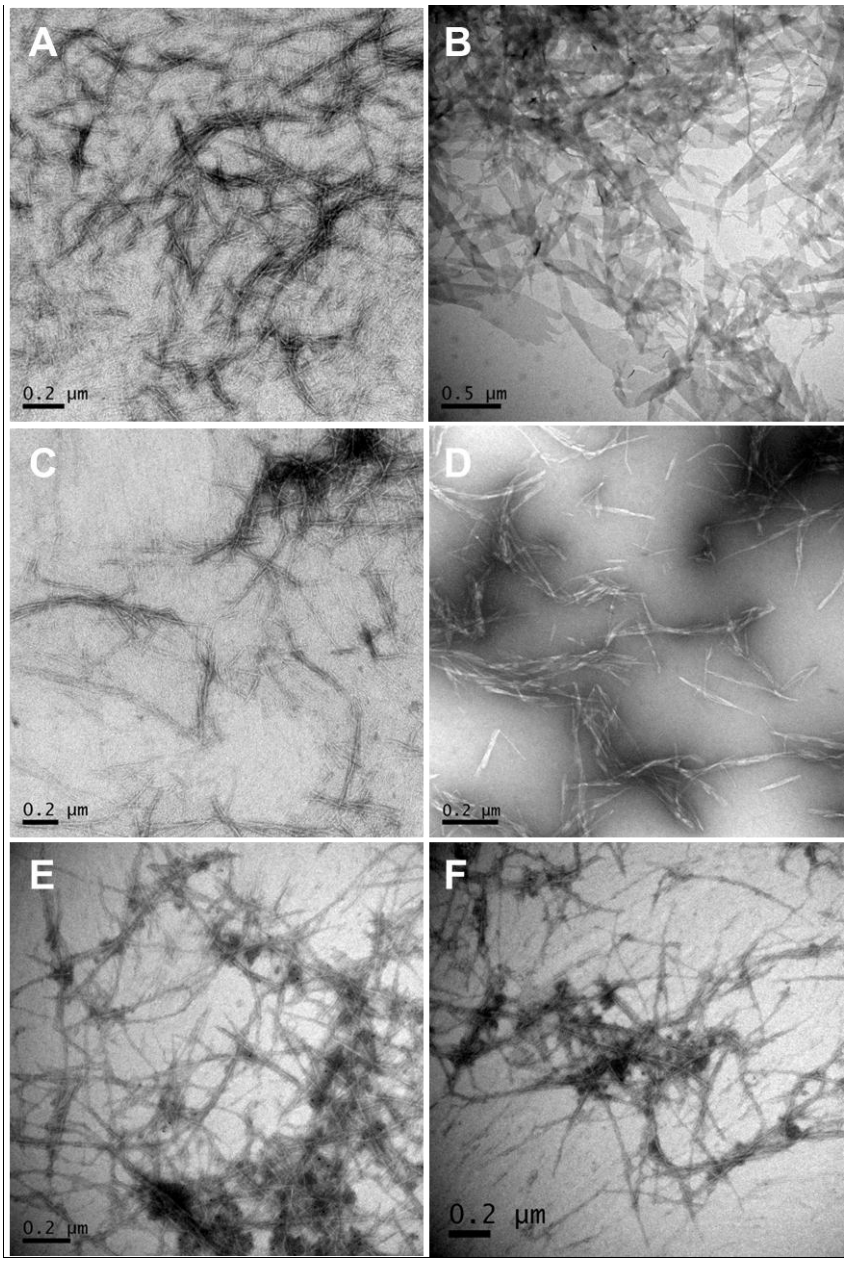

Figure 3-19. TEMs of chimeras with different linkers. (a) KLVFFAE-GGG-KLVFFAE forms fibrils at pH 2.0 (a) and sheets at pH 7.0 (b). KLVFFAE-GGS-KLVFFAE forms smooth fibrils at pH 2.0 (c) and rough fibrils at pH 7.0 (d). KLVFFAE-GPGG-KLVFFAE forms fibrils at pH 2.0 (e) and at pH 7.0 (f).

The linkers do not alter the ability of the Aβ(16-22) sequence to assemble, but they do seem to cause changes in the structure that lead to more heterogeneous morphologies. The linker sequence and length both appear to contribute to the differences observed between the chimeras, though more work will be needed to fully characterize the packing arrangement of the peptides in these fibril structures.

Discussion

I have shown that full-length blade subunits truncated from the GPBS β-propeller fold are able to self-assemble into amyloid fibrils. These fibrils are β-sheet rich, can be stained with Congo Red and appear to be in a parallel arrangement by initial analysis by FTIR, though the registry of the fibrils is yet to be determined. The self-assembly of the blades is not surprising since I show in the last chapter that their internal sequences have a high propensity to aggregate. When excised from the protective core of the fully-folded protein, these sequences would likely cluster together to exclude water, leading to the formation of larger aggregates. Though I hypothesized that the D strand may be acting to cap growth of the β-sheet, the removal of the other protective features of the protein is clearly more powerful than any interaction that the D strand could mitigate. With exposure of the aggregation-prone core of the blade, determining the D strand's ability to halt β-sheet growth becomes increasingly complicated. To simplify the possible interactions that could lead to aggregation, I removed the A and B strands from the sequences, creating a C-

D hairpin. Assuming the sequences fold into stable hairpins, the ability of the D strand to prevent β-sheet growth and assembly should be easier to measure in a hairpin that contains only one aggregation prone stand (strand C) with dimer formation being more favorable than extended β-sheet formation.

Interestingly, the C strand-D strand hairpin also assembles into fibrils, though the rate of assembly and the stability of the final morphology appear to be affected by the linking of the external D strand sequence. If the C-D hairpin also assembles, this suggests that either the salt-bridge that is proposed to stabilize the fold is not intact or that the shorter peptide can access a more extended morphology than I proposed. It is also possible that the peptide did fold into a hairpin but is still able to stack either with the units stacking head-to-tail or in a side-to-side fashion. It would be interesting to determine the preferred folding arrangement of this peptide because it would allow us to predict the mechanism of the fibril formation and how it is affected by the D strand sequence, which is proposed to protect the β sheet from aggregating in the native protein fold. This model could also be used to help define the nucleating core of the β-propeller during its folding process, as well as for designing new inhibitors to disrupt β-sheet aggregation using sequences from native protein folds.

When Aβ(16-22) is placed into the C-D hairpin at either position or both, its assembly is modulated. The replacement of the C and D sequences with KLVFFAE results in heterogeneous fibril formation. The KLVFFAE-D peptide did assemble, but at a slower rate than the wildtype Aβ(16-22) or the KLVFFAE-KLVFFAE chimera. The presence of the long-lived intermediate particle morphology before the

emergence of fibrils suggests that the D strand is slowing the formation of the paracrystalline nucleus that is necessary for the propagation of the fibrils. The fibrils that do eventually form are "curly" and have multiple branching points, which may be due to the D strand facing outward and acting as a template for the extension of a separate fibril. These properties may be specific for the D strand sequence or it may be a more general phenomenon accessible to other sequences, though this will need further characterization to discern.

It is also apparent from these experiments that the sequence of the linker region in these Aβ(16-22) chimeras plays a role in the final morphology and the degree of peptide lamination, which may be a function of flexibility, length, or a combination of both. The chimeras linked by the longer linker –GPGG- appear to more closely resemble the Aβ(16-22) fibrils, which may suggest that the added length and flexibility may be necessary for the formation of a packing arrangement similar to non-covalently linked Aβ(16-22). The observation that none of the sequences form nanotubes at pH 2.0, as is typical for free Aβ(16-22), demonstrates that the attachment of the peptide by the linker inhibits the ability of the peptides to pack into a bilayer or that this arrangement is not amenable to extended lamination (Mehta, Lu et al. 2008; Childers, Mehta et al. 2010; Ni, Childers et al. 2012). If a linker were discovered that allowed the chimera to form nanotubes, it would be a great opportunity for further functionalization of the bilayer interface.

It is apparent from these experiments that the A, B, C and D strands of the GPBS are not soluble or stable as monomers without being encased within the surrounding blade subunits. These proteins typically require the assistance of

chaperones to fold properly and the high propensity for the core sequences to aggregate may explain this necessity. Previously described experiments used in the development of more soluble blades using directed evolution techniques may overcome this by selecting for blade subunits with A, B and C strands that have sequences that are less aggregation-prone. This correlation is not described here, but merits further investigation and would likely yield more insight as to the sequence distributions within the blades that lead to stability as a monomer versus as a protein subunit. Because the blade and the smaller hairpin units assemble and the analysis of these structures to determine the mechanism of assembly appears complex, I chose to characterize the individual sequences at each position within the GPBS to discern the contribution of each strand to the aggregation of the larger subunit and also to determine which strand could serve as a template for the nucleation of Aβ(16-22).

Materials and Methods

All chemicals were purchased from Sigma-Aldrich (St. Louis, MO) unless stated otherwise.

Peptide Synthesis and Purification

All peptides used were synthesized using standard FMOC solid-phase peptide synthesis (SPPS) protocols with both N- and C-termini capped using microwave synthesis (CEM Liberty Peptide Synthesizer, North Carolina, USA). The peptides were cleaved from the solid support using a cleavage cocktail of TFA/anisole (95/5, v/v). The resulting solution was filtered from the resin and precipitated using excess chilled anhydrous ethyl ether. The centrifuged pellet was dried under house vacuum before purification. They were purified by reverse-phase HPLC (RP-HPLC) to greater than 99% and their mass was confirmed using TOF-MALDI mass spectrometry. Capped blade and hairpin sequences from the G-protein crystal structure (PDB: 1A0R) were synthesized using the same SPPS protocols and were purified and confirmed using previously described methods.

Peptide Assembly Conditions

For assembly, the peptides were dissolved in 40% acetonitrile/60% water to a final concentration of 1.0 mM unless otherwise stated. pH was adjusted to near pH 7.0 using pH paper and the solutions were allowed to mature at room temperature for the indicated time periods. To rapidly dissolve the peptide, the suspension was vortexed at high speed for 30s and sonicated at 40kHz in a room temperature water

bath for 1-2min. This process was repeated 3-4 times till the solution was clear, generally requiring less than 20 min to ensure complete dissolution.

Transmission Electron Microscopy

Samples were allowed to adsorb on a TEM grid (carbon/copper) for at least 1 min. Excess peptide solution was wicked away with filter paper. A 2-wt % uranyl acetate solution was added to TEM grids and incubated for 3-5 minutes before wicking away. Samples were then placed in a desiccator overnight. TEM micrographs were recorded with a Hitachi 7500 TEM at magnifications ranging from 2000x to 200,000x with a Tungsten filament at an accelerating voltage of 75 kV.

Fourier-Transform Infrared Spectroscopy

Sample aliquots (300μL) were centrifuged for 30 minutes at 13,000 rpm and frozen in a bath of dry ice and acetonitrile bath (-40°C) for 20 minutes before lyophilizing overnight. The IR spectra were acquired using a Jasco FT-IR 4100 ATR with a diamond crystal at room temperature and averaging 256 scans with $4cm^{-1}$ resolution. Background spectra were acquired immediately before each sample and were subtracted from each sample spectrum.

UV/Vis Spectroscopy of Congo Red Binding

A stock solution of Congo Red dye was prepared at 1mM at neutral pH. This was added to solutions of 1mM peptide assemblies for a final CR concentration of 25μM. Samples were incubated for 30 minutes and then the UV/Vis spectra were recorded

Circular Dichroism Spectroscopy

Samples (30 μL) were placed into a quartz cuvette with a 0.1 mm path length (Starna Cells). Each spectrum was obtained by scanning wavelength from 300 nm to 185 nm at a scanning rate of 100 nm/min with a resolution of 0.2 nm using a Jasco J-810 spectropolarimeter. For each CD run temperature was controlled at 20°C, unless otherwise stated. Prior to recording the presented final wavelength scan CD at 215 nm was recorded for approximately 15-minute period to ensure sample had stabilized at the CD measurement conditions. Three successive wavelength scans were averaged for each sample. Buffer control spectra were averaged and subtracted from the sample spectra.

Predictions of Peptide Secondary Structure

Sequences for the C-D hairpins were submitted to the SSPred (Protein Continuum Secondary Structure Predictor using high-resolution NMR data) server to get secondary structure predictions(Bodén and Bailey 2006). These predicted values were graphically represented on the server and were also transferred to OriginPro for analysis. Bar graphs were produced using these values showing the β-sheet and coil regions for each sequence.

Chapter 4

β-Propeller Fragments Self-Assemble into Distinct Morphologies

Introduction

As discussed in Chapter 3, both the full-length blades 1-4 of GPBS and the shorter hairpins of strands C-D self-assemble into amyloid. Therefore, I wanted to test if the β-propeller blade had a core nucleating sequence similar to the Aβ(16-22) sequence in the amyloid β peptide. Given the context, as described in Chapter 2, that the β-propeller of WDR36 could provide a templating surface to seed Aβ, the nucleating sequence of Aβ and the propeller domain would have the highest probability of interacting. It has been suggested that any peptide sequence has the ability to misfold into amyloid given the correct conditions (Halverson, Sucholeiki et al. 1991; Alberti, Halfmann et al. 2009; Chiti and Dobson 2009). In the GPBS, there are a total of 28 β strands with differing degrees of homology at each position, which was previously discussed in Chapter 2, but it was not clear which sequence would serve as the best template for Aβ(16-22). In other studies, it is commonly thought that self-templating, as measured by induction of aggregation, is the most common mechanism of amyloid aggregation in the disease state(Meyer-Luehmann, Coomaraswamy et al. 2006). However, it is not known how other β-strands interact with the amyloid β peptide, and β-strands with high propensities for aggregation may serve as the best templates for amyloid growth. With the abundance of β strands within the β-propeller structure, I hypothesized that these would have a high propensity to self-assemble as individual fragments due to their predisposition to

access an extended conformation, with mutations possibly leading to the exposure of internal β-strands (**Figure 4-1**).

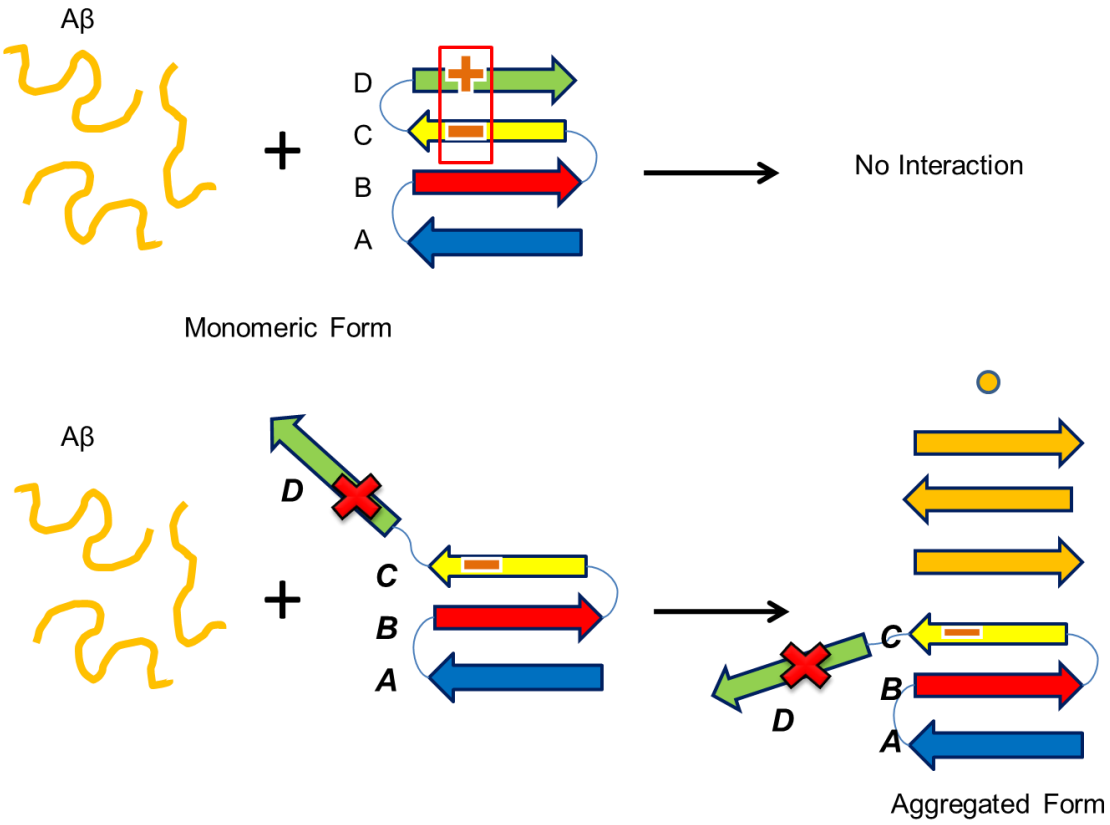

Figure 4-1. First generation model for the mutations within the GPBS blade leading to the exposure of a preorganized β-sheet template for nucleation of Aβ(16-22) monomer.

Since many short peptide sequences have been shown to self-assemble, it was necessary to score these fragments' ability to self-assemble, with the prediction that the more hydrophobic internal sequences would have lower critical assembly concentrations and form more stable crystalline aggregates. Given that the most

stable morphology observed for the full-length blade was fibrils, deviation from the fibril morphology would suggest that the individual short peptides are constrained by intermolecular interactions within the full blade during assembly. I predicted that by characterizing sequences from each position within the GPBS β-propeller blade, it should be possible to determine sequences that would serve as the best templates for Aβ(16-22) nucleation. I show here that the β-strands extracted from the full GPBS blade can self-assemble into morphologies that are distinct from that of the full blade.

Results

β-propeller Fragments from the GPBS Self-Assemble

Individual β-strand sequences were selected using the GPBS crystal structure and synthesized (**Figure 2-10**). Because these were segments of a larger protein tertiary structure, they were synthesized with an acylated N-terminus (CH_3CO-) and amidated C-terminus (-NH_2) to remove the effects that extra charge might play in the assembly process. The segments were assembled individually in 40% CH_3CN/60% H_2O at neutral pH and followed by both CD and TEM for comparison. The morphologies observed by TEM are summarized in **Table 4-1**. While several sequences were insoluble at the 1mM concentration used here, many assembled into sheets, particles or fibrils during the given incubation time.

Table 4-1. Individual β strands from the G Protein β Subunit crystal structure (PDB:1A0R) were synthesized, purified and allowed to self-assemble at 1mM for 1 week at pH 7.0. All peptides were synthesized with an N-terminal CH_3CO- and a C-terminal -NH_2. Morphologies observed by TEM were characterized as fibers (thin), sheets (wide, non-helical) or particles (spheres). N.A. = no assembly. IS = insoluble under these conditions. X = not synthesized.

Position A	**Morphology Observed**	**Position B**	**Morphology Observed**
IYAMHW	fibril	RLLLSA	particle
MTCAYA	insoluble	NYVACG	NA
SCCRFL	X	NQIVTS	NA
MSLSLA	insoluble	RLFVSG	particle
NAICFF	NA	NAFATG	NA
TSVSFS	fibril	RLLLAG	particle
CLGVTD	particle	RAVATGS	particle
Position C	**Morphology Observed**	**Position D**	**Morphology Observed**
KLIIWD	sheets	NKVHAIP	NA
DNICSI	X	RVSRELA	particle
TCALWD	sheets	TTTFT	NA
SAKLWD	NA	GMCRQTF	NA
TCRLFD	NA	QELMTYS	NA
NCNVWD	sheets	RAGVLA	particle
FLKIWN	NA	RTLR	NA

Although there is diversity in morphology, there are some correlations that can be made between the position of the sequence and the morphology observed. The sequences in the A position typically assembled into fibrils, some of which would bundle together to form larger macroscale assemblies (**Figure 4-2**). Several of these were very insoluble, possibly due to their sequences containing no charged residues.

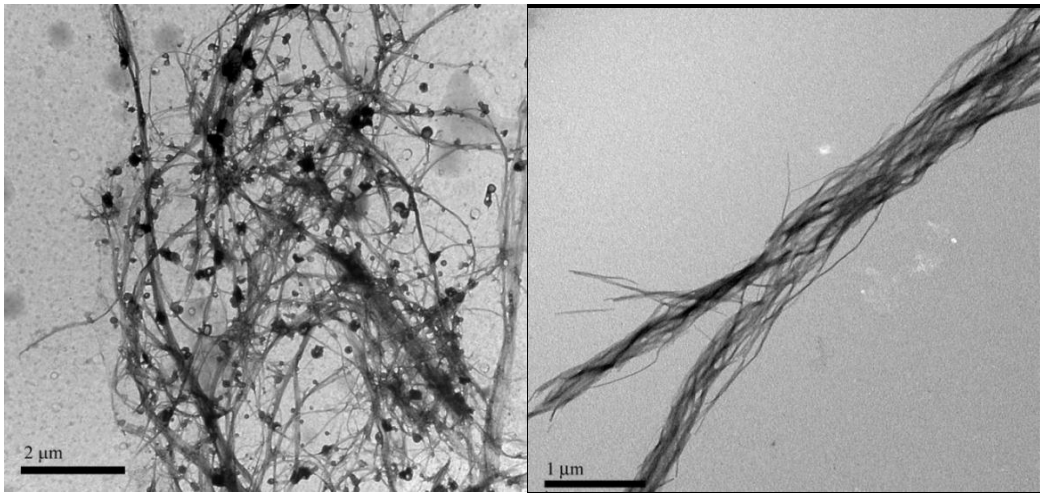

Figure 4-2. TEM of 1mM IYAMHW, strand A of GPBS blade 1, after 1 week incubation at neutral pH.

Sequences corresponding to the C position either do not assemble or, in the case of KLIIWD, assembled into large, flat sheets of different widths that have an unusual CD spectrum (**Figure 4-2**). The presence of the minimum at 235nm may be due to the alignment of the Trp residues that make up the KLIIWD sheets, as seen in other systems with multiple aromatic residues (Albinsson and Norden 1992). The extended lamination seen here is similar to that observed in previous experiments with KLVFFAED, Aβ(16-23), which also forms sheets (Thinh Bui, Honors Thesis).

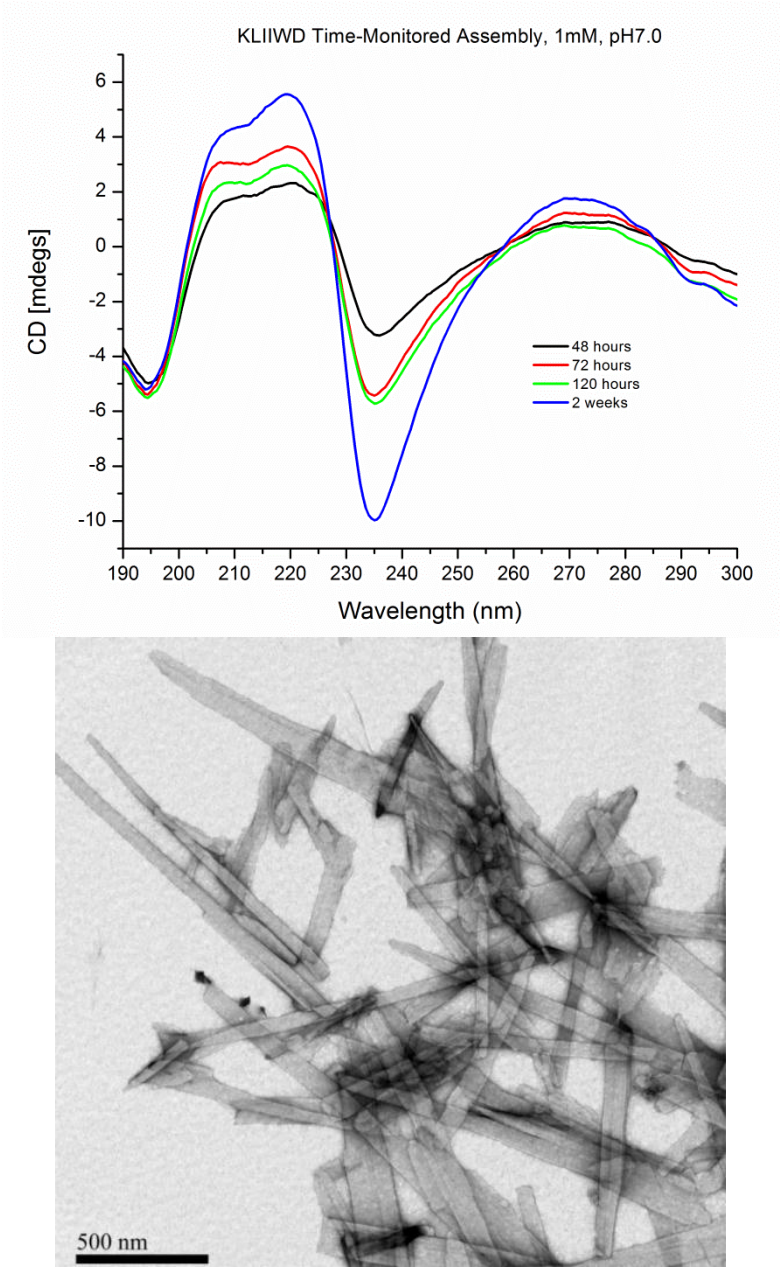

Figure 4-3. CD and TEM of 1mM KLIIWD, strand C of GPBS blade 1, after 1 week incubation at neutral pH.

The sequences in the C position that did not assemble from blades 4, 5 and 7 all have a positively charged residue in the middle of the sequence. The driving force for the assembly of the KLIIWD, position C sequence of blade one, should be similar to Aβ(16-22), both having a hydrophobic core sequence and complementary charges on either end. These assemblies, though they do not exhibit a typical fiber morphology, can still be stained with Congo Red (**Figure 4-4**), confirming that they are amyloid, just like Aβ(16-23).

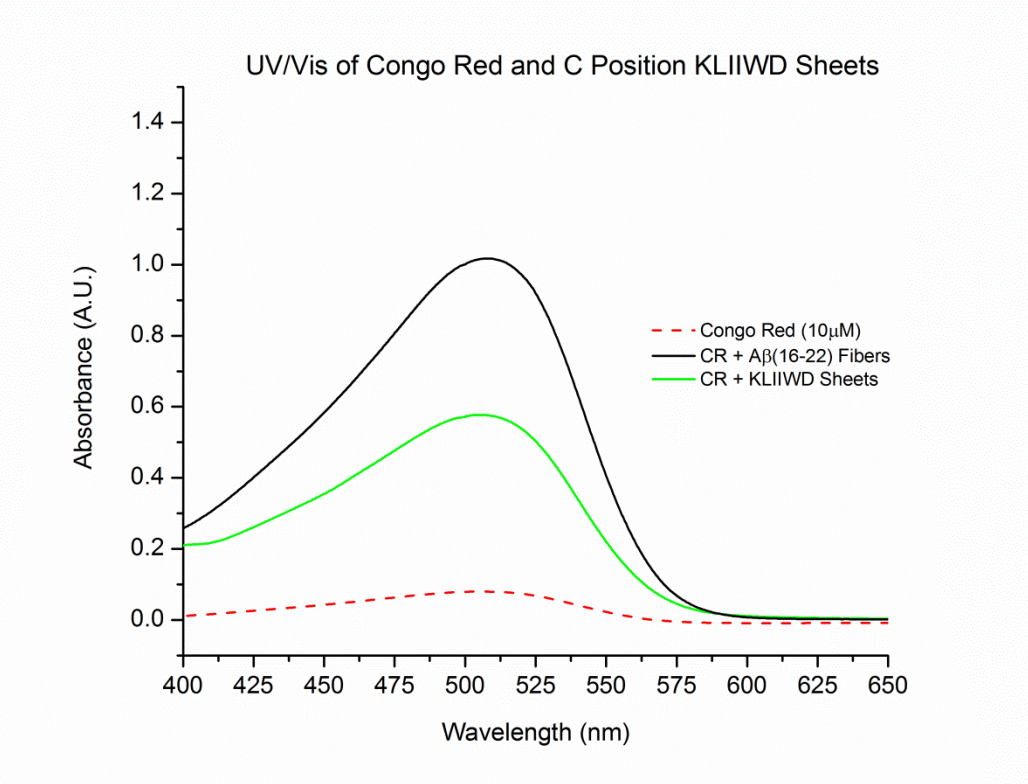

Figure 4-4. Congo Red binding 1mM Aβ(16-22) fibers (black) and 1mM KLIIWD sheets (green) at neutral pH.

The sheets formed by Aβ(16-23) are the result of lamination of hundreds of β-sheets, similar to the extended lamination seen for Aβ(16-22) at acidic pH, as discussed in Chapter 1. Typically, the lamination width of these β-sheet assemblies is determined by the side chains alternating along the peptide backbone and their particular interactions. Some interactions that may stabilize the lamination of sheets, and subsequently result in wider assemblies, include cation-π interactions and salt bridges. For example, at pH 7.0 we propose that the KLIIWD peptide is in an antiparallel in-register conformation (**Figure 4-4**) due to the salt-bridge formed by the aspartic acid side chain and the terminal lysine.

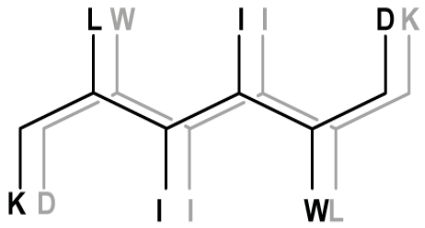

Figure 4-5. Proposed conformation of KLIIWD at pH 7.0.

If my model is correct, then the C sequence, KLIIWD, should form anti-parallel β-sheets within the sheet morphology based on the charged residues being on opposite faces. A method of investigating the structure of amyloid assemblies is to use infrared spectroscopy to probe the Amide I region, which corresponds predominantly to the carbonyl stretching vibrations of the peptide backbone and can be used to determine the secondary structure of the peptide. A peak around 1629 cm^{-1}

is indicative of β-strand formation and a secondary peak around 1690 cm^{-1} is common for strands oriented in an anti-parallel motif (**Figure 4-6**).

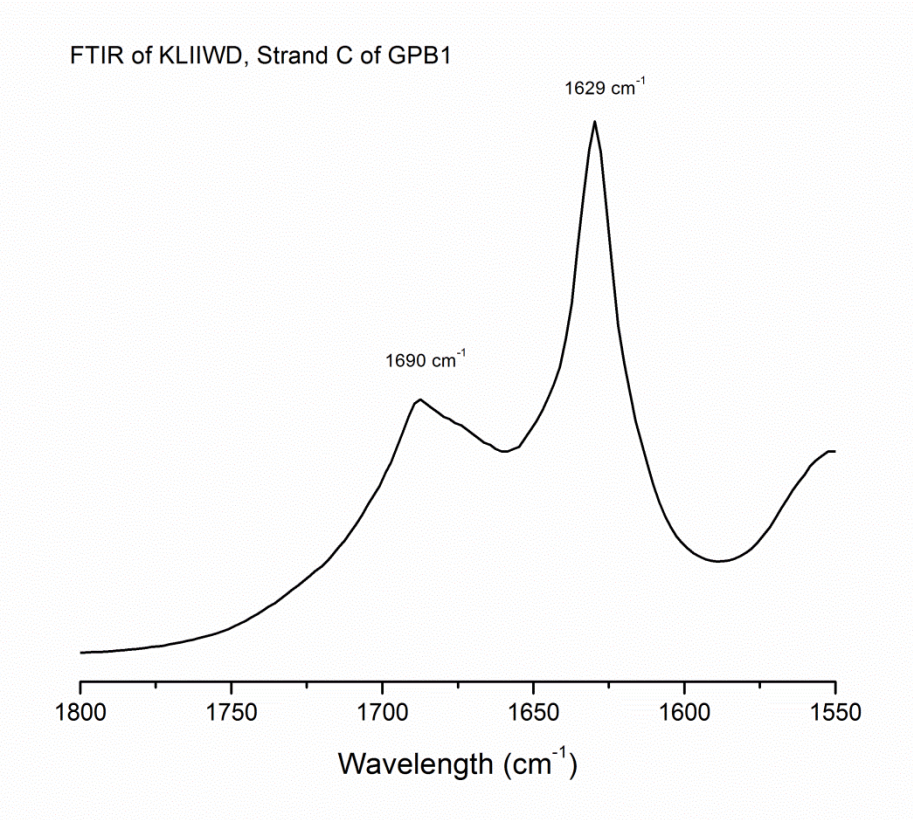

Figure 4-6. FTIR of the sheets formed by 1mM KLIIWD C strand at neutral pH after 1 week incubation.

The sequences in the D position did not have a high propensity to assemble under these conditions. Only two showed any aggregation as visualized by EM. This is likely due to their increased solubility from having multiple charged residues and decreased percentages of hydrophobic side chains. The organic solvent present in

these solutions may also hinder their assembly, though their assembly propensity in pure water was not examined.

The most interesting morphology observed in these experiments was the large, spherical particle that was formed primarily by the sequences in position B. These particles were able to exclude stain to be visualized by TEM and were also able to be seen by confocal microscopy. The characterization of the fiber and sheet morphologies was relatively straightforward because of their robust nature, but the particles responded more quickly to heating and cooling, demonstrating that they were more dynamic. I proposed that the particles would have similar properties as lipid vesicles and sought to characterize their properties.

Characterization of the Spherical Peptide Particles

The B position sequence RLLLSA self-assembles into large peptide particles that range in size from 200nm at higher temperatures (approximately 45°C) to 1-5μm at cooler temperatures (approximately 4°C). These particles have a CD spectrum consistent with the peptides being in a disorganized, fluctuating random-coil conformation though they remain in a non-crystalline particle form for more than 6 months (**Figure 4-7**).

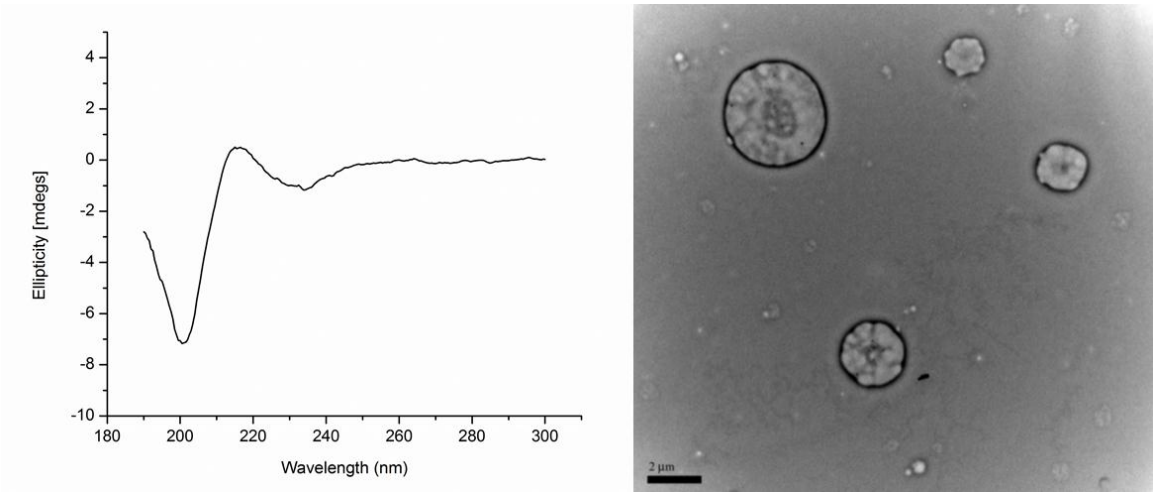

Figure 4-7. CD and TEM of 1mM RLLLSA, strand C of GPBS (Blade 1), after 1 week incubation at neutral pH and room temperature.

Negative stains such as uranyl acetate are used in TEM to highlight the features of peptide assemblies. Interestingly, if the RLLLSA peptide in incubated in uranyl acetate, a stain which is excluded from dense peptide regions, the particles show a heterogeneous core that demonstrates that it is not uniform in its internal peptide distribution (**Figure 4-8**).

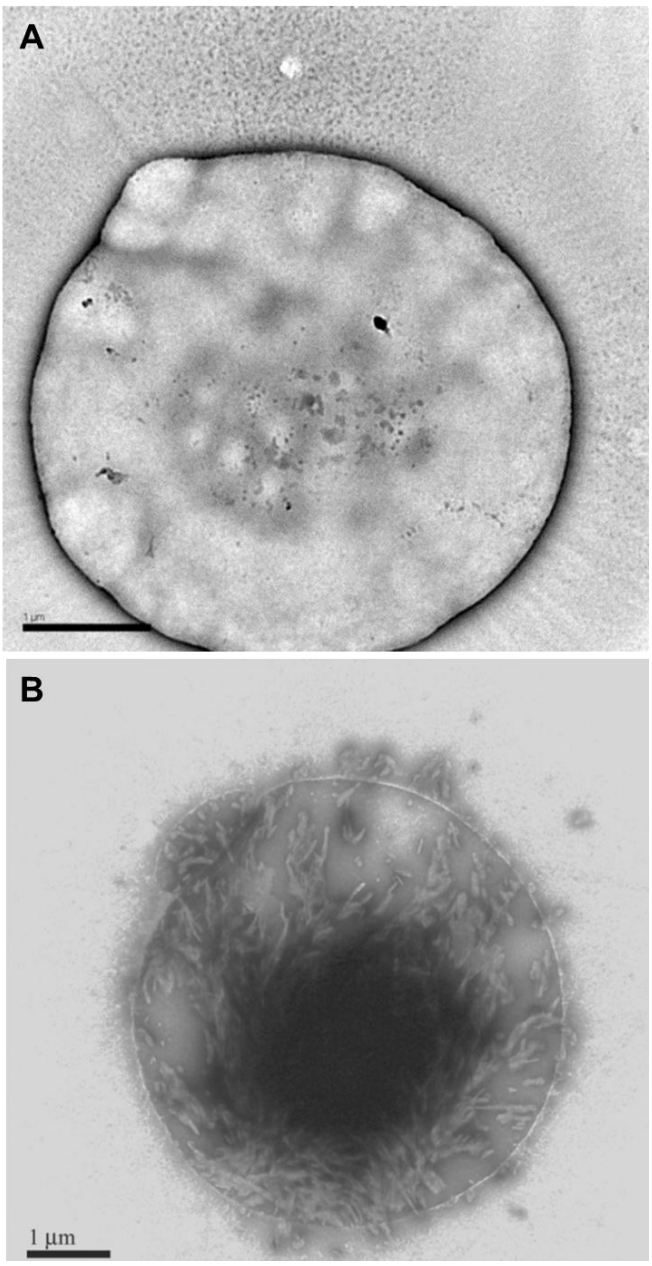

Figure 4-8. TEM of 1mM RLLLSA particle at neutral pH (a) and 1mM RLLLSA incubated with 2 wt% uranyl acetate (b) showing the heterogeneity of the particle interior.

After observing that the particles had enough stability to both exclude or include stain, it was apparent that they may also be compressible using atomic force microscopy (AFM), which is frequently used to characterize lipid vesicles (Mao 2005). Lipid vesicles can be extruded to form particles of different sizes, as well as having unique surface properties that allow them to be elastic or compressible (**Figure 4-9**).

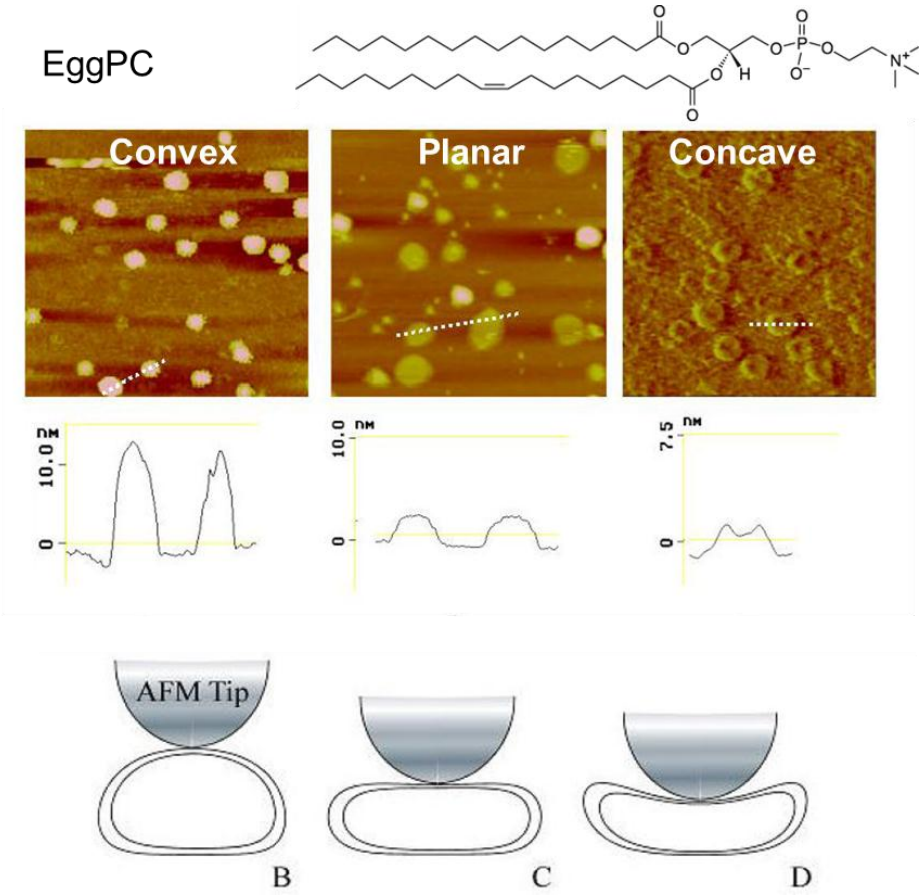

Figure 4-9. AFM of vesicles formed by Egg phosphotidyl choline that exhibit different surface compressibilities. The more rigid vesicles will have a convex or planar profile (B and C) while those that are more fluid will have a concave profile (D) (Mao 2005).

Using tapping-mode AFM, it was possible to collect a height profile for the RLLLSA particles and, on average, these were 33nm at the edges. Because it was compressible the profile is bowl-shaped, consistent with the concave lipid vesicles shown previously in **Figure 4-9d**.

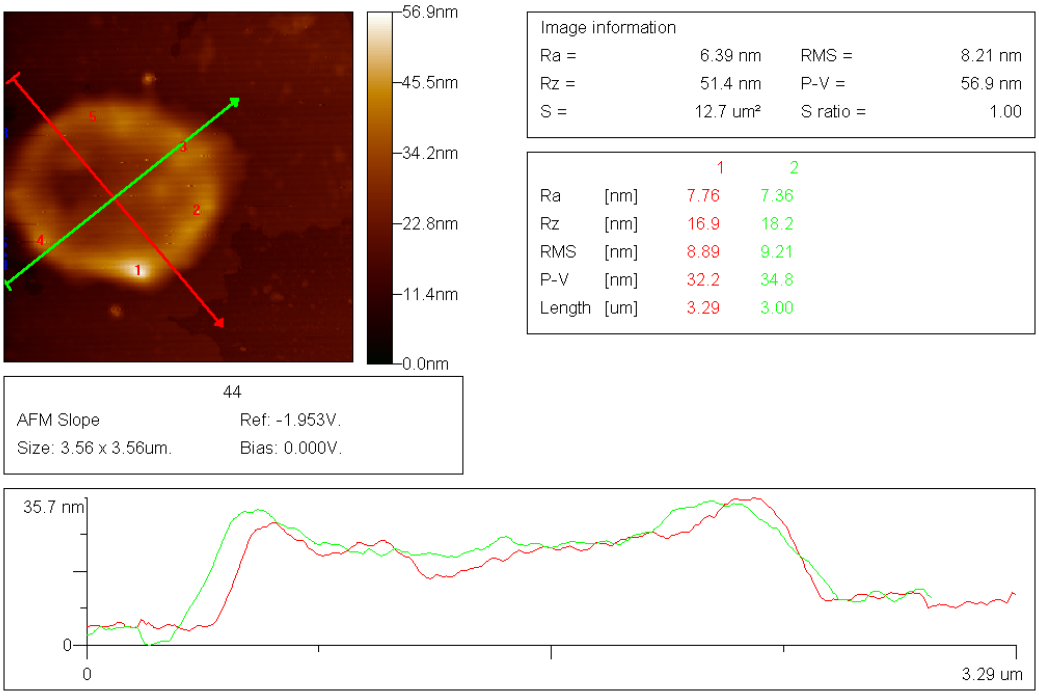

Figure 4-10. AFM of an RLLLSA particle showing its compressibility, which is characteristic of a more fluid vesicle.

To demonstrate this fluidity, RLLLSA particles were sonicated to create smaller particles that would, in theory, be exchanging peptide more rapidly due to the higher temperature. Immediately after sonication, the particles were placed on a TEM grid surface and flash-frozen in liquid nitrogen. The grid was then desiccated overnight to

remove any residual moisture prior to staining with uranyl acetate. When viewed, the TEM grid is covered in small RLLLSA particles that are connected to each other by small extensions that exclude stain and are presumably peptide(**Figure 4-11**), creating "beads on a string" that have also been observed in the transitions of KLVFFAE from particles into fibrils (Childers, Anthony et al. 2012).

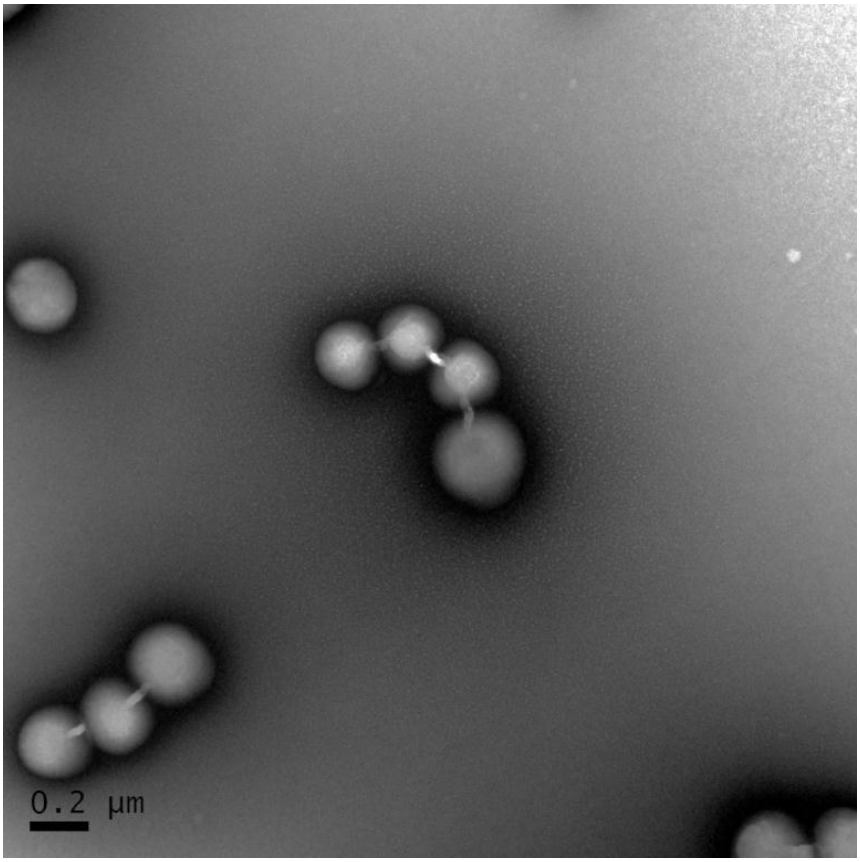

Figure 4-11. TEM of RLLLSA particle "pearls" after sonication and flash-freezing in liquid nitrogen. Extensions between the particles that also exclude stain suggest that these are rapidly exchanging peptides at higher temperatures.

While the RLLLSA sequence forms particles, I wanted to understand what forces would drive it to self-assemble into a more fibril-like morphology. Even at very high concentrations (10mM), the RLLLSA peptide remains stable as a large non-crystalline particle. I predicted that by adding a complementary charge onto the C-terminus of the sequence it would recapitulate the charge-hydrophobic-charge pattern of KLVFFAE and would be more likely to self-assemble at lower concentrations due to the ability to now form a stabilizing salt-bridge (**Figure 4-12**).

Figure 4-12. Sequence comparisons of the (left) KLVFFAE peptide at neutral pH and (right) RLLLSAE peptide at neutral pH drawn as antiparallel β-sheets with favorable electrostatic interactions highlighted in red.

The RLLLSAE peptide was synthesized, purified and allowed to incubate in 40% CH_3CN/60% H_20 at neutral pH for 1 week at concentrations of 1mM, 5mM and 10mM. At lower concentrations, the RLLLSAE peptide formed particles 5x smaller than those formed by RLLLSA under the same conditions (**Figure 4-13**).

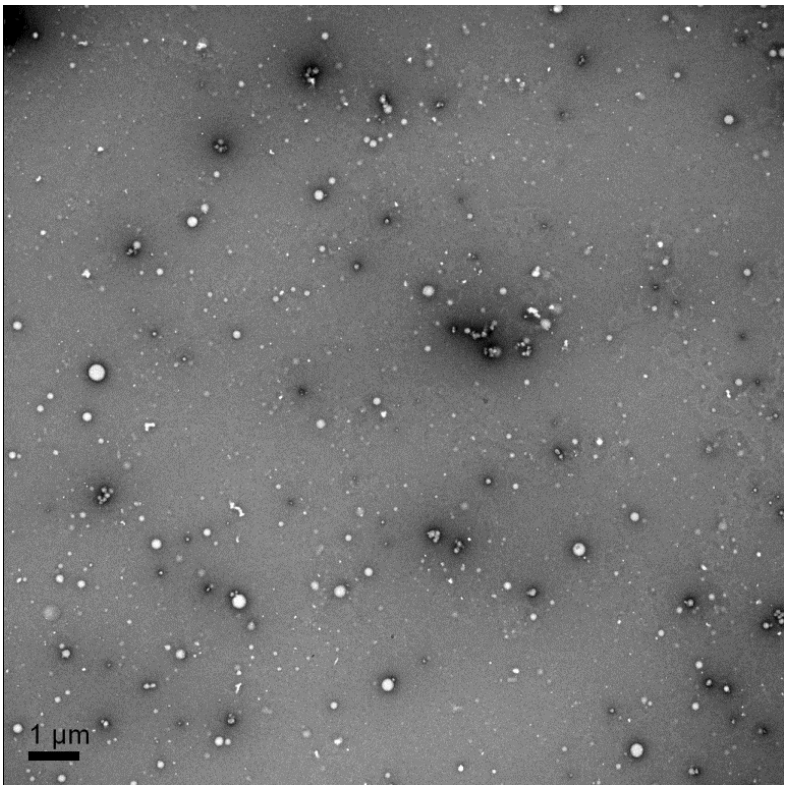

Figure 4-13. TEM of RLLLSAE particles assembled at 1mM at neutral pH for 1 week.

However, for both the 5mM and 10mM samples, the RLLLSAE peptide self-assembles into large sheets with varying widths that were microns in length (**Figure 4-14**). The ability of this peptide to form sheets with extended lamination at much lower concentrations than its parent sequence demonstrates the importance of electrostatic interactions to forming more crystalline aggregates.

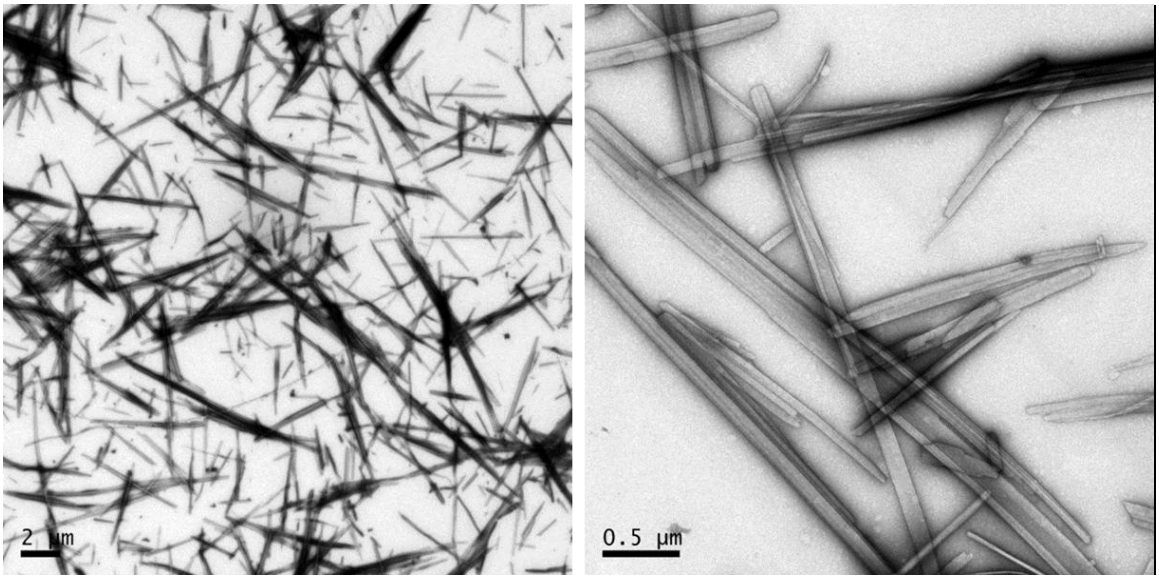

Figure 4-14. TEM of large RLLLSAE sheets assembled at 5mM at neutral pH for 1 week at low magnification (left) and high magnification (right).

Other variants of the RLLLSA sequence were synthesized to determine if the length of the sequence or the nature of the hydrophobic residues was important. The Ser residue was mutated to Leu and Val and the resulting peptides still formed particles, though of much smaller size (50-200nm) than the parent RLLLSA sequence (**Figure 4-15**) (1-5µm). The Leu triad in the core of the peptide was also extended by a Leu, Ala or Val and, similarly to the previous modifications, resulted in particles that were stable but with smaller diameters (20-150nm).

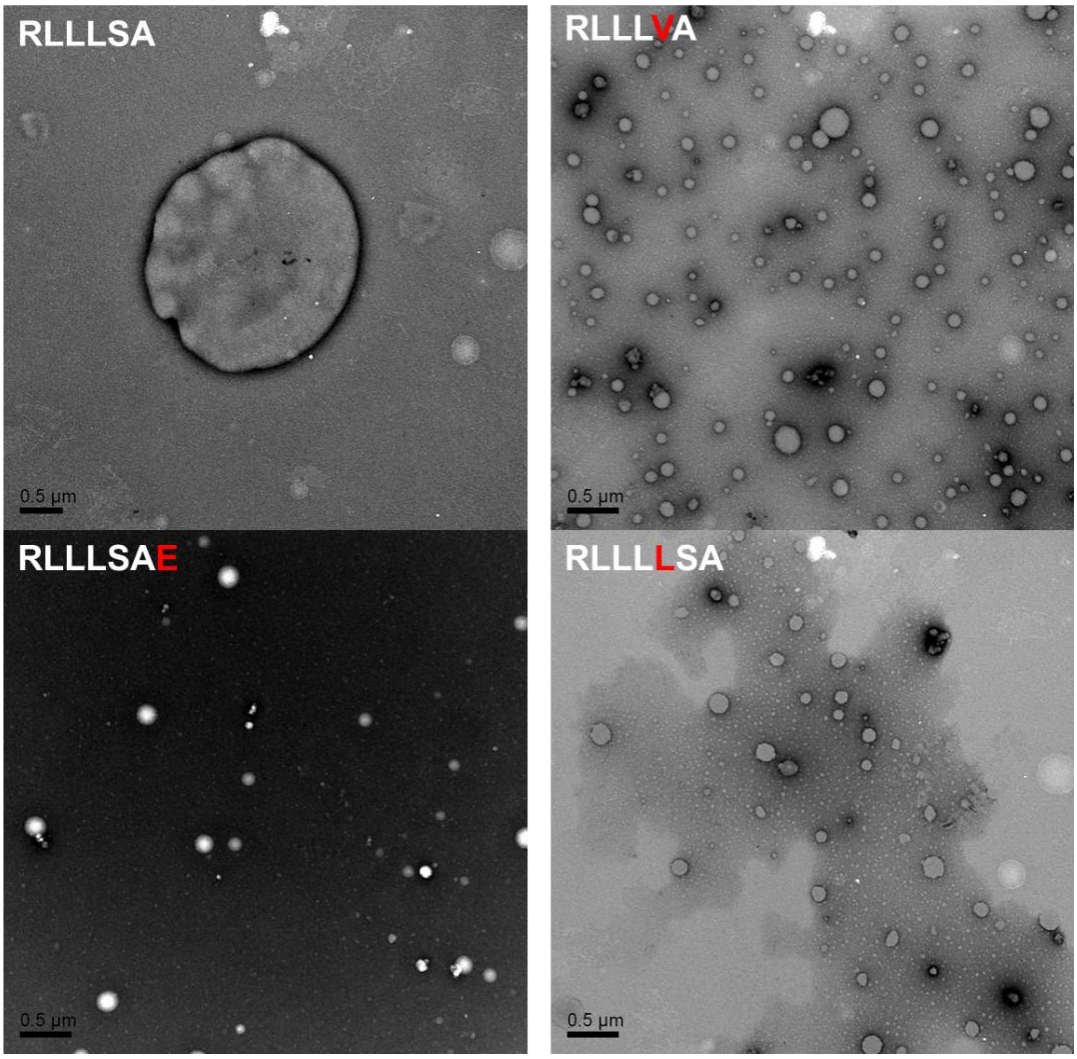

Figure 4-15. TEMs of particles formed from the parent RLLLSA peptide as well as representative particles formed by RLLLSAE, RLLLVA and RLLLLSA at 1mM at neutral pH for 1 week.

The ability of these variant sequences to assemble into particles suggests that the conservation of the Arg-Leu-Leu-Leu core sequence is sufficient to maintain the particle morphology.

Discussion

In this chapter, I show that the individual fragments from the GPBS can access multiple morphologies that are distinct from those formed by the GPBS blades. While it has been shown by Dobson and others that native protein folds can form amyloid under certain conditions (Chiti and Dobson 2009), my data demonstrates that these protein fragments can access crystalline amyloid morphologies, but also others, such as non-crystalline particles, that are now gaining more attention in the literature. Since the full-length blade assembles into fibrils and the sequences at position A, such as IYAMHW, also assemble into fibrils, I propose that this position may dominate the assembly process in some way with its morphology being the only one maintained and propagated. The sequences in the C position, such as KLIIWD, have a propensity for assembling into structures with extended lamination which could contribute to blade-to-blade packing interactions in the full-length β-propeller protein fold. The sequences in the D position are much more soluble than those from any other position and do not readily aggregate, supporting the notion that it plays a role in minimizing edge hydrophobic interactions and contributing to overall protein solubility.

The sequences in the B position and D positions that have similar amphipathic character self-assemble into large spherical particles that can change size in response to temperature, as well as retain this dynamic non-crystalline form for extended periods of time. These particles have heterogeneous distributions of peptide in their core and can be compressed to form concavities similar to concave

lipid vesicles. Several sequence variants of RLLLSA also form particles and have unique phase properties that allow them to be trapped by fast changes in their surrounding temperature. The dynamic nature of these B strand sequences may provide for conformational flexibility within the context of the fully-folded propeller structure. The position of the B strand is near the core of the propeller and, with the A strand position able to participate in metal or ligand binding, the ability of the B strand to access multiple conformations may absorb the impact of changes within the protein core upon ligand binding.

The ability of sequences from positions A, B, C to aggregate correlated with their predicted aggregation propensities. The Aggrescan server used to calculate these propensities is only a measure of general aggregation and is not specific to determining if the sequence will form amyloid. This proved to be useful in my experiments as many of the sequences aggregated but not all formed amyloidogenic morphologies. Determining the characteristics that lead to aggregation and those specific forces leading to an amyloid packing arrangement would allow us to better define the landscape of amyloid assembly since we now have examples of short aggregation-prone peptides that are stable without forming a cross-β crystalline structure. It is also important to recognize that the nature of the individual peptide sequences do not necessarily correspond to their nature when part of a larger protein fold. The length of the sequence and the surrounding amino acids can greatly alter the properties of the peptide sequence and also its potential for aggregation.

The variety of the morphologies observed for the fragments of GPBS suggest that the aggregation of any part of the GPBS could result in a heterogeneous mixture

of protein aggregates, each with potentially different interactions with their environment or other peptides. Since there are several fragments of the GPBS that do form amyloid fibrils, I proposed that these would be the most likely portions of the propeller fold to act as templates to nucleate the amyloid β peptide, leading to amyloid fibrils with different conformations. With the prediction that the A strand sequence, which forms fibrils similar to the full-length blade, being the nucleating core of the propeller blade sequence, it should be the most likely to be able to template Aβ(16-22), the nucleating core of amyloid β. Using the well-characterized Aβ(16-22), I can now use these propeller fragments as seeding agents to determine which strands are the most likely to seed amyloid growth.

Materials and Methods

All chemicals were purchased from Sigma-Aldrich (St. Louis, MO) unless stated otherwise.

Peptide Synthesis and Purification

All peptides used were synthesized using standard FMOC solid-phase peptide synthesis (SPPS) protocols with both N- and C-termini capped using microwave synthesis (CEM Liberty Peptide Synthesizer, North Carolina, USA). The peptides were cleaved from the solid support using a cleavage cocktail of TFA/anisole (95/5, v/v). The resulting solution was filtered from the resin and precipitated using excess chilled anhydrous ethyl ether. The centrifuged pellet was dried under house vacuum before purification. They were purified by reverse-phase HPLC (RP-HPLC) to greater than 99% and their mass was confirmed using TOF-MALDI mass spectrometry. Capped blade and hairpin sequences from the G-protein crystal structure (PDB: 1A0R) were synthesized using the same SPPS protocols and were purified and confirmed using previously described methods.

Peptide Assembly Conditions

For assembly, the peptides were dissolved in 40% acetonitrile/60% water to a final concentration indicated. pH was adjusted to near pH 7.0 using pH paper and the solutions were allowed to mature at room temperature for the indicated time periods. To rapidly dissolve the peptide, the suspension was vortexed at high speed for 30s and sonicated at 40kHz in a room temperature water bath for 1-2min. This process

was repeated 3-4 times till the solution was clear, generally requiring less than 20 min to ensure complete dissolution.

Transmission Electron Microscopy

Samples were allowed to adsorb on a TEM grid (carbon/copper) for at least 1 min. Excess peptide solution was wicked away with filter paper. A 2-wt % uranyl acetate solution was added to TEM grids and incubated for 3-5 minutes before wicking away. Samples were then placed in a desiccator overnight. TEM micrographs were recorded with a Hitachi 7500 TEM at magnifications ranging from 2000x to 200,000x with a Tungsten filament at an accelerating voltage of 75 kV.

Circular Dichroism Spectroscopy

Samples (30 μL) were placed into a quartz cuvette with a 0.1 mm path length (Starna Cells). Each spectrum was obtained by scanning wavelength from 300 nm to 185 nm at a scanning rate of 100 nm/min with a resolution of 0.2 nm using a Jasco J-810 spectropolarimeter. For each CD run temperature was controlled at 20°C, unless otherwise stated. Prior to recording the presented final wavelength scan CD at 215 nm was recorded for approximately 15-minute period to ensure sample had stabilized at the CD measurement conditions. Three successive wavelength scans were averaged for each sample. Buffer control spectra were averaged and subtracted from the sample spectra.

UV/Vis Spectroscopy of Congo Red Binding

A stock solution of Congo Red dye was prepared at 1mM at neutral pH. This was added to solutions of 1mM peptide assemblies for a final CR concentration of 25μM. Samples were incubated for 30 minutes and then the UV/Vis spectra were recorded

Fourier-Transform Infrared Spectroscopy

Sample aliquots (300μL) were centrifuged for 30 minutes at 13,000 rpm and frozen in a bath of dry ice and acetonitrile bath (-40°C) for 20 minutes before lyophilizing overnight. The IR spectra were acquired using a Jasco FT-IR 4100 ATR with a diamond crystal at room temperature and averaging 256 scans with $4cm^{-1}$ resolution. Background spectra were acquired immediately before each sample and were subtracted from each sample spectrum.

Atomic Force Microscopy

Sample aliquots (10 μL) were incubated for 3 min. at room temperature on a silicon chip (TedPella, Inc.) which was first cleaned by sonicating in methanol for 30 min. A JEOL JCPM-4210 scanning probe microscope was used for imaging. The silicon cantilever (NSC12/50 purchased from MikroMasch) had a resonant frequency of 315 kHz. Samples were imaged by AFM tapping mode with a filter of 0.2 Hz and at a scan clock of 0.1667 ms. WinSPM software (system version 407) was used to analyze the image, providing the height information.

Chapter 5

β-Propeller Fragments Alter the Morphology of Aβ(16-22)

Introduction

As discussed in Chapter 1, pure Aβ(16-22) can assemble into a variety of morphologies, including small or large particles (Childers, Anthony et al. 2012), fibrils (Balbach, Ishii et al. 2000), ribbons (Lu, Jacob et al. 2003) or nanotubes (Lu, Jacob et al. 2003). This assembly process from single monomers aggregating and then organizing themselves into these morphologies occurs in an environmentally-dependent manner and is sensitive to solvent polarity, pH, salt concentration and temperature (Lu, Jacob et al. 2003; Dong, Lu et al. 2006; Mehta, Lu et al. 2008; Childers, Anthony et al. 2012). The amyloid β peptide *in vitro* can be nucleated by other entities (exogenous nucleation), such as macromolecules or biochemical interfaces, or exclusive self-nucleation. For example, a single amino acid change within the amyloid-forming peptide Sup35 can prevent amyloid propagation in a mixed system, supporting that there must be a certain degree of complementarity between the peptide sequence of the nucleating species and the sequence of the monomer that is templated by the nucleus (Santoso, Chien et al. 2000; Chien, DePace et al. 2003). A variety of surfaces can result in a very specific sequence or molecular-level conformation to be nucleated. In the context of amyloid β, the peptide can begin to aggregate at very low concentrations (<400μM) at an air-water interface (Anthony, Lynn et al. 2012). In the presence of a templating surface, the rate of amyloid β assembly can be increased (either a fragment of a mature fibril or a

mixed interface), and the peptide always assembled into fibrils, although their length can be attenuated by rocking the sample during incubation(Wu, Bowers et al. 2010). All of these examples demonstrate that amyloid assembly is dependent on its environment. In the last chapter, I showed that the A strand of the GPBS was able to self-assemble into a similar morphology as the full-length blade, similar to how the Aβ(16-22) peptide is able to self-assemble into a similar fiber morphology as Aβ(1-42). If the A strand is the nucleating core of the blade, I predict that it would have the highest likelihood of templating Aβ(16-22). In this chapter, I test if the pre-assembled β-strands of the GPBS are sufficient templates for the nucleation of Aβ(16-22) assembly.

Results

Aβ(16-22) Monomers Interact with Preassembled GPBS β-Strands

As outlined in **Figure 5-1**, to determine if interactions could occur between amyloid β(16-22) and the fragments of the G Protein β Subunit (GPBS), 500μM Aβ(16-22), a concentration below its critical assembly concentration, was mixed with each fragment at neutral pH and room temperature and allowed to incubate for 45 days. To break up any preformed aggregates, prior to mixing Aβ(16-22) was first dissolved in HFIP and concentrated to dryness *in vacuo*. The fragments from GPBS were allowed to mature for 2 weeks before 10 minutes sonication to fragment the assemblies before being added to freshly dissolved Aβ(16-22) (**Figure 5-1**). The

assemblies formed by the fragments are tabulated in Table 4-1 and represent fibers (A), particles (B), sheets (C) and no assembly (D).

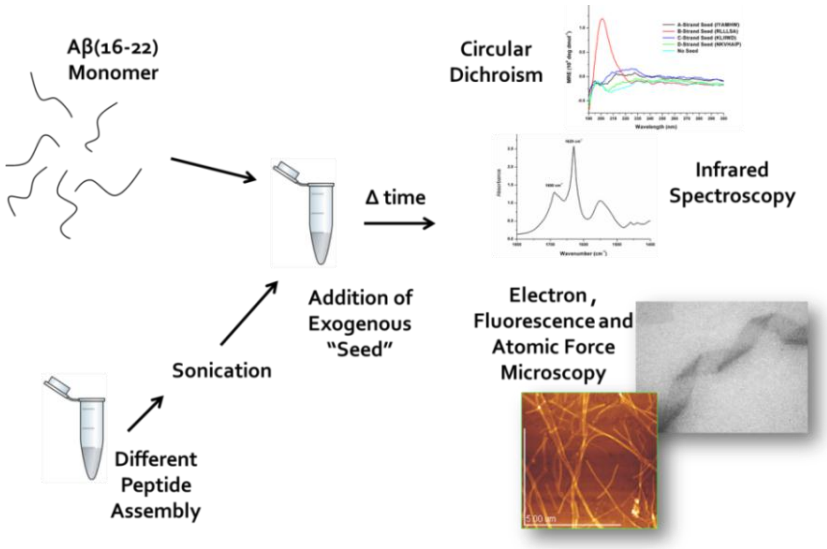

Figure 5-1. Procedure for mixing Aβ(16-22) with exogenous peptide seeds.

As shown in **Figure 5-2**, a significant increase in positive ellipticity is observed at 200nm after 10 days of co-incubation. This transition has proven to be diagnostic of early assembly, and, with longer incubation, the negative ellipticity transition at 215nm of β-sheet secondary structure begins to appear (**Figure 3**).

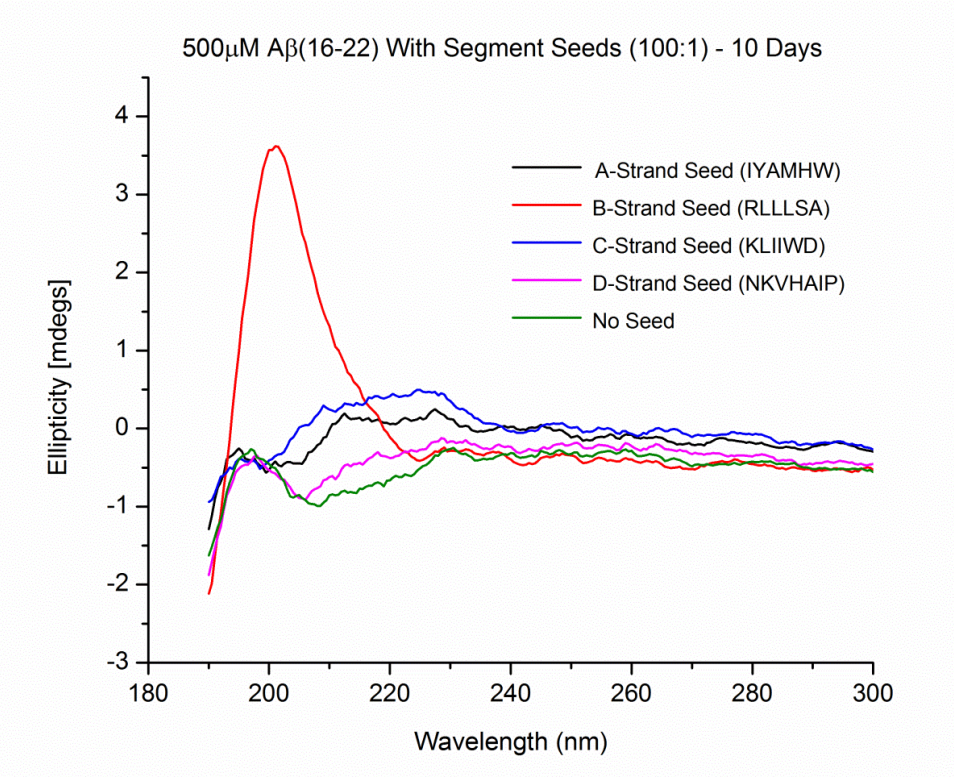

Figure 5-2. CD of 500μM Aβ(16-22) monomer with the addition of each strand, A, B, C and D, from the GPBS, assembled as shown in Figure 5-1 at room temperature, pH 7.0 for 10 days.

After 45 days, the characteristic CD β-sheet signature had grown significantly of (**Figure 5-3**) the B strand RLLLSA seeded Aβ(16-22).

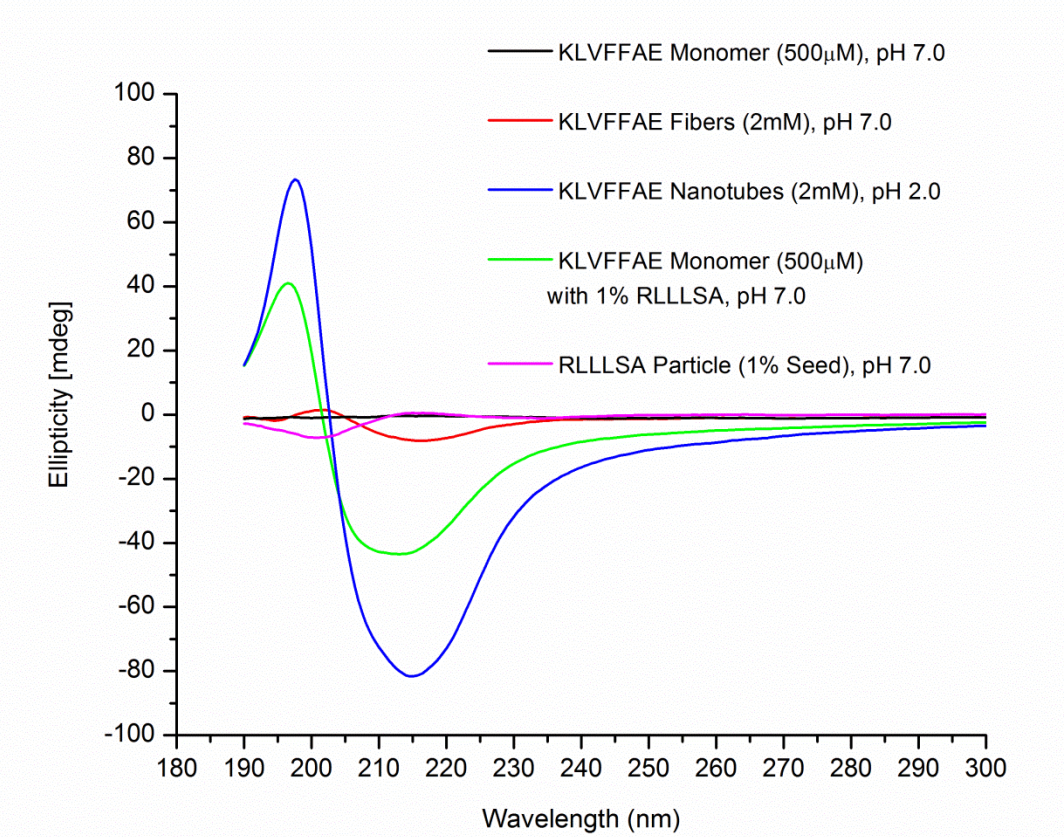

Figure 5-3. CD spectra of Aβ(16-22) peptide, unassembled at 500μM (black), 2mM fibers at pH 7.0 (red) and 2mM nanotubes at pH 2.0 (blue) and 1% of 4mM CH_3CO-RLLLSA-NH_2 seed (magenta). The mixture of unassembled Aβ(16-22) at 500μM with 1% CH_3CO-RLLLSA-NH_2 seed (green) at pH 7 has a similar β-sheet signature as Aβ(16-22) at pH 2.0 assembled into tubes.

The large decrease in the ellipticity at 215nm and increase around 195nm can be correlated with extended lamination of β sheet secondary structure, similar to what is observed for the nanotubes formed by Aβ(16-22) at pH 2.0 (blue in **Figure 5-3**) (Lu, Jacob et al. 2003). There were no observable morphologies as visualized by TEM for the Aβ(16-22) mixtures of the A, C and D strands. In contrast, the TEM of the

Aβ(16-22) with RLLLSA sample revealed large nanotube structures that were evenly dispersed across the sample grid (**Figure 5-4b**).

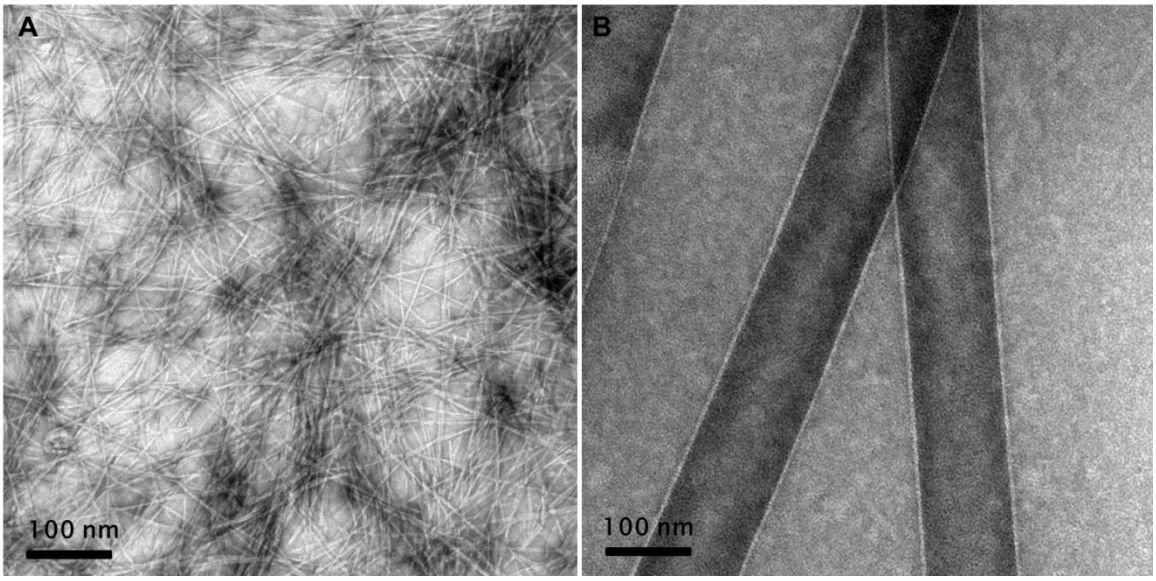

Figure 5-4. TEM of 2mM Aβ(16-22) fibers at pH 7.0 (a) and 1mM Aβ(16-22) mixed with 1% RLLLSA particles at pH 7.0 (b) showing formation of large hollow nanotubes. Samples are stained using uranyl acetate (2wt%). The tubes capture the stain on their interior.

TEM revealed that this mixture of Aβ(16-22) monomers and RLLLSA particles leads to the formation of peptide nanotubes, characterized by the parallel white lines of the tube walls that exclude stain. Previously, the nanotubes formed by Aβ(16-22) at pH 2.0 were shown to be 52 nm in diameter (Lu, Jacob et al. 2003), whereas the nanotubes formed by mixing Aβ(16-22) with RLLLSA particles are much larger in dimension with diameters as great as 150nm (**Figure 5-5b**) .

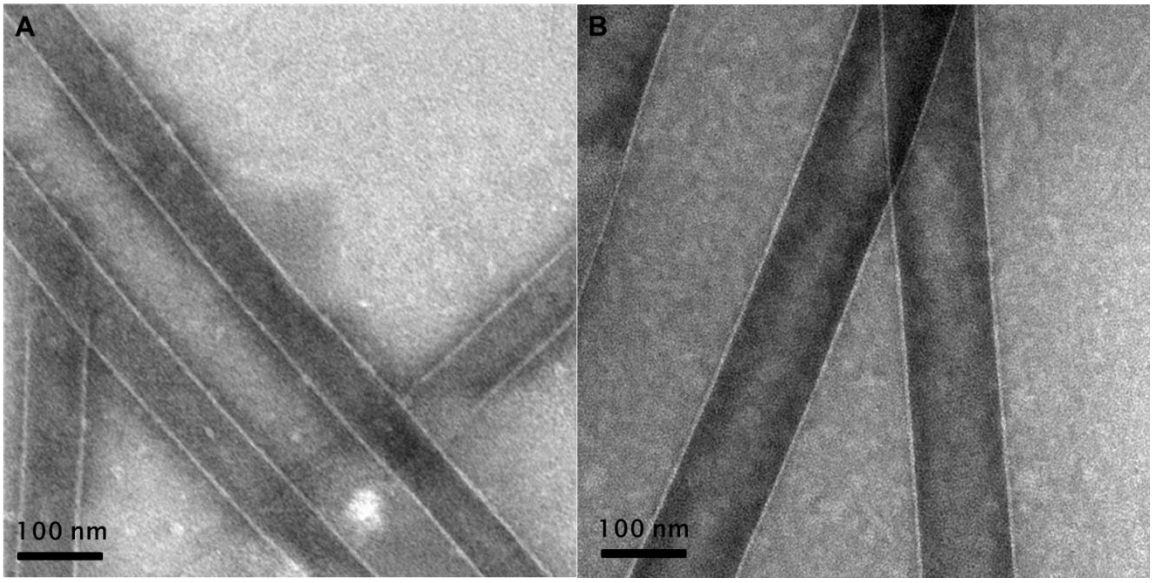

Figure 5-5. TEM of 1mM Aβ(16-22) nanotubes formed at pH 2.0 (a) and 1mM Aβ(16-22) mixed with 1% RLLLSA particles forming nanotubes at pH 7.0 (b).

Because the sizes of the nanotubes were not the same as those formed by Aβ(16-22) at acidic pH, oriented electron diffraction was used to determine if there was a difference in the tilt angles between the pure and mixed nanotubes (**Figure 5-6**). The hydrogen-bonding distance and the lamination distances were calculated from the two sets of arcs using this data. Lines were drawn to define the cross-β arc sets corresponding to the diffraction originating from the top and bottom walls of the nanotubes and the tilt angle was determined by measuring the angle between each pair of cross-β arcs and the tube long-axis.

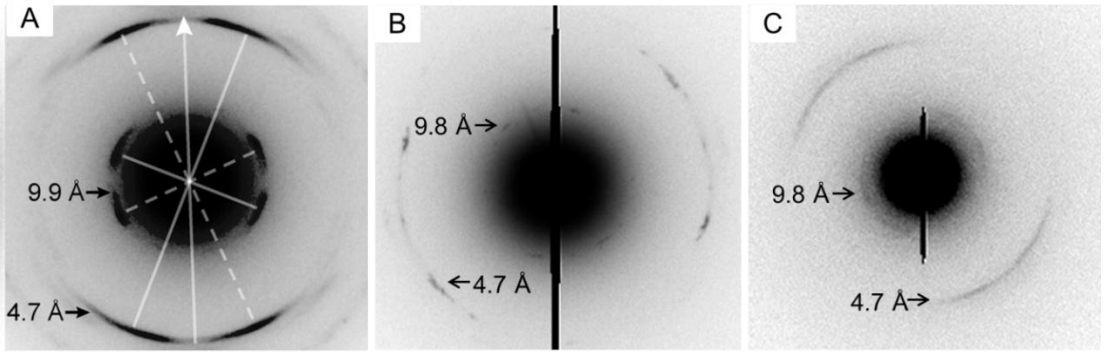

Figure 5-6. Electron diffraction of Aβ(16-22) nanotubes formed at pH 2.0 with a tilt angle of 25°±2 (a), Aβ(16-22) nanotubes formed by mixing with 1% RLLLSA particles with a tilt angle of 29°±2 (b) and Aβ(16-22) nanotubes formed by mixing with 10% RLLLSA particles with a tilt angle of 31°±2. Tilt angles were determined as the angle between each pair of cross-β arcs and the nanotube long axis.

The percentage of RLLLSA particles added to the Aβ(16-22) peptide monomer was varied to test the effect on morphology. The concentration of Aβ(16-22) was increased to 1mM because this concentration resulted in tubes with shorted incubation times of two weeks, and the molar percentage of RLLLSA was evaluated from 1% to 50% (**Figure 5-7**). These structures are over an order or magnitude larger compared to the fibers typically observed under these conditions and slightly larger than the tubes formed at pH 2.0 by pure Aβ(16-22). The fibers formed by Aβ(16-22) at pH 7.0 are 5-10nm in diameter due to fewer β-sheets laminating together. As more RLLLSA peptide is added, the diameters of the tubes decreases from around 150nm for the 1% RLLLSA sample to around 65nm for the 50% RLLLSA sample. For the 1% RLLLSA sample, there were at least two populations of nanotubes with different

diameters. This was the only RLLLSA:Aβ(16-22) ratio where two different tube sizes were observed. The population of the smaller sized tubes (B in Figure 5-7) was slightly greater than that of the larger sized tubes (A in Figure 5-7).

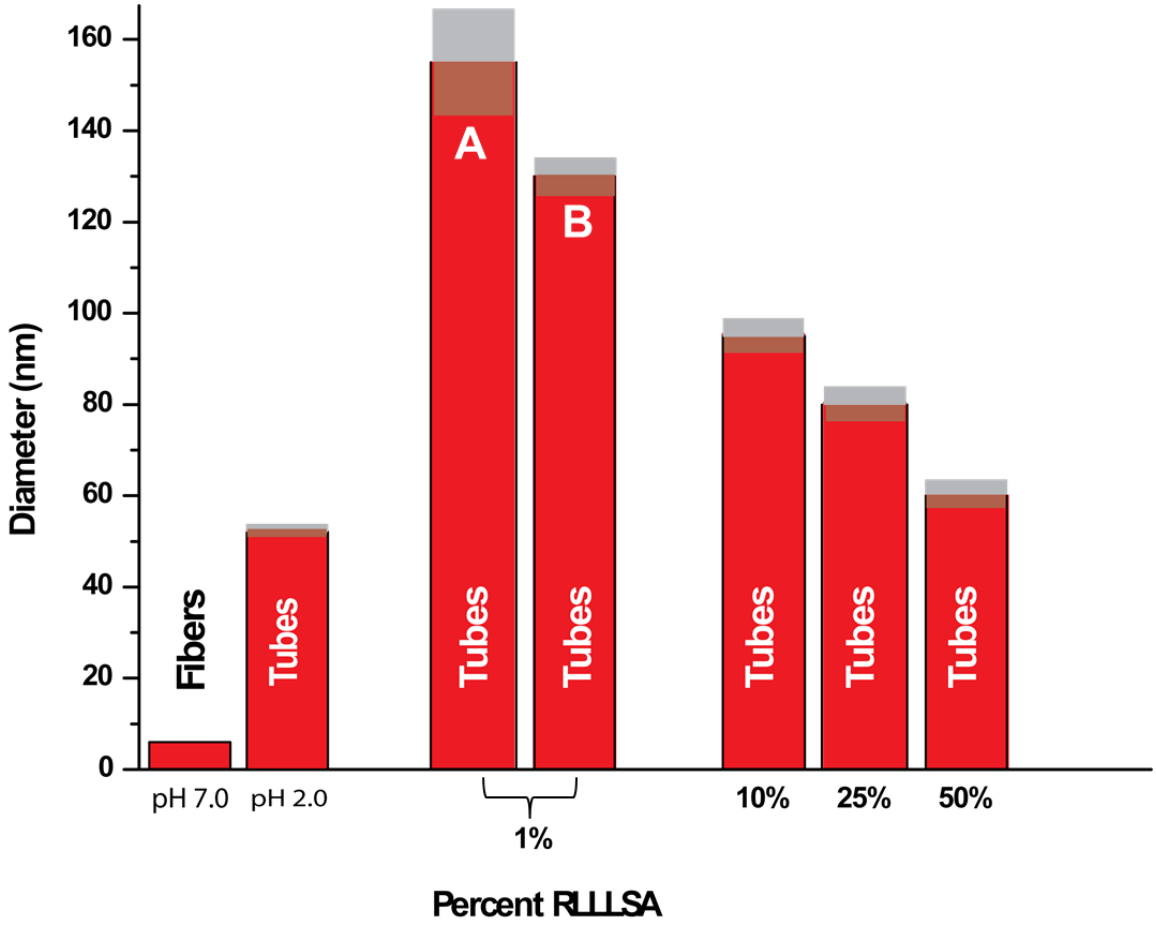

Figure 5-7. Diameter of nanotubes as a function of RLLLSA added to 1mM unassembled Aβ(16-22). Gray bars indicate the range of measured dimensions from TEM widths that were converted into diameter.

RLLLSA Monomers Do Not Seed Aβ(16-22) Tubes

To determine if the formation of the nanotubes was dependent on the addition of preincubated RLLLSA particles, RLLLSA peptide was dissolved in HFIP and allowed to dry before solvating. The RLLLSA was then mixed with varying concentrations of both HFIP treated Aβ(16-22) as well as sonicated Aβ(16-22) fibrils. RLLLSA forms particles very quickly (as soon as 5 minutes following solvation), though they are small (200-300nm) compared to those incubated for 1 week (**Figure 4-6**). As shown in **Figure 5-8**, small particles are observed soon after solvation in the 1% Aβ(16-22) sample. When the percent of sonicated Aβ(16-22) fibrils added is increased, only fibrils are observed under these conditions, with no nanotube formation observed by TEM at any ratio. The RLLLSA samples mixed with Aβ(16-22) monomer and those mixed with sonicated Aβ(16-22) fibrils yielded similar results.

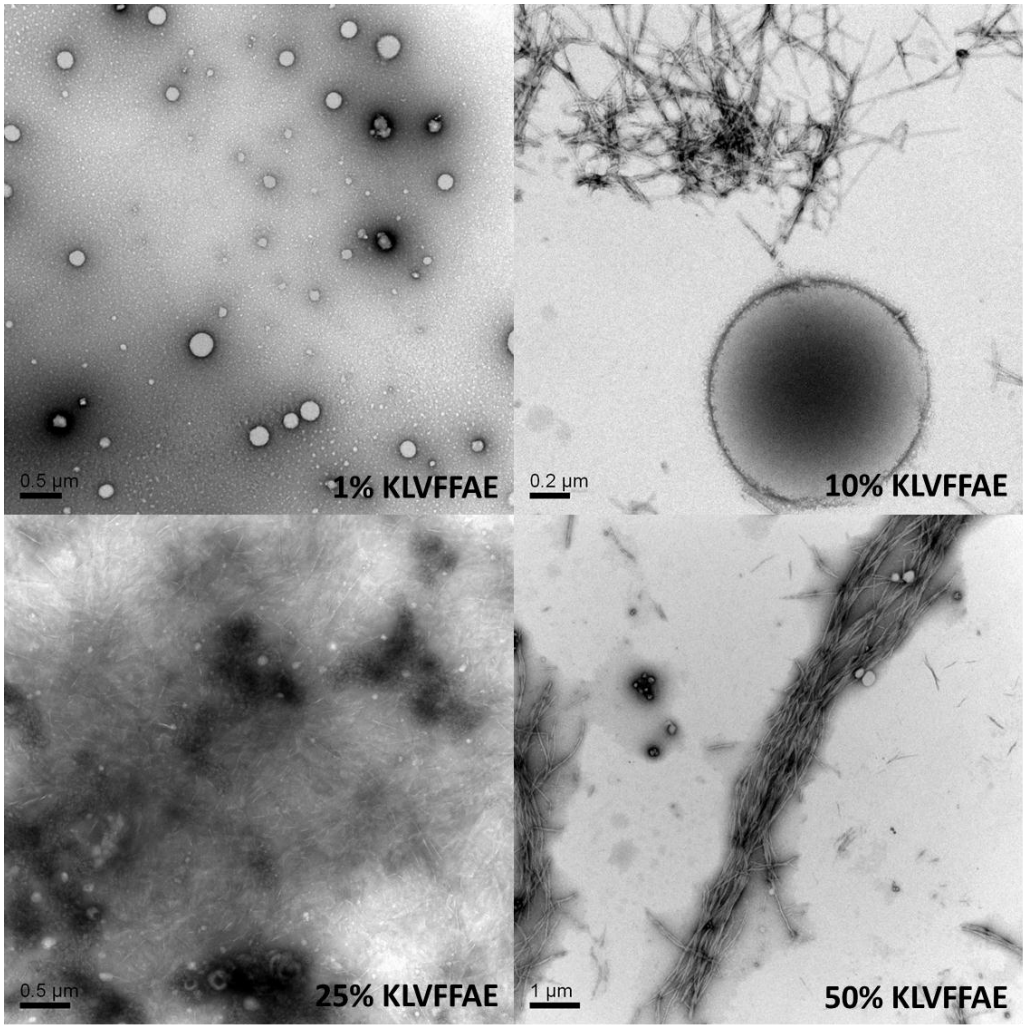

Figure 5-8. TEMs of 1mM RLLLSA monomer with 1%, 10%, 25% and 50% molar percent added of sonicated Aβ(16-22) fibers after 2 week incubation at neutral pH.

RLLLSA Particles Transform Mature Aβ(16-22) Fibrils

To test the effect of the RLLLSA particles on mature Aβ(16-22) fibrils, which are thermodynamically stable, 25% RLLLSA particles, mature at 2 weeks, were added to a solution of mature 2mM Aβ(16-22) assembled as fibrils at 2 weeks

incubation and neutral pH. The mixture appears as segregated fibers and particles after several hours (**Figure 5-9c**). The mixture becomes more heterogeneous after 4 days, with particles no longer adopting a spherical morphology (**5-9d**). After 8 days, ribbons are observed by TEM, though the majority of the sample remains as fibrils (**5-9e**). After 30 days incubation, the ribbons have transitioned into nanotubes, as shown in **Figure 5-9f**.

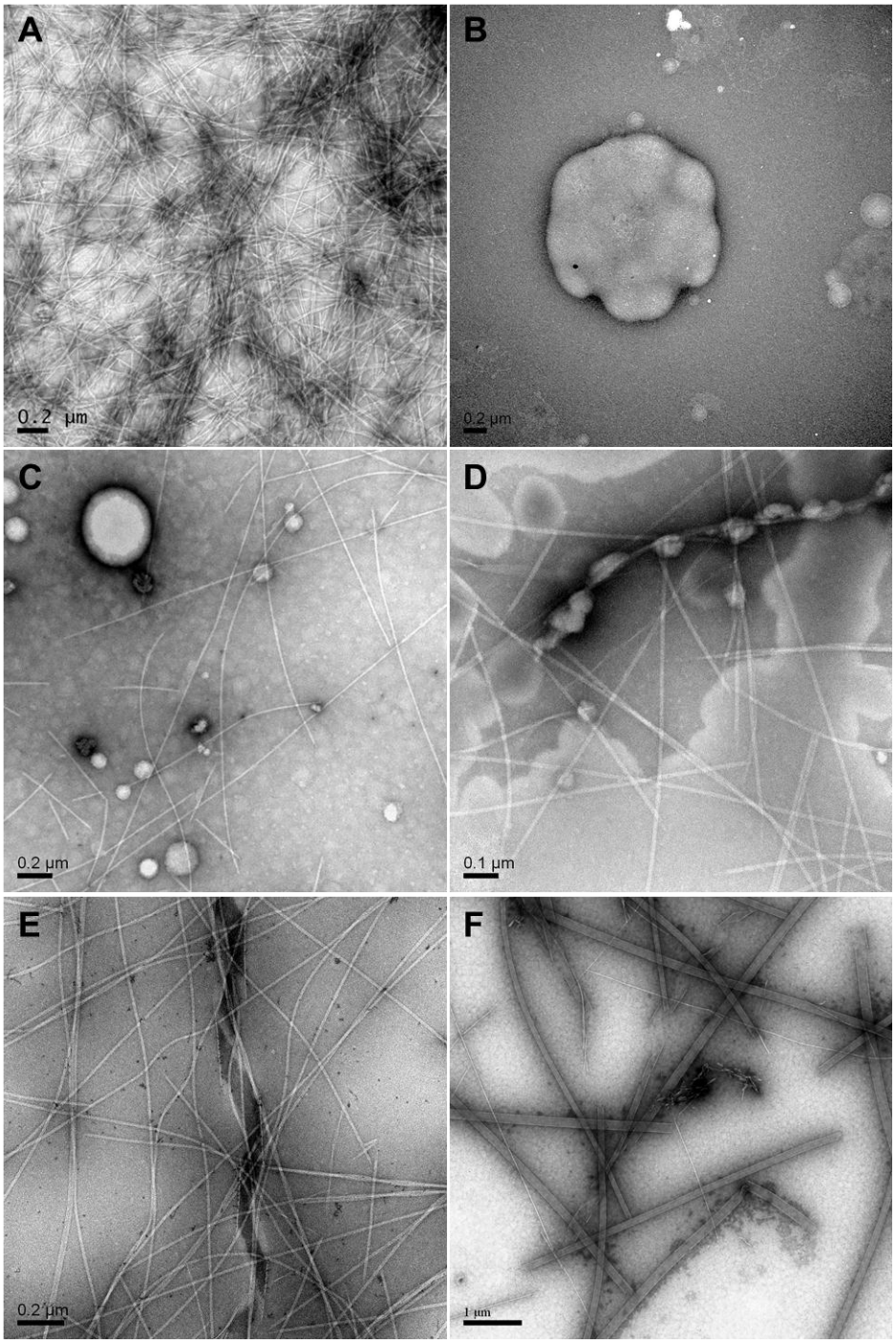

Figure 5-9. TEMs showing the effect of mixing mature 2mM Aβ(16-22) fibrils (a) with 25% sonicated RLLLSA particles (b). Time points are four hours (c), four days (d), eight days (e) and 30 days (f). Aβ(16-22) fibrils were prepared at 2mM in 40%

CH_3CN/60% H_2O at neutral pH and incubated for 2 weeks at room temperature. RLLLSA particles were prepared at 4mM in 40% CH_3CN/60% H_2O at neutral pH and incubated for 2 weeks at room temperature. The particles were sonicated prior to mixing hence their smaller size in the TEM after 4 hours.

To further compare the mixed tubes to those previously described in our lab (Lu, Jacob et al. 2003; Dong, Lu et al. 2006; Mehta, Lu et al. 2008; Childers, Mehta et al. 2010; Ni, Childers et al. 2012), atomic force microscopy (AFM) was used to measure the height of the tubes. AFM of the mixed tubes gives heights of the tubes averaging 8.3±0.6nm, which is similar to that observed for the pure Aβ(16-22) nanotubes at acidic pH (**Figure 5-10**), suggesting that, similar to Aβ(16-22) nanotubes, the peptides within these nanotube may be in a bilayer arrangement (Childers, Mehta et al. 2010).

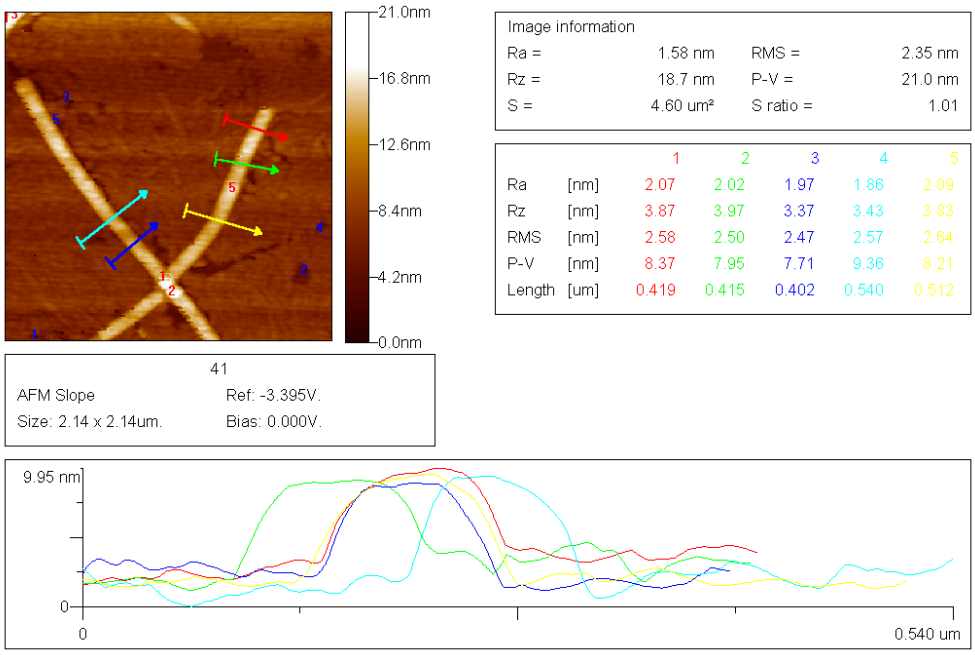

Figure 5-10. AFM of the 10% RLLLSA mixed nanotubes showing the height values (P-V) to be approximately 8nm.

To determine the registry of the peptides within these nanotubes, a ^{13}C was incorporated at the F19 carbonyl position within the Aβ(16-22), KLVFFAE, sequence. When a ^{13}C carbonyl is incorporated into a peptide, the FTIR signal of the peptide secondary structure is split with both ^{12}C and ^{13}C amide I stretches. The observed splitting is dependent on a tightly coupled the hydrogen-bonded oscillator network is and changes in the $^{12}C/^{13}C$ frequency splitting can be used to determine if another peptide is incorporated to dilute the oscillator network (Petty and Decatur 2005; Decatur 2006). This F19 peptide was assembled into nanotubes at pH 2.0, which have been shown to have peptides within the β-sheet oriented in an antiparallel, out-of-register arrangement (**Figure 5-11, bottom**), and fibers at pH 7.0,

which are antiparallel in-register β-sheets (**Figure 5-11, middle**). When the KLV[1-^{13}C]FFAE peptide was mixed with 10% RLLLSA and allowed to form nanotubes after 2 weeks incubation at pH 7.0, the FTIR spectrum of the mixed tubes resembled most closely the spectrum of the pH 7.0 fibers (**Figure 5-11, top**), showing that they share the same peptide registry.

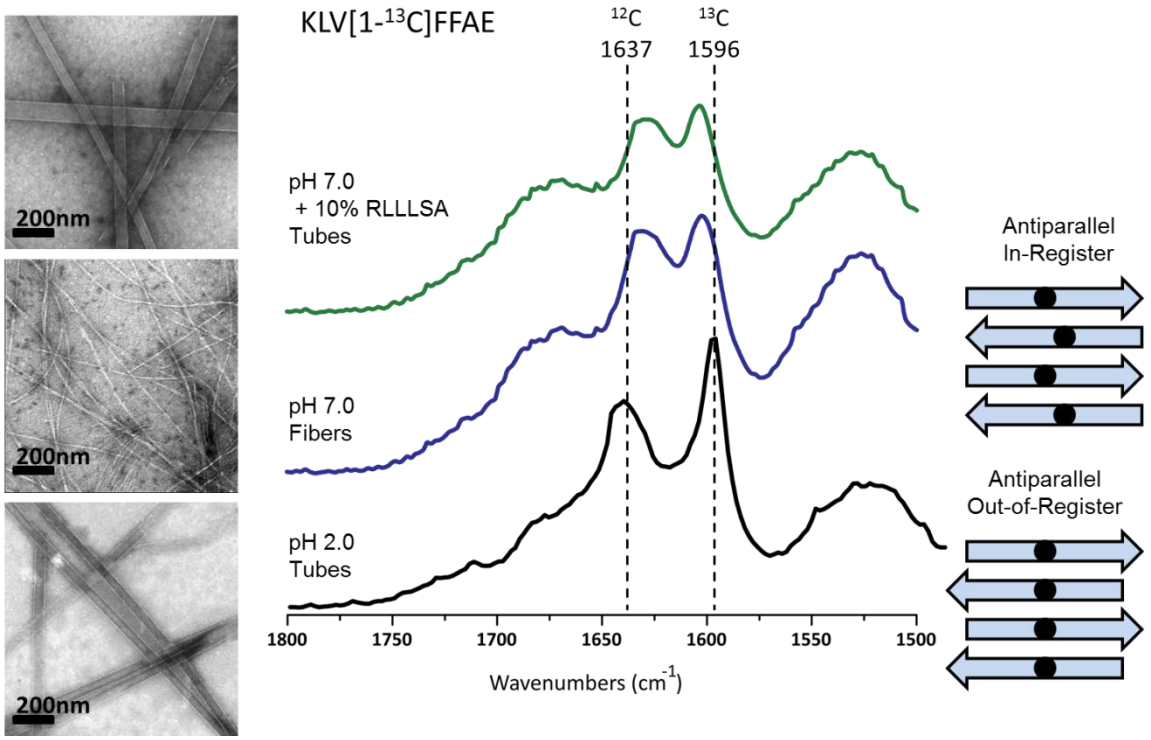

Figure 5-11. Isotope-edited FTIR of KLV[1-^{13}C]FFAE tubes formed by incubating for 2 weeks at pH 2.0 (bottom), fibers formed by incubating for 2 weeks at pH 7.0 (middle) and tubes formed by mixing with 10% unlabeled RLLLSA and incubating for 2 weeks at pH 7.0 (top). Insets are TEMs of the morphologies prior to taking the IR spectra. Because of the location of the ^{13}C carbonyl at the F19 position, the labels are only aligned when in an antiparallel out-of-register arrangement, shown on the bottom right. When the peptides are antiparallel in-register, the ^{13}C carbonyls are no

longer as tightly coupled, leading to a decreased frequency splitting between the ^{12}C and ^{13}C peaks.

The thermostability of the fibers and mixed tubes was measured as a function of temperature by following the 215nm β sheet signature by CD. Tubes formed in mixing experiments have a melting temperature (T_m) of 63.8±0.3°C, that is below that of the fibers (84.3±0.2°C), but still higher than pure Aβ(16-22) nanotubes formed at pH 2.0(39.8±0.9°C)(**Figure 5-12**).

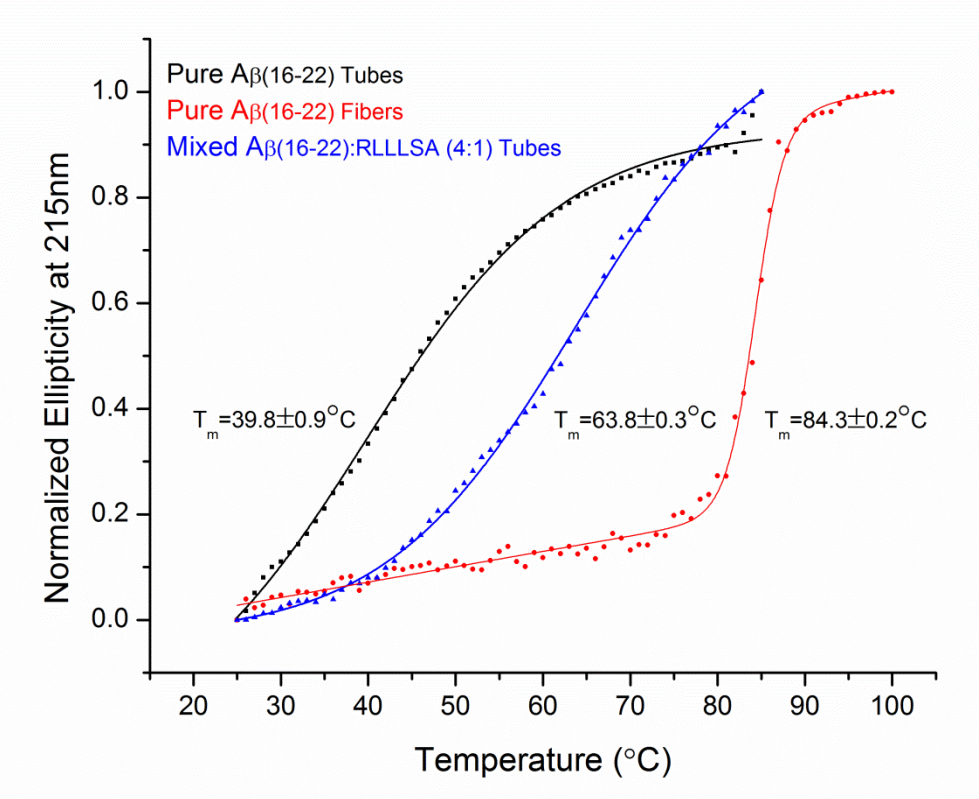

Figure 5-12. Melting curves of assemblies as monitored by CD ellipticity at 215nm of pure Aβ(16-22) fibrils at neutral pH (red), pure Aβ(16-22) tubes (black) and mixed

Aβ(16-22):RLLLSA (4:1) tubes at neutral pH (blue). Curves were fit using the sigmoidal form of the Boltzmann model to acquire the T_m of each structure.

The mixed tubes are also sensitive to the addition of salts, such as Na_2SO_4. After adding 20mM SO_4^{2-} to mature mixed tubes, the tubes disintegrate into ribbons and particles after only 4 hours (**Figure 5-13**). This experiment shows that the tube morphology is still dynamic and responsive to its environment, as well as suggesting an important role of electrostatic interactions within the mixed tube.

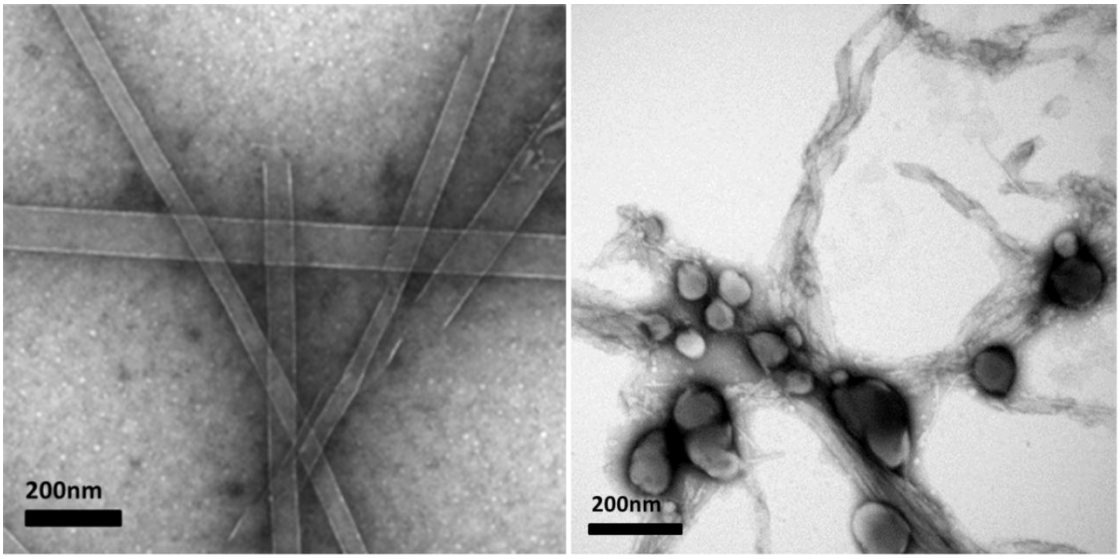

Figure 5-13. TEM of (left) 10% RLLLSA and 1mM Aβ(16-22) mixed tubes after 1 month incubation and (right) the same tubes 4 hours after addition of 20mM Na_2SO_4.

After 2 days, the mixture of ribbons and particles transitions into a mixture of particles and fibers as observed by TEM (**Figure 5-14**). Though the salts were not removed using dialysis, previous experiments with RLLLSA monomer suggest that these would not necessarily be able to transition back into tubes. The reversibility of this process merits future exploration.

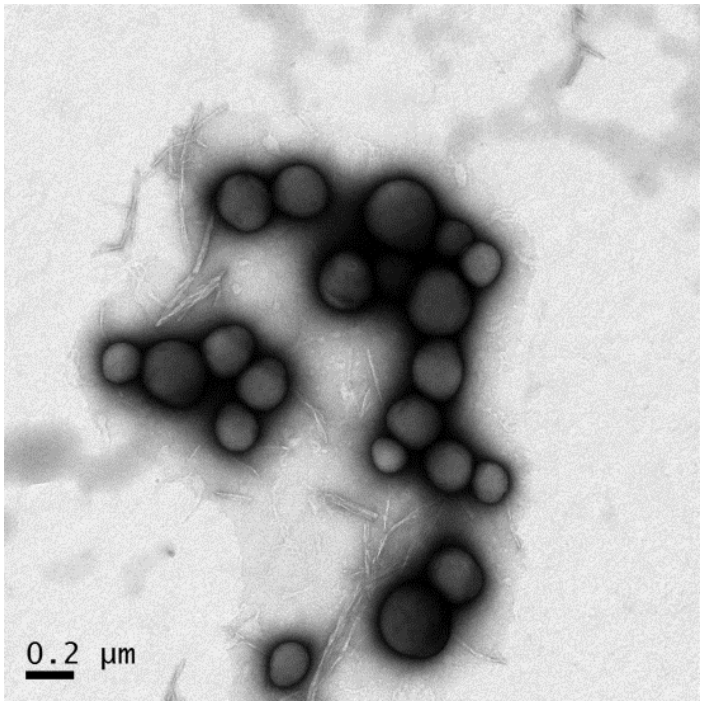

Figure 5-14. TEM of 10% RLLLSA and 1mM Aβ(16-22) mixed tubes after 2 days of incubation in 20mM Na_2SO_4.

Discussion

In the previous chapter, I showed that the β-strands taken from the GPBS are able to self-assemble into different morphologies. To evaluate the ability of these β-

strands to template Aβ(16-22), these assembled GPBS fragments were mixed with Aβ(16-22). Here, I show that when mixed, particles that assemble from the B strand (RLLLSA) of the GPBS change the morphology of Aβ(16-22) both above and below the critical aggregation concentration from fibrils to nanotubes under conditions where only fibers are observed. No assembly is observed when mixing Aβ(16-22) with assemblies of peptides from strand A, C or D, which either assemble into fibril or sheet structures (A and C) or do not assemble at all (D). Because the fibril and sheet morphologies are retained after sonication and prior to addition to the Aβ(16-22) monomer, this is consistent with a more molten, non-crystalline particle morphology being necessary for the conversion of Aβ(16-22) from fibers into nanotubes. The size of the nanotubes formed is much larger than those observed by assembling pure Aβ(16-22) at acidic pH, which may be due to the RLLLSA peptide changing the tilt angle of the initial peptide arrangement, which could be correlated to the final diameter of the nanotubes. Further characterization of the tilt angles of the different mixing ratios would need to be done to confirm this correlation. There was not a significant correlation between the size of the particle added and the final dimension of the nanotubes which may mean that the general properties of the particle may play a role in modulating the initial nanotube nucleus that leads to the propagation of structures with increased β-sheet lamination.

The size of the tubes is correlated to the ratio of RLLLSA to Aβ(16-22), with smaller diameter tubes forming at higher RLLLSA concentrations. These data suggest that this may be due to the RLLLSA peptide associating more with itself at higher concentrations, potentially lowering the number of interactions with Aβ(16-

22). It may also be due to differences in particle size upon equilibration in the solution containing Aβ(16-22), though this has not been thoroughly characterized. I also show that the RLLLSA monomer is not able to transform either the Aβ(16-22) monomers or fibers into nanotubes, with the sample remaining stable as fibers. This points to the necessity of having a preformed RLLLSA particle for the morphological transformation to occur. The preformed particles appear to be required for Aβ(16-22) desolvation leading to a nucleus that allows for extended lamination of the nanotube morphology.

Amazingly, RLLLSA particles are able to not only transform Aβ(16-22) into nanotubes, but are also able to transform mature Aβ(16-22) fibrils. The gradual shift in global morphology from fiber to ribbon to nanotubes suggests that this process occurs by a change in the equilibrium between the monomer free in solution and the monomer that is packed into the fiber structure. I propose that, as more monomer is sequestered by the RLLLSA particle, the peptide in the fibers begin to dissociate from the structure to return to solution. It is possible that the pKas of the Aβ(16-22) side chains are altered when the peptide is sequestered into the core of the RLLLSA particle, making it possible to access the out-of-register arrangement observed in the nanotubes formed at acidic pH. Eventually, all of the Aβ(16-22) peptide is fully converted into the stabilized nanotube morphology. If this is true, it should be possible in the future to fluorescently label the Aβ(16-22) peptide and follow the conversion from fibrils to monomer to particle and back to the nanotube by fluorescence microscopy to fully characterize this proposed pathway.

The AFM heights of the mixed nanotubes are similar to those of other nanotubes characterized in our group that are shown to have the peptides packing into a bilayer conformation (Mehta, Lu et al. 2008; Childers, Mehta et al. 2010). Though not as thermostable as the pure Aβ(16-22) fibers, the mixed tubes are more stable than the pure Aβ(16-22) nanotubes formed at pH 2.0. Aβ(16-22) is known to self-assemble into fibrils that are very thermodynamically stable, typically with melting temperatures around 85°C, which is much higher than most natively-folded proteins. This stability is hypothesized to be a result of the cross-β structure composed of repeated electrostatic complementation and hydrophobic packing within the β-sheet laminates. These fibrils need to be subjected to harsh conditions in order to be broken apart, such as the addition of denaturants or use of sonication. The mild conditions needed to change the conformation through mixing are in stark contrast to the extreme methods typically required to disrupt the fibril's conformation. The melting curves for Aβ(16-22) tubes and the mixed tubes were much less cooperative than the curve for the fibers, which may be due to the tubes having a much larger hollow region in their core and many more laminates than the fibers. The less cooperative melt of the mixed tubes could be the product of equilibration between different structures during each degree change during the experiment, which would be indicative of a more heterogeneous mixture.

The mixed tubes appear to be sensitive to the addition of salt, which highlights electrostatic interactions as being vital to the structural integrity of the nanotubes. The Arg of the RLLLSA peptide could interact with the Glu of the Aβ(16-22) sequence (KLVFFAE). This stabilizing electrostatic interaction would be

sensitive to both pH changes as well as added salt ions. This is an interesting parallel to the Aβ(16-22) fibers, which, as discussed in Chapter 1, are formed by stabilizing electrostatic interactions at neutral pH. The removal of these interactions by a pH change results in the peptide reorganization into nanotubes at acidic pH. My data show that the core electrostatic interactions as seen in the Aβ(16-22) fibers may still be intact, with the sheets now being able to access extended lamination that is observed in the nanotubes. The importance of electrostatic interactions is investigated in more detail in Chapter 6. These experiments are a demonstration of the shallow energy landscape for amyloid assembly and may provide a simple model for understanding the heterogeneity observed in amyloid plaques. Two models of the peptides mixing during assembly are discussed in Chapter 6—one in which the RLLLSA peptide is distributed evenly throughout the nanotube structure and one in which there are local nucleating pockets of RLLLSA formed, leading to growth of nanotubes from the aggregate that are elongated via monomer addition to the template from solution(Liang, Guo et al. 2008).

Materials and Methods

All chemicals were purchased from Sigma-Aldrich (St. Louis, MO) unless stated otherwise.

Peptide Synthesis and Purification

All peptides used were synthesized using standard FMOC solid-phase peptide synthesis (SPPS) protocols with both N- and C-termini capped using microwave synthesis (CEM Liberty Peptide Synthesizer, North Carolina, USA). The peptides were cleaved from the solid support using a cleavage cocktail of TFA/anisole (95/5, v/v). The resulting solution was filtered from the resin and precipitated using excess chilled anhydrous ethyl ether. The centrifuged pellet was dried under house vacuum before purification. They were purified by reverse-phase HPLC (RP-HPLC) to greater than 99% and their mass was confirmed using TOF-MALDI mass spectrometry. Capped blade and hairpin sequences from the G-protein crystal structure (PDB: 1A0R) were synthesized using the same SPPS protocols and were purified and confirmed using previously described methods.

Peptide Assembly Conditions

For assembly, the peptides were dissolved in 40% acetonitrile/60% water, and except where indicated, to a final concentration of 1.0 mM unless otherwise stated. pH was adjusted to near pH 7.0 using pH paper and the solutions were allowed to mature at room temperature for the indicated time periods. To rapidly dissolve the peptide, the

suspension was vortexed at high speed for 30s and sonicated at 40kHz in a room temperature water bath for 1-2min. This process was repeated 3-4 times till the solution was clear, generally requiring less than 20 min to ensure complete dissolution.

For a monomer pool, the purified peptide was dissolved in HFIP to disrupt any preformed nuclei and then the solvent was evaporated using N_2 gas. The peptide monomer was resuspended at a concentration of 1mM (except where indicated) in a 40% acetonitrile/60% water solution that was then adjusted to pH 7.0 using minimal 500μM NaOH. Mature assemblies were sonicated for 20 minutes and then the molar percentage indicated of each was added to the resuspended Aβ(16-22) monomer. The solutions were incubated at room temperature for a minimum of 2 weeks and assembly progress was monitored by TEM and CD signatures at 200nm and 215nm.

Circular Dichroism Spectroscopy

Samples (30 μL) were placed into a quartz cuvette with a 0.1 mm path length (Starna Cells). Each spectrum was obtained by scanning wavelength from 300 nm to 185 nm at a scanning rate of 100 nm/min with a resolution of 0.2 nm using a Jasco J-810 spectropolarimeter. For each CD run temperature was controlled at 20°C, unless otherwise stated. Prior to recording the presented final wavelength scan CD at 215 nm was recorded for approximately 15-minute period to ensure sample had stabilized at the CD measurement conditions. Three successive wavelength scans

were averaged for each sample. Buffer control spectra were averaged and subtracted from the sample spectra.

Transmission Electron Microscopy

Samples were allowed to adsorb on a TEM grid (carbon/copper) for at least 1 min. Excess peptide solution was wicked away with filter paper. A 2-wt % uranyl acetate solution was added to TEM grids and incubated for 3-5 minutes before wicking away. Samples were then placed in a desiccator overnight. TEM micrographs were recorded with a Hitachi 7500 TEM at magnifications ranging from 2000x to 200,000x with a Tungsten filament at an accelerating voltage of 75 kV.

Atomic Force Microscopy

Sample aliquots (10 μL) were incubated for 3 min. at room temperature on a silicon chip (TedPella, Inc.) which was first cleaned by sonicating in methanol for 30 min. A JEOL JCPM-4210 scanning probe microscope was used for imaging. The silicon cantilever (NSC12/50 purchased from MikroMasch) had a resonant frequency of 315 kHz. Samples were imaged by AFM tapping mode with a filter of 0.2 Hz and at a scan clock of 0.1667 ms. WinSPM software (system version 407) was used to analyze the image, providing the height information.

Chapter 6

Peptide Particles Allow for Extended Lamination of Aβ(16-22)

Introduction

The ability of the RLLLSA peptide particles to change the morphology of the mature Aβ(16-22) fibers prompted evaluation of the mechanism for this change to understand the molecular-level interactions that would lead to a shift in supramolecular morphology. In the previous chapter, it was shown that addition of sequences that form sheets, such as those in position C, and sequences that form fibrils, such as those in position A, to Aβ(16-22) do not result in nanotube formation. One possibility is that these structures have a smaller surface on which the Aβ(16-22) monomer can be templated. For instance, the fibrils may only be able to template hydrogen-bonded addition of monomer at their ends. Likewise, the sheets, though larger in dimension than the fibrils, may also have a limited template surface at the ends of the structure. In comparison, the micron-sized RLLLSA particles are more fluid than the previous morphologies and are spherical, both properties leading to a much larger surface area for possible interactions with the Aβ(16-22) monomer.

In Chapter 4, I showed that the peptide particles displayed properties similar to lipid vesicles. The RLLLSA sequence is composed of a charged residue followed by a relatively hydrophobic set of residues, giving it similar properties to an amphipathic lipid molecule which is also characterized as having a hydrophilic head group connected to a hydrophobic tail. In a simple model, the Arg guanidinium group could be extended, creating a more lipid-like peptide amphiphile (**Figure 6-1**).

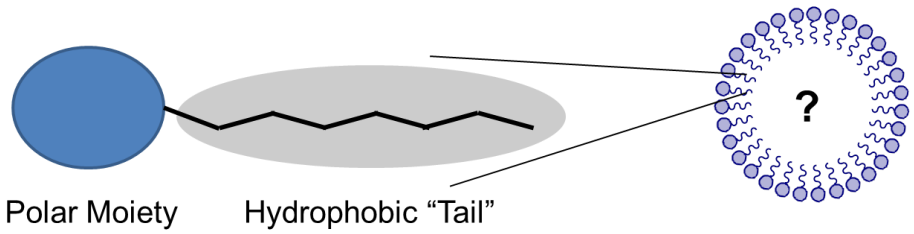

Figure 6-1. Model of the amphiphilic nature of RLLLSA and similar B strand sequences.

Other B strand sequences from the GPBS and the congeners, shown in Chapter 4, also contain a charged head-group residue and a set of hydrophobic or less polar amino acids. The observation that all of these sequences also assemble into vesicle-like structures lead me to question whether or not these structures were hollow or if they contained internal layers of alternating polarity similar to multilamellar lipid vesicles previously characterized in the literature (Hope, Bally et al. 1985; Mayer, Hope et al. 1986; Jousma, Talsma et al. 1987; Hoffmann, Thunig et al. 1994; Bergenholtz and Wagner 1996; Viard, Gallay et al. 2001; Lei and MacDonald 2003). Lipid vesicles have been well-studied in bioengineering, therapeutic development and materials science because of their dynamic properties and their ability to self-assemble. They have predictable transitions as well as the ability to trap small molecules while retaining their fluidity, allowing for diffusion. I predicted that due to their more dynamic nature, the peptide particles provide a unique environment for the Aβ(16-22) monomer to diffuse and desolvate in order to pack into a crystalline nucleus capable of being propagated into a nanotube.

Examining the details of this process would allow us to determine if the particle is only providing an environment for desolvation or if the RLLLSA peptide sequence is actually interacting with the Aβ(16-22) monomer directly to aid in the formation of a new nucleating species. As shown in blue in **Figure 6-2**, the Aβ(16-22) monomer undergoes hydrophobic collapse at a critical concentration and forms spherical particles. Given time, the peptide within the particle can pack to form a nucleating core which is then propagated from the particle as monomers associate with the newly-formed template. When RLLLSA particles are added (red in **Figure 6-2**), there are several possible outcomes for the mixture of the two species. In one case, the RLLLSA particles may nucleate their own structures, distinct from that of the Aβ(16-22). The Aβ(16-22) monomers may desolvate within the RLLLSA particles to create a particle with mixed composition. The RLLLSA peptides within the mixed particle may interact directly with the Aβ(16-22) monomer yielding a mixed nucleus that is propagated as a mixed structure (bottom of **Figure 6-2**). The RLLLSA particle may not interact directly with the Aβ(16-22) as a pure nucleus forms and propagates, but may be incorporated into the final structure as a heterogeneous region within the nanotube, shown in the bottom right of **Figure 6-2**. The particles may also be excluded from the final Aβ(16-22) structure, but may still have hydrophobic associations with the surface of the structures (middle right of **Figure 6-2**).

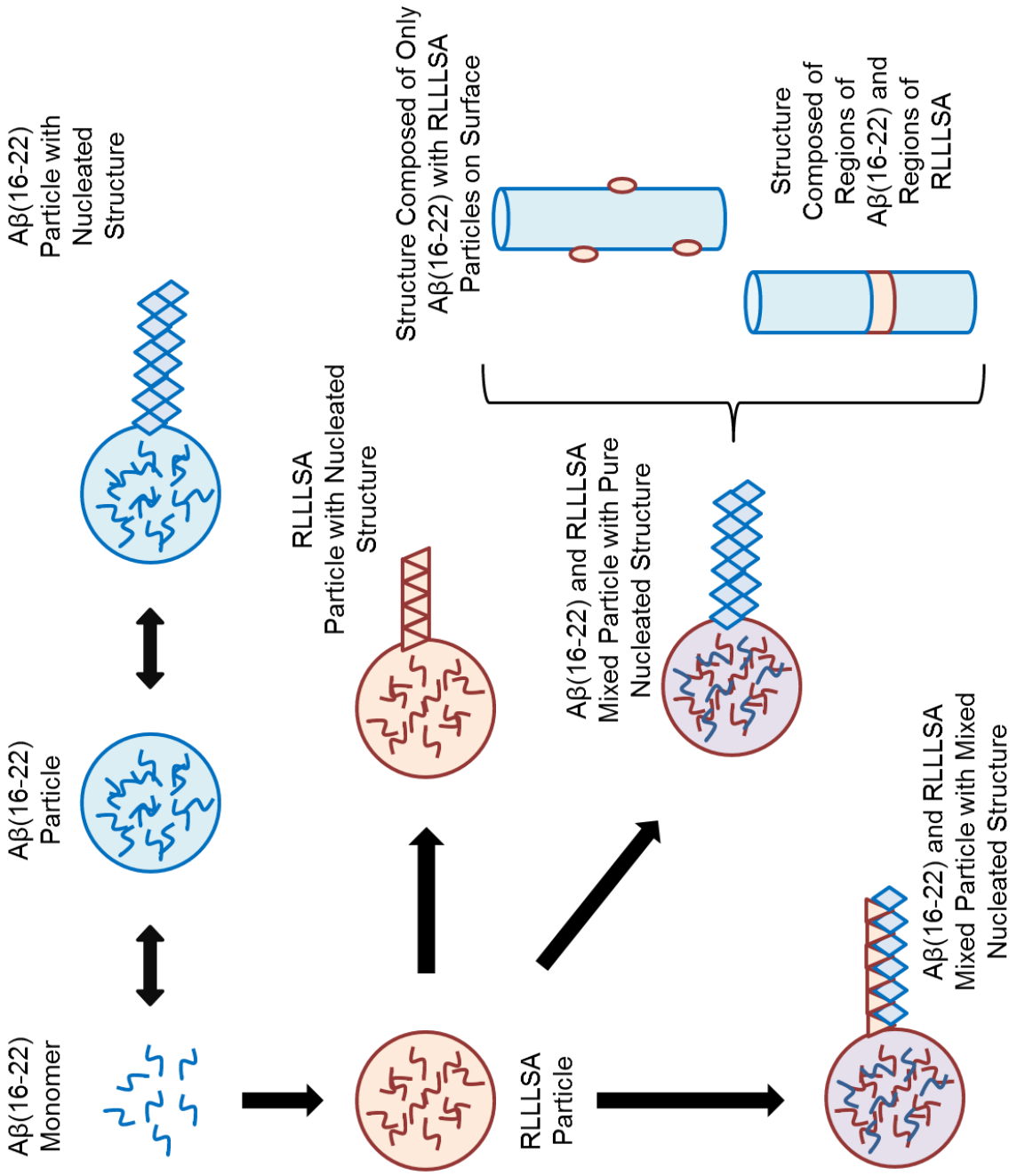

Figure 6-2. Models of possible interactions between Aβ(16-22) and RLLLSA particles.

In this chapter, I show that the RLLLSA particles can trap small molecules and are correlated with the formation of the nanotubes shown previously, though there is no evidence that they are incorporated into the structure.

Results

RLLLSA Particles Remove Rhodamine Dye from Solution

To determine if the peptide particles could be used to trap small molecules, similar to lipid vesicles (Hope, Bally et al. 1985). The positively-charged Rho110 was chosen over other dye molecules because its charge would not interact with the positively-charged Arg side chain, leaving the remaining possible interactions to be hydrophobic interactions and solvent capture. A solution of 20μM Rhodamine 110 dye was prepared and the nanotubes and particles were both added to this stock solution. As shown in **Figure 6-3**, after incubation with the RLLLSA particles for an hour, the intensity of the absorbance at 498nm decreased appreciably, with almost all of the dye being removed during centrifugation with the 2mM RLLLSA particles. When the Rho110 was centrifuged and the UV/Vis spectrum recorded after this, there was no significant change in the intensity of absorbance at 498nm, consistent with the dye remaining in solution and not getting spun down (**Figure 6-3**). When mature KLVFFAL nanotubes were incubated with the Rho110 solution for 1 hour and then centrifuged, the UV/Vis absorbance intensity at 498nm did not change significantly, supporting that the positively-charged dye does not readily interact with the positively-charged nanotube surface. The peptide nanotubes formed by Aβ(16-22)

E22L can be centrifuged to separate them from the supernatant. The peptide particles are also large enough to be centrifuged to remove them from the supernatant.

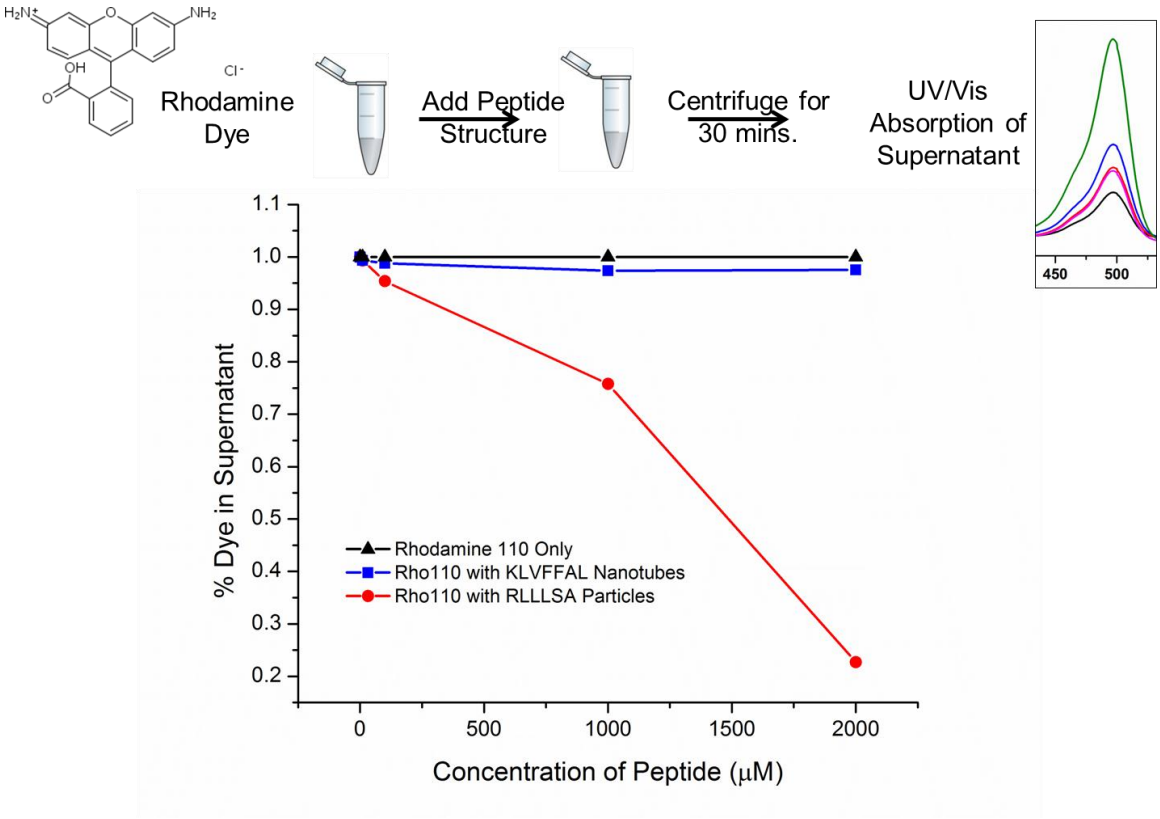

Figure 6-3. Spin-down experiment plotted as a function of the percent of Rho110 dye remaining after centrifugation of Rho110 dye alone (black), Rho110 incubated with KLVFFAL nanotubes (blue) and Rho110 incubated with RLLLSA particles (red). Rhodamine 110 dye was prepared at 20μM and the peptide concentrations for KLVFFAL tubes and RLLLSA particles ranged from 0mM, 0.2mM, 1mM, 2mM. Absorbance intensity at 498nm using extinction coefficient ε= 81,000 $cm^{-1}M^{-1}$ was used to calculate the total and remaining concentration of Rho110.

Biotin-labeled RLLLSA Concentrates Strepavidin-GNP

To determine the general accessibility of the particle, a biotin group was attached to the N-terminus of RLLLSA. Strepavidin-functionalized gold nanoparticles can then be used to visualize the distribution or movement of the entities without having to use any negative stains, such as uranyl acetate. Biotin was coupled to uncapped the NH_2-RLLLSA sequence that was synthesized on a solid support using a standard FMOC solid-phase peptide coupling reaction with the carboxyl group on the tail of the biotin molecule (**Figure 6-4**).

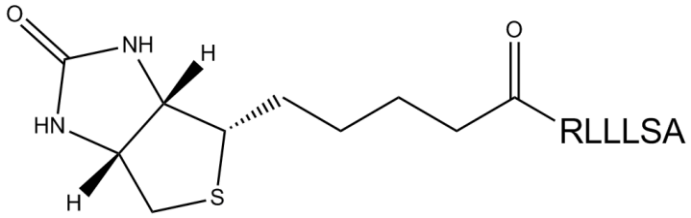

Figure 6-4. Structure of biotin-labeled RLLLSA.

If the particles are truly hollow, the gold nanoparticles should concentrate only near the edges of the particle where the concentration of biotin-functionalized peptide is concentrated. If the RLLLSA peptide is distributed throughout the particle, there should be a homogeneous distribution of nanoparticles in the core of the particle.

The biotin-RLLLSA peptide was purified and, as observed by TEM, forms particles of similar dimensions as wildtype Ac-RLLLSA under the same conditions (**Figure 6-5a**). Uniform 20nm Strepavidin-coated gold nanoparticles (**Figure 6-5b**) were then mixed with Ac-RLLLSA and biotin-RLLLSA. The Ac-RLLLSA particles

do not interact with the Strepavidin-coated gold nanoparticles (data not shown). The biotin-RLLLSA peptide particles can be observed by TEM without any negative stain added and appear very dark which correlates with very high electron-density due to the gold nanoparticles being highly concentrated in the core of the particles (**Figure 6-5c**). The lack of transmission through any portion of the particles suggests that the particles are not hollow and that the peptide is distributed throughout the core of the particle, consistent with the particles being able to sequester molecules away from the bulk solvent. When the particle is heated by the electron beam for 30 seconds, it appears to burst, spraying the nanoparticles out onto the grid (**Figure 6-5d**).

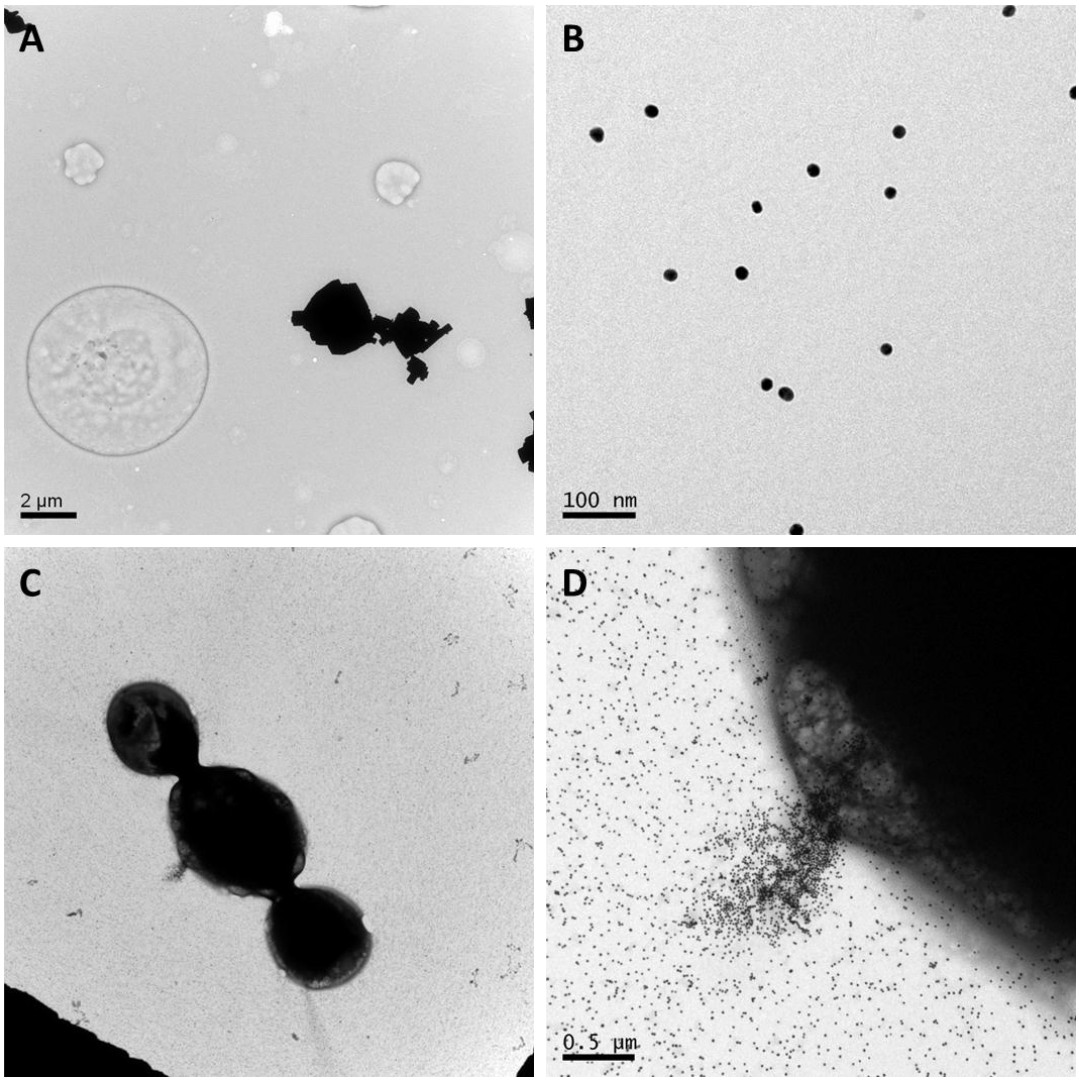

Figure 6-5. TEM of the Biotin-RLLLSA peptide particles (a), the Strepavidin-coated 20nm gold nanoparticles (b), the 1:1 mixture of Biotin-RLLLSA particles with Strepavidin-coated gold nanoparticles (c) showing high density within the particles and a close-up of the Biotin-RLLLSA particle (d) with nanoparticles after focusing the electron beam on the particle for 30 seconds. All samples were prepared without any negative stain.

RLLLSA Does Not Change the Morphology of Aβ(16-22) E22L

The data in Chapter 5 show that adding salt to the mixed Aβ(16-22)/RLLLSA tube structures results in their disassembly into particles and fibrils. To determine the importance of the electrostatic interactions in the formation of the mixed nanotubes, I chose to mix the RLLLSA peptide with both Aβ(16-22) E22L and RLVFFAL at a ratio that results in a significant size change of the tubes when mixed with Aβ(16-22). KLVFFAL, RLVFFAL and Aβ(16-22) were allowed to assemble into mature tube or fibril structures for 2 weeks (**Figure 6-6a, 6c, 6e**). RLLLSA particles were added to the mature structures and the samples were incubated for another 2 weeks. Under these conditions, both the KLVFFAL and RLVFFAL nanotubes remained the same dimensions as before and no morphological changes were observed over 2 weeks (**Figure 6-6b, 6d**). However, the Aβ(16-22) fibrils had already begun to form ribbon structures (**Figure 6-6f**).

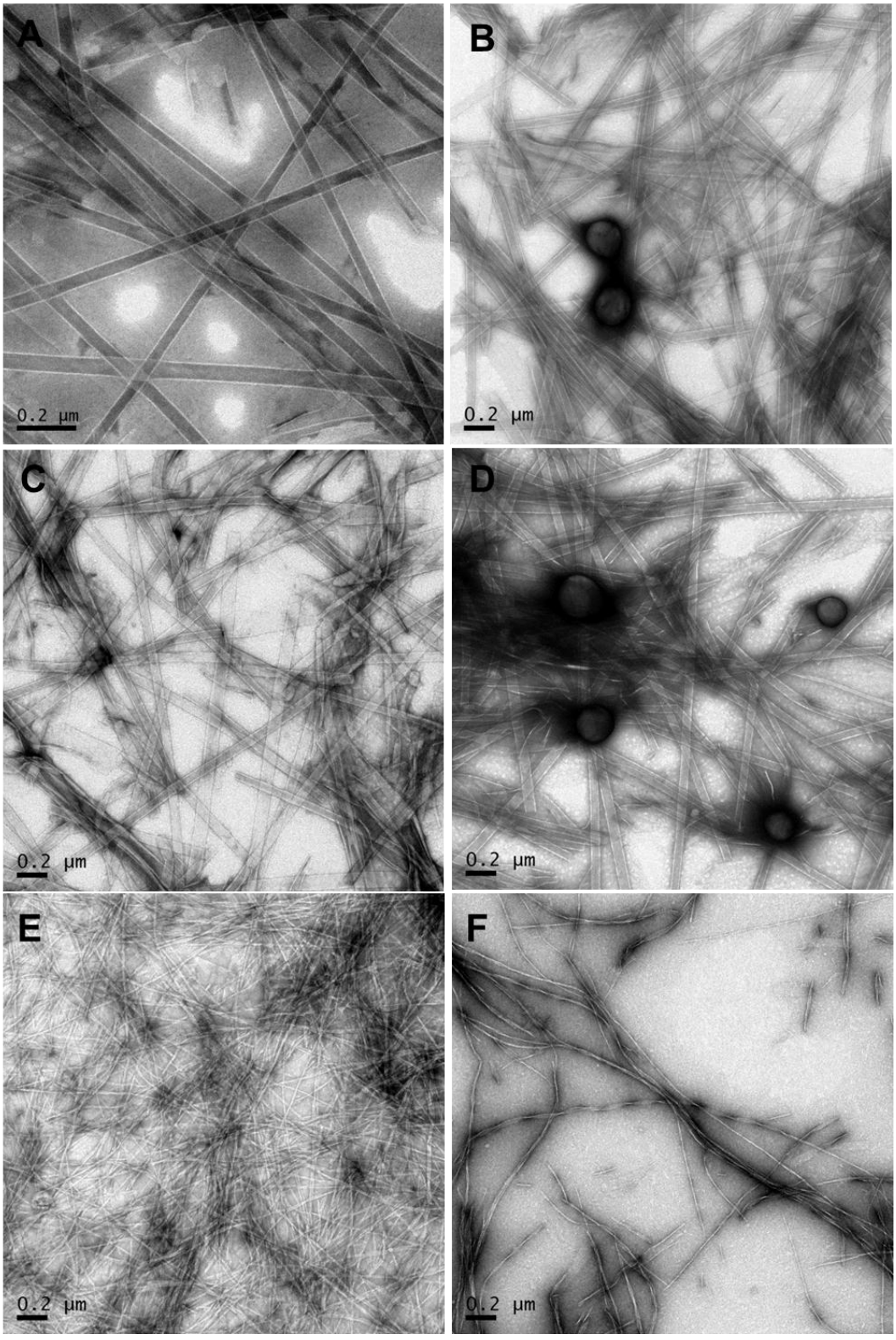

Figure 6-6. TEM of mature KLVFFAL nanotubes (a), KLVFFAL nanotubes mixed with 10% RLLLSA particles (b), mature RLVFFAL nanotubes (c), RLVFFAL

nanotubes mixed with 10% RLLLSA particles (d), mature KLVFFAE fibrils (e) and the KLVFFAE with 10% RLLLSA mixture forming ribbons (f). All samples were prepared at 2mM at neutral pH and incubated for 2 weeks after mixing.

To examine this possible interaction further, a Glu residue was added to the end of the RLLLSA sequence that may stabilize the interactions with Aβ(16-22) that lead to fibril formation. With RLLLSA being six amino-acids in length, addition of a complementary charge would make it seven residues long and would allow the RLLLSAE to pack against the KLVFFAE monomer with one more electrostatic interaction favoring the in-register packing that is characteristic of the Aβ(16-22) fibrils. The data in Chapter 4 show that the RLLLSAE sequence forms particles at lower concentrations and sheets at higher concentrations. Mixing mature RLLLSAE particles with Aβ(16-22) would result in only fibril formation due to the higher degree of complementarity between the two sequences. Mature RLLLSAE particles were mixed with mature Aβ(16-22) fibrils and over 14 days, the particles observed by TEM decrease, as expected. However, after another 12 days of incubation, I observed an increase of particles and then more fibrils 15 days later (**Figure 6-7**). This oscillation between morphologies was very unexpected, though the sample eventually stabilized with only fibrils visible after 45 days of incubation.

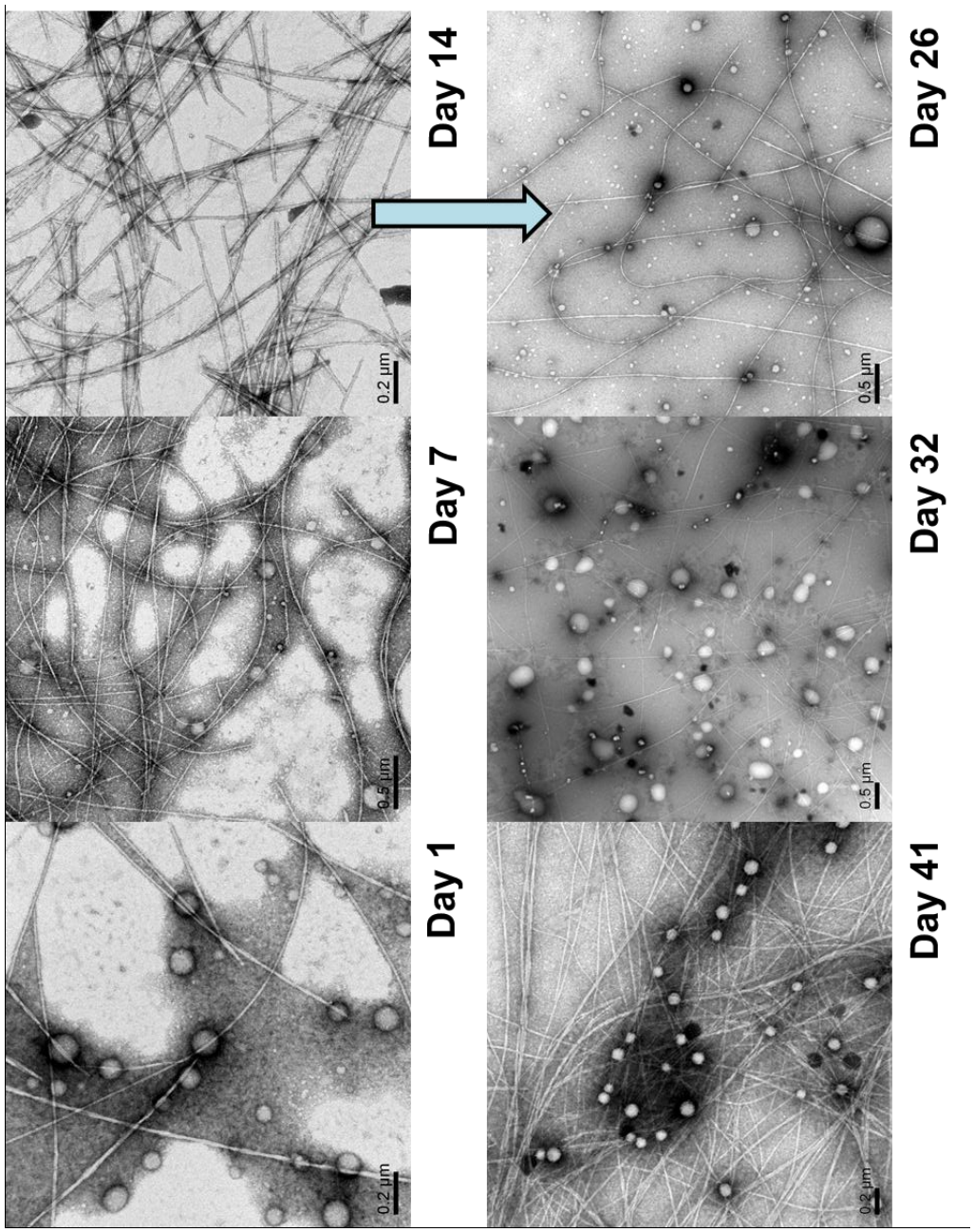

Figure 6-7. TEMs over time of the 2mM Aβ(16-22):2mM RLLLSAE mixture showing the general population increasing in fibrils at 14 days and then to particles at 26 days and then only fibrils are visible after 45 days at neutral pH.

The multiple morphologies observed over time in this mixed sample may be due to phase differences (crystalline versus non-crystalline) in the two peptides despite their sequence complementarity.

Post-Freeze TEM and Fluorescence Microscopy Suggest a Nucleation Event

Another interesting phase behavior was also manifested in experiments where the mixed tubes were frozen. At room temperature, the pure Aβ(16-22) nanotubes and those formed by mixing with RLLLSA typically exhibit very homogeneous negative staining with uranyl acetate throughout the hollow core by TEM (**Figure 6-8**) after assembly at room temperature. The tubes were frozen in an acetonitrile/dry ice bath (-40°C) and then thawed to test their stability. The stain applied to the Aβ(16-22):RLLLSA tubes post-freeze diffuses into only parts of the structures, suggesting that there are regions within the tube that are no longer completely hollow (**Figure 6-8**).

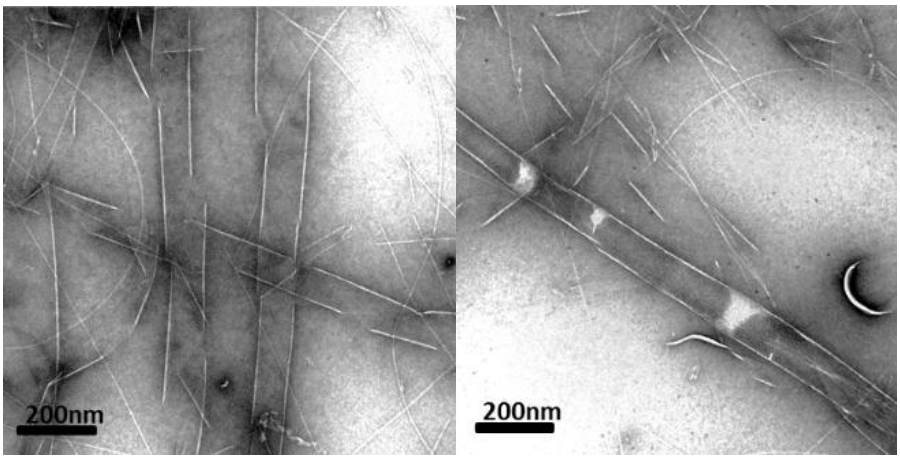

Figure 6-8. TEM micrographs peptide assemblies after being frozen at -40°C. (Left) pure Aβ(16-22) nanotubes formed at acidic pH. (Right) Mixed Aβ(16-22):RLLLSA (4:1) nanotubes at neutral pH.

These regions of blocked stain are not observed in the pure Aβ(16-22) tubes after being frozen, which means that the RLLLSA peptide may be partitioning within the mixed tubes due to differing phase properties upon freezing.

Based on the previous experiments, the particle-forming peptide, RLLLSA, should be able to sequester peptide monomer at its core and facilitate the arrangement of a new paracrystalline nucleus. Monomer addition onto this new template would lead to the creation of a new crystalline product, such as the nanotubes (**Figure 6-9**).

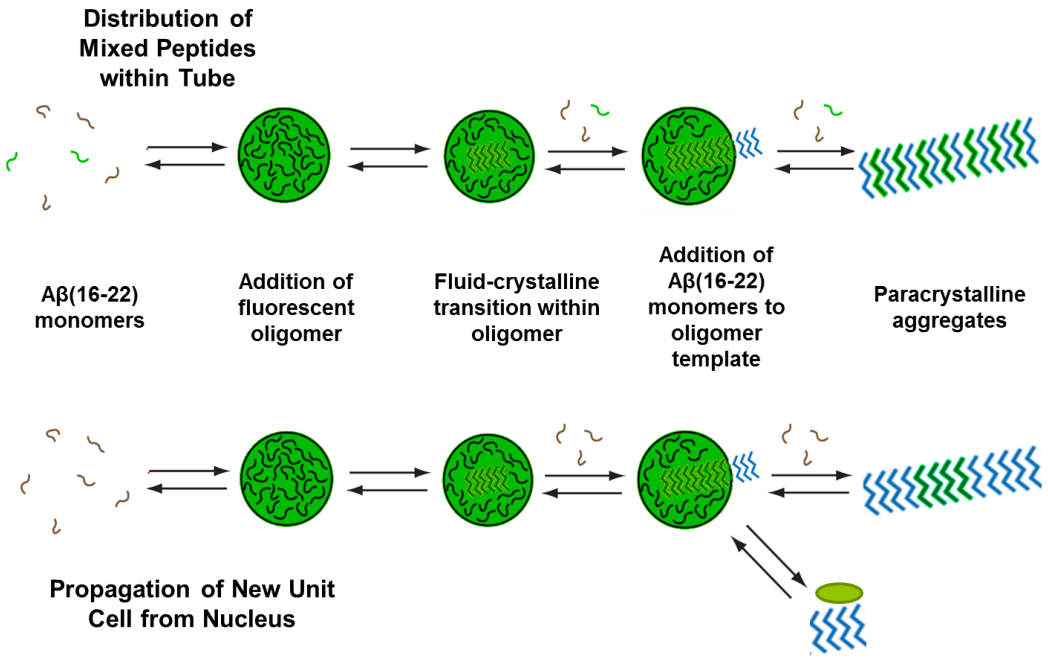

Figure 6-9. Models for possible distributions of Rho-RLLLSA fluorescence showing either a stoichiometric effect with even mixing, localization of Rho-RLLLSA within the structure or the Rho-RLLLSA particles leading to nanotube formation without being incorporated into the structure.

The RLLLSA within the particle could interact with the Aβ(16-22) to form tubes where the two peptides are evenly distributed throughout the structure or the RLLLSA could create localized pockets within the nanotube structure. A third possibility is that the RLLLSA particles sequester Aβ(16-22) monomer through electrostatic and hydrophobic interactions and the Aβ(16-22) forms nanotubes without RLLLSA being incorporated into the structure. To follow this phenomenon, a Rhodamine 110 dye molecule was covalently attached to the N-terminus of the

RLLLSA peptide following a similar synthesis protocol as for the covalent attachment of the biotin. The Rho-RLLLSA peptide forms particles, though they have slightly different properties as visible by TEM. They tend to be smaller in size and have depressions throughout the surface (**Figure 6-10**).

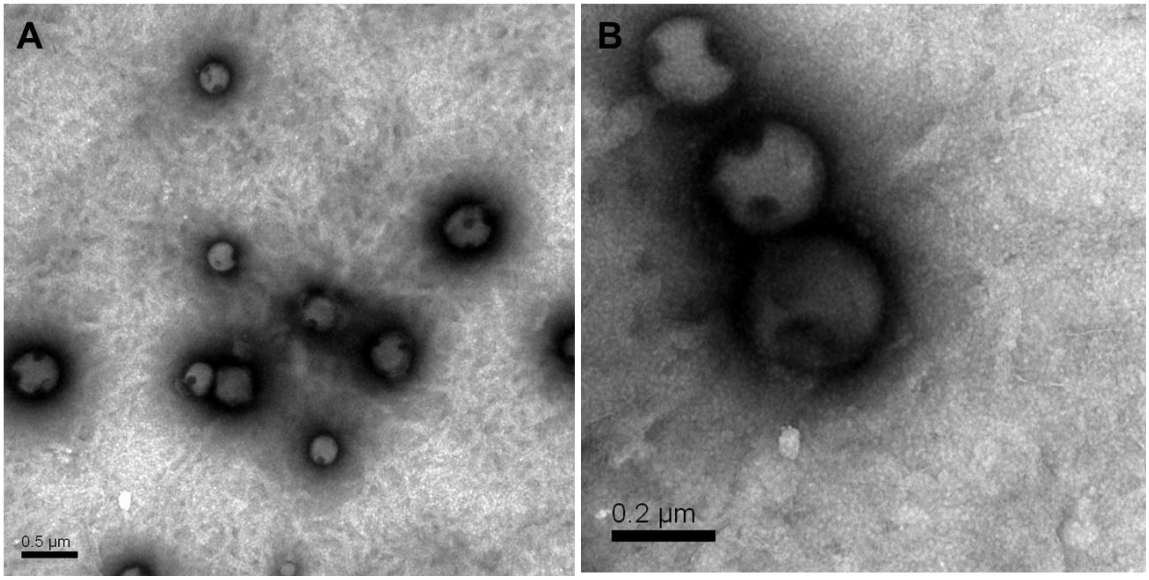

Figure 6-10. TEM of Rho-RLLLSA peptide particles after 2 weeks incubation at neutral pH (a) and a close-up of the particles (b) showing the depressions in the surface of the structure that collects the stain.

This may be due to the much larger size of the Rhodamine 110 moiety and the less-flexible ring system of the dye compared to the flexible tail of the biotin (**Figure 6-11**).

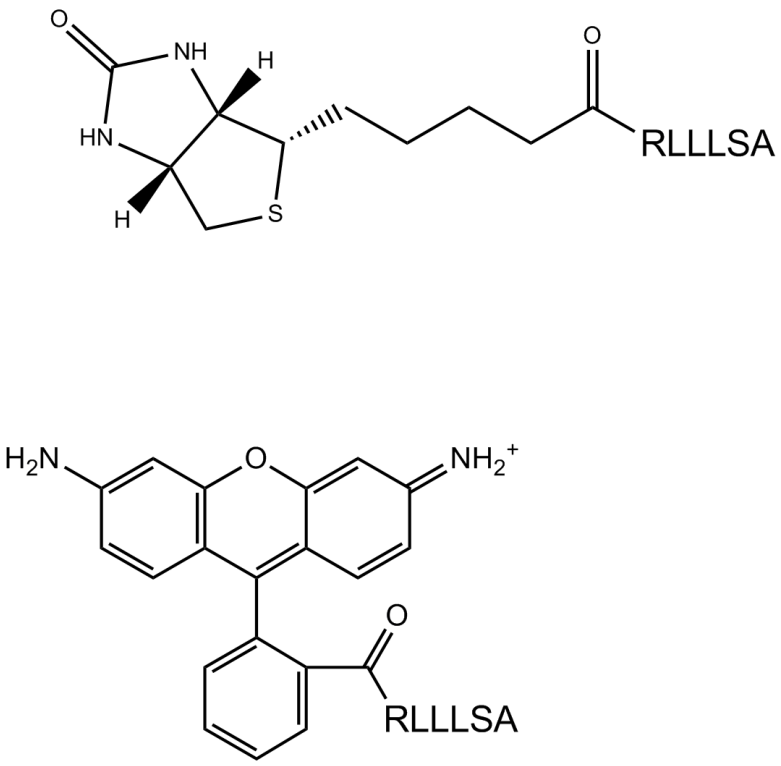

Figure 6-11. Structures of biotin-labeled RLLLSA (top) and Rhodamine 110-labeled RLLLSA (bottom).

Having a Rho110 attached to the peptide within the particles allowed them to be visualized using two-photon confocal fluorescence microscopy using a laser excitation of 780nm (comparable to 480nm single photon excitation) with emission detection at 520nm. By taking a slice at different positions off of the surface of the microscope slide, it was possible to construct a 3-d Z-stack image of the particles (**Figure 6-12**).

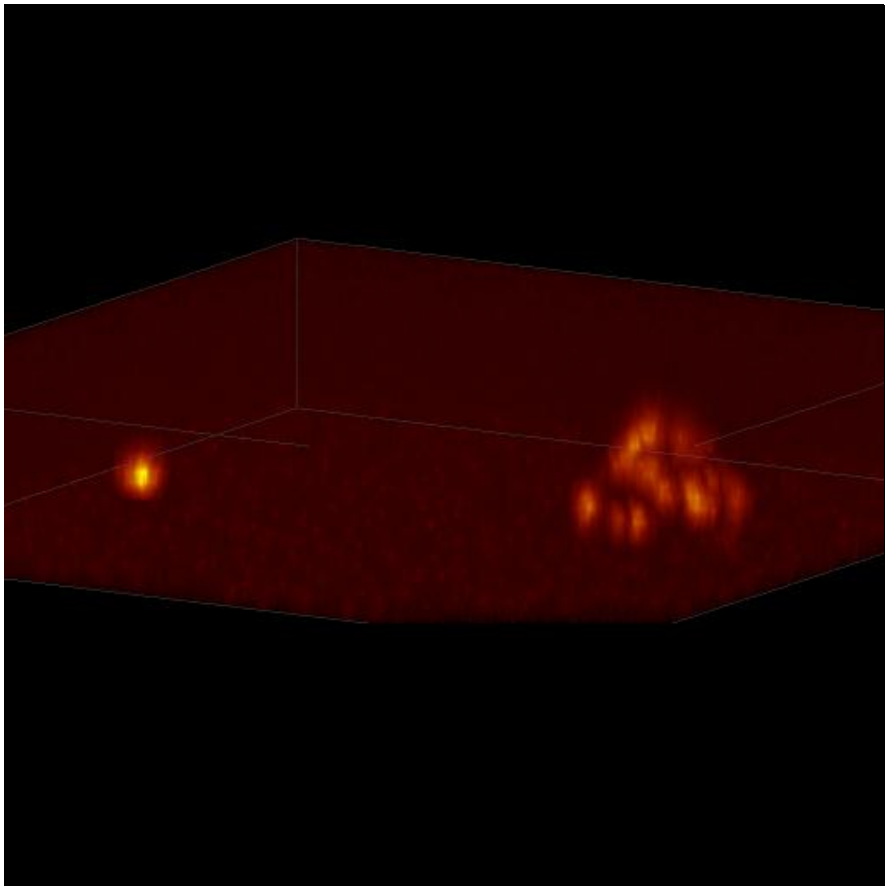

Figure 6-12. Two-photon fluorescence microscopy Z-stack of the Rho-RLLLSA particles showing their typical clustering, similar to that observed in TEM. Two-photon excitation was used at 780nm with detection of fluorescence at 520nm.

Particles assembled from the Rho-RLLLSA conjugate were added to Aβ(16-22) monomer using similar conditions as previous experiments. The samples were incubated for 4 weeks, until tubes were visible by TEM. The sample took longer time to form the nanotubes and the final products were more heterogeneous than previously observed, suggesting that the addition of the Rho dye affects not only the

particle morphology but also its ability to transform Aβ(16-22) into nanotubes (**Figure 6-13**), possibly due to the increase in charge.

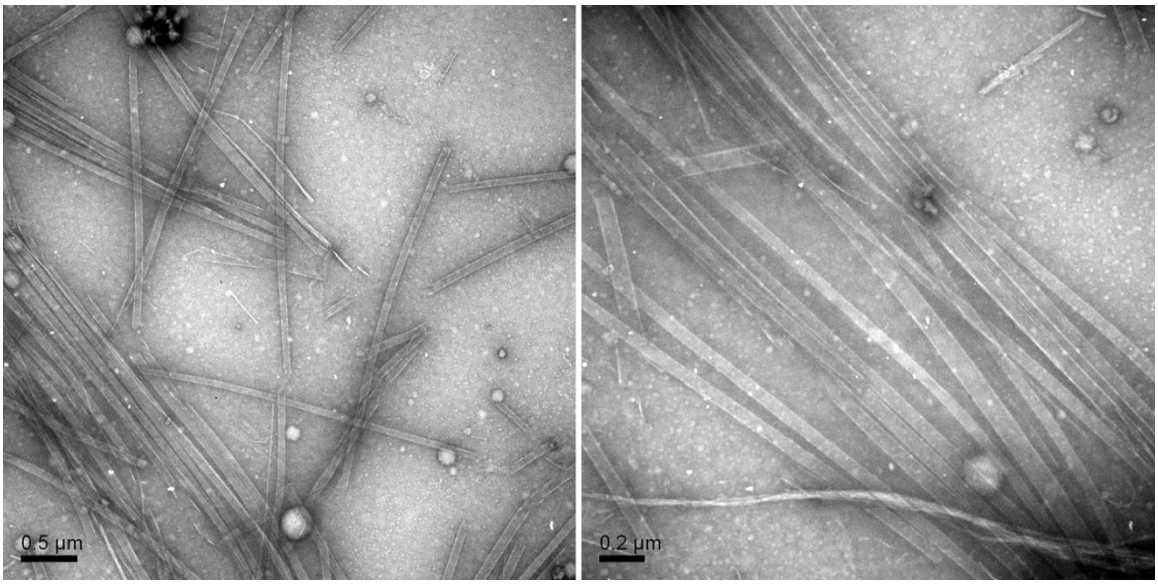

Figure 6-13. TEMs of the nanotubes formed by Rho-RLLLSA particles and Aβ(16-22) after 4 weeks incubation at neutral pH showing that the sample also contains particles and ribbons.

The tubes formed from Aβ(16-22) with Rho-RLLLSA also exhibited a lower melting temperature, showing that while the Rho-RLLLSA particle can still mediate nanotube formation, the final structures are not as thermostable as the mixtures formed using the wild type RLLLSA particles (**Figure 6-14**) or the greater heterogeneity of the sample contributes to broadening of the thermogram.

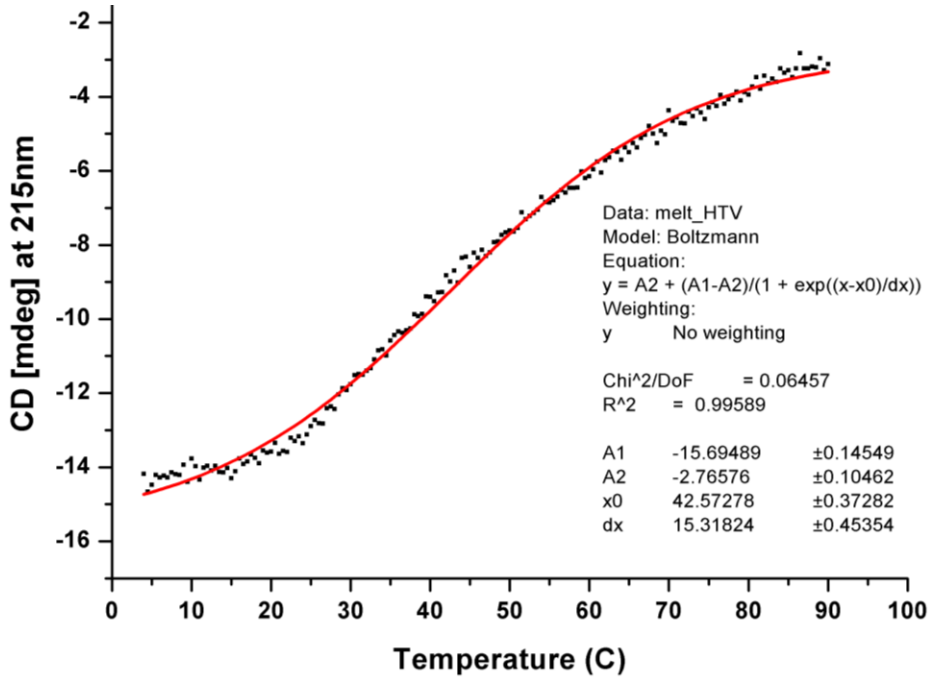

Figure 6-14. Melting of the Rho-RLLLSA/Aβ(16-22) mixed tubes showing the T_m shifting to 43°C versus the previously observed 64°C for the RLLLSA/Aβ(16-22) mixed tubes.

The addition of Alexa 555 dye, which binds to the tube surface non-covalently, allowed for independent sequential observation of the nanotubes, represented in red in the center panel of **Figure 6-15**, and the Rho-RLLLSA peptide, represented in green in the left panel of **Figure 6-15**. The separated two-photon absorption spectra of Alexa 555 and Rho-RLLSA allowed for selective excitation of each dye in turn. The red and green channel image overlap in **Figure 6-15** shows that punctate signals from the RLLLSA (green) are aligned with tubes (red), indicated in yellow.

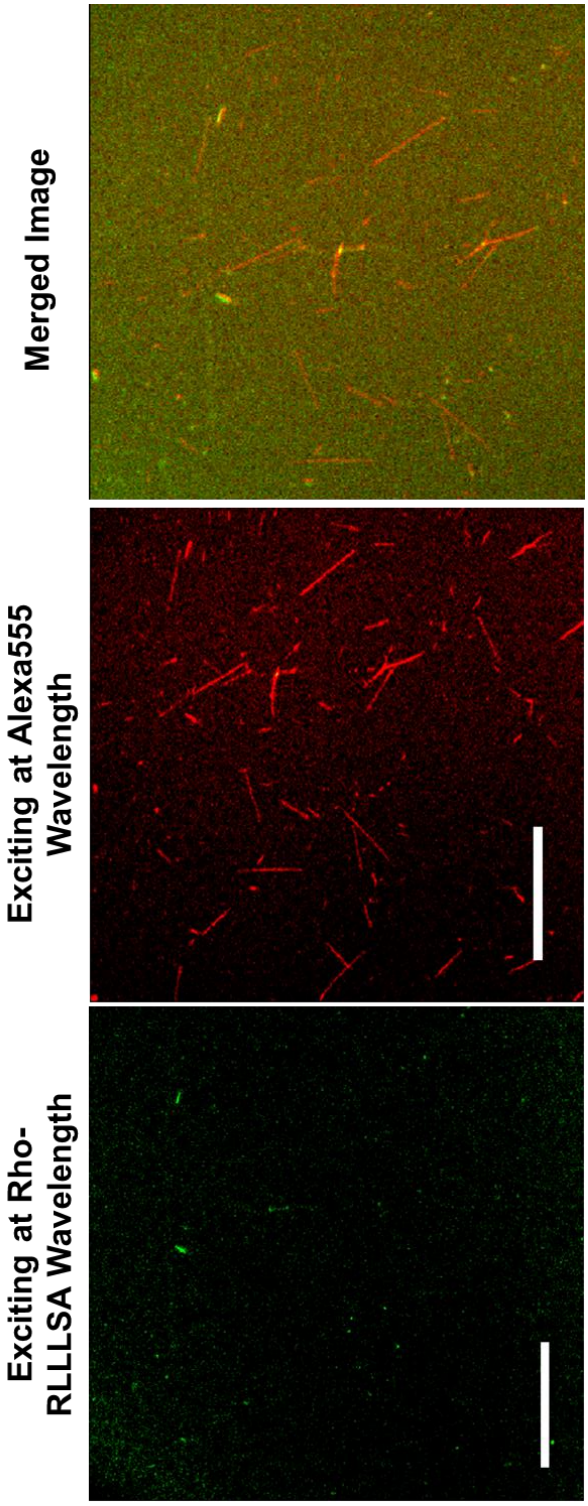
Merged Image
Exciting at Alexa555 Wavelength
Exciting at Rho-RLLLSA Wavelength

Figure 6-15. Fluorescence microscopy images of 500μM KLVFFAE with 250:1 Rho-RLLLSA (green) forming nanotubes. Exciting rhodamine at 480nm (left), Alexa555 (added to the tube sample for a final concentration of 1μM Alexa555) at 555nm (center) and the images merged (right) showing punctate Rho-RLLLSA signals (green) aligning with the nanotubes (red). Scale bar=20μM.

Localization of Rho-RLLLSA peptide within the self-assembled structure is consistent with a nucleation event leading to the templating of new structures. Though the fluorescence experiment confirms some association between the Rho-RLLLSA particles and the final nanotube structures, it is not clear whether the Rho-RLLLSA peptide is incorporated into the nanotube or merely associating with the surface of the tubes. Indeed, as shown in **Figure 6-16**, small Rho-RLLLSA particles appear to associate with the surface of the tubes.

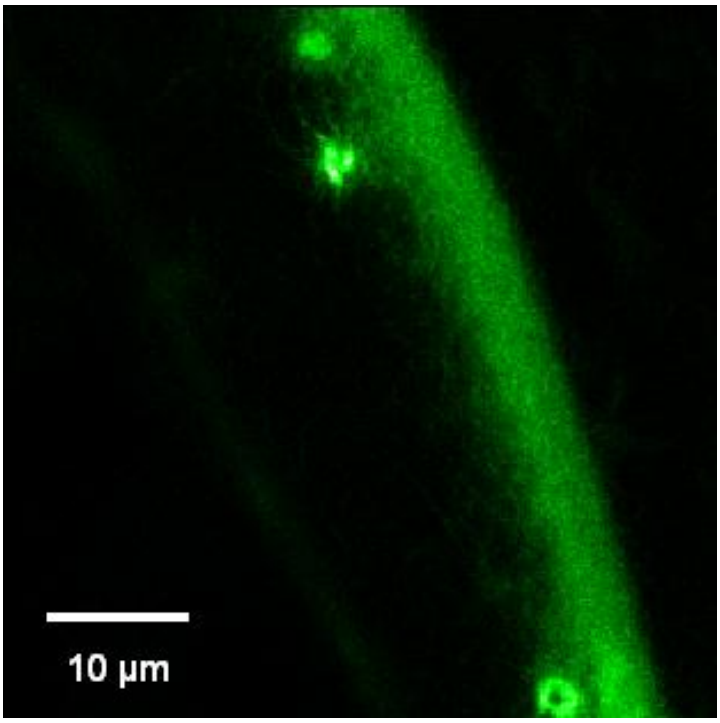

Figure 6-16. Fluorescence microscopy image of 500µM KLVFFAE with 250:1 Rho-RLLLSA (green) mixture leading to nanotubes showing Rho-RLLLSA highly concentrated on the surfaces of the nanotubes.

IE-FTIR Shows No RLLLSA Incorporation into the Mixed Nanotubes

To determine whether the RLLLSA peptide was being incorporated into the nanotube structure, KLV[1-^{13}C]FFAE, with a site-specific carbonyl ^{13}C was used for mixing. When a ^{13}C carbonyl is incorporated into a peptide, the FTIR signal of the peptide secondary structure is split with both ^{12}C and ^{13}C amide I stretches. The observed splitting is dependent on a tightly coupled the hydrogen-bonded oscillator network is and changes in the ^{12}C/^{13}C frequency splitting can be used to determine if another peptide is incorporated to dilute the oscillator network (Petty and Decatur

2005; Decatur 2006). A ^{13}C is incorporated at the F19 position of Aβ(16-22) gives two frequencies at 1637 cm^{-1} and 1599 cm^{-1}. As shown in **Figure 6-16**, unlabeled KLVFFAE (left) or RLLLSA peptide (right) were added to determine if either would significantly affect the frequencies of the ^{12}C and ^{13}C peaks. Unlabeled KLVFFAE peptide was incorporated into the hydrogen-bonding network with increasing amounts of KLVFFAE the 1624cm^{-1} stretch increases concomitant with a general broadening of the isotope splitting pattern at 1637cm^{-1} and 1599cm^{-1} (**Figure 6-17**). No significant change in the FTIR spectrum was observed with an increase of RLLLSA peptide, suggesting that the original oscillator network remained intact.

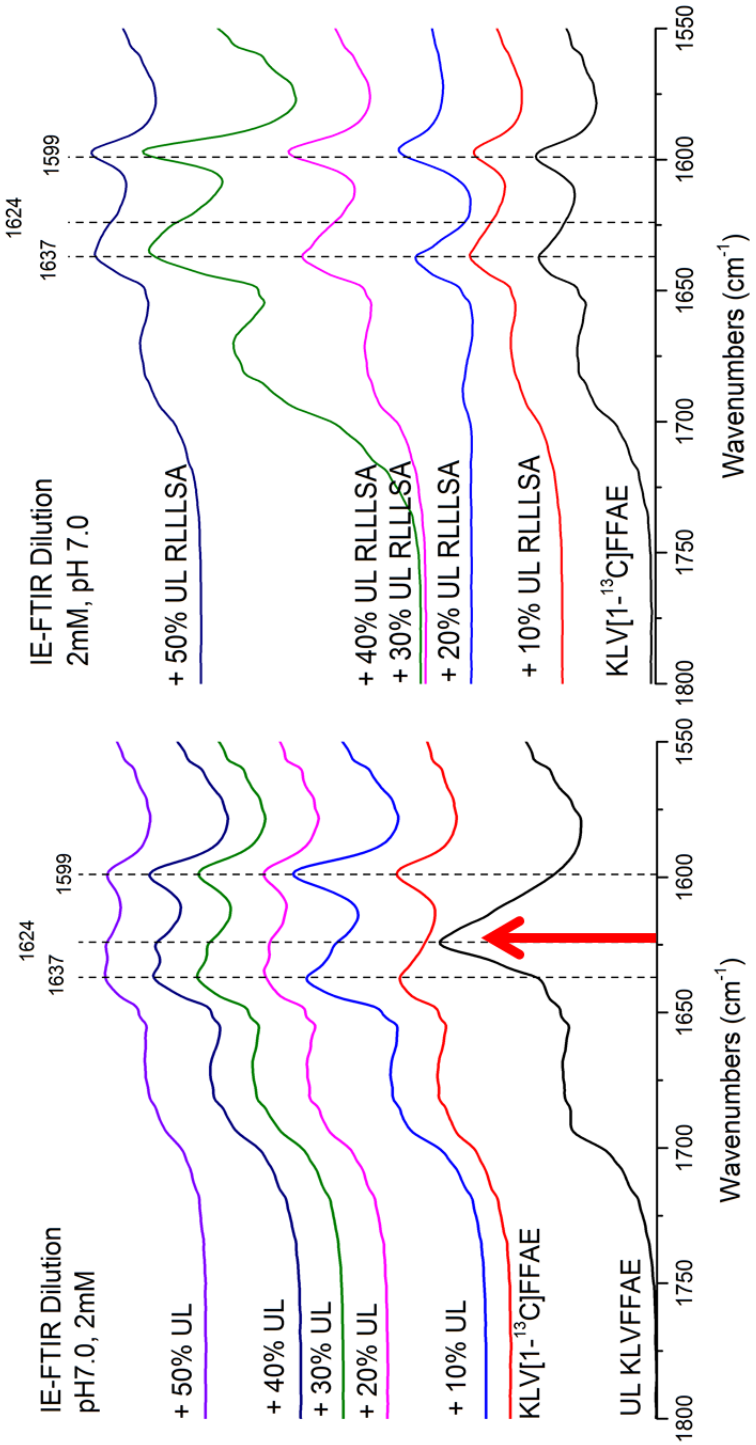

Figure 6-17. IE-FTIR spectra showing the mixture of KLV[1-^{13}C]FFAE with (left) unlabeled KLVFFAE and (right) unlabeled RLLLSA particles at different ratios. The

reappearance of the 1624cm^{-1} when mixing with unlabeled KLVFFAE shows that the oscillator network is being diluted by the incorporation of more ^{12}C peptide, whereas there is no change observed in the sample mixed with RLLLSA suggesting that the network has not been diluted with ^{12}C.

If RLLLSA is indeed not being incorporated into the nanotube structure but acting to desolvate the Aβ(16-22) monomer, then it follows that other particle-forming sequences, such as those described in Chapter 4, should also propagate the nanotube morphology upon mixing with Aβ(16-22). Sequences RLLLLSA (**Figure 6-18a**) and RLLLVA (**Figure 6-18d**) were allowed to assemble into particles and were then mixed with 1mM Aβ(16-22). After 2 weeks of incubation, ribbons and tubes were observable by TEM (**Figure 6-18b, 18c, 18e, 18f**) for both particle mixtures.

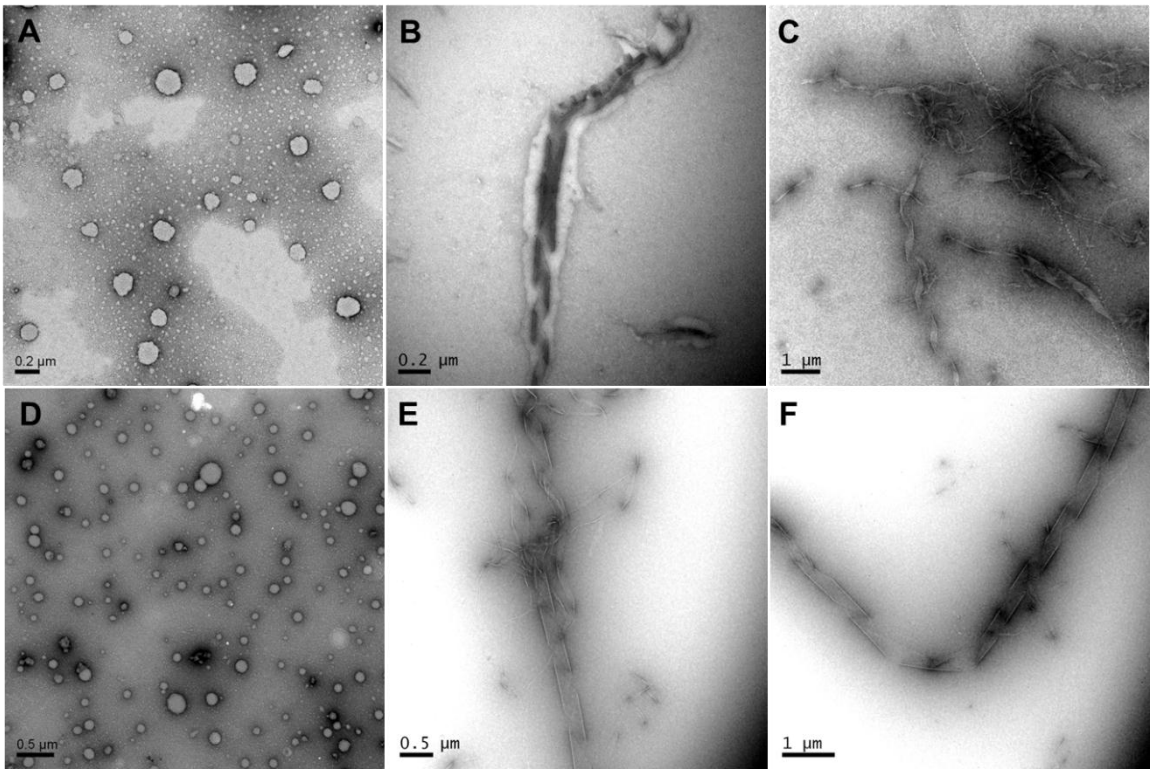

Figure 6-18. TEM of RLLLLSA (a) and RLLLVA (d) particles formed at 4mM at neutral pH and room temperature. After mixing with 1mM Aβ(16-22), both RLLLLSA (b,c) and RLLLVA(e,f) form nanotubes after incubation for 2 weeks.

Another sequence, RWLISA, taken from the WDR36 homology model, also forms particles under these conditions (**Figure 6-19a, 19b**). When mixed with Aβ(16-22), this sample also leads to nanotube formation (**Figure 6-19c, 19d, 19e, 19f**), though these are of larger diameters than those formed by mixing RLLLLSA and RLLLVA shown in **Figure 6-18**. The ability for all of the particle forming peptides to convert Aβ(16-22) into nanotubes supports that these particles serve as a unique microenvironment to desolvate the monomer and that their ability to facilitate

assembly of Aβ(16-22) into nanotubes is independent of sequence, so long as they form particles.

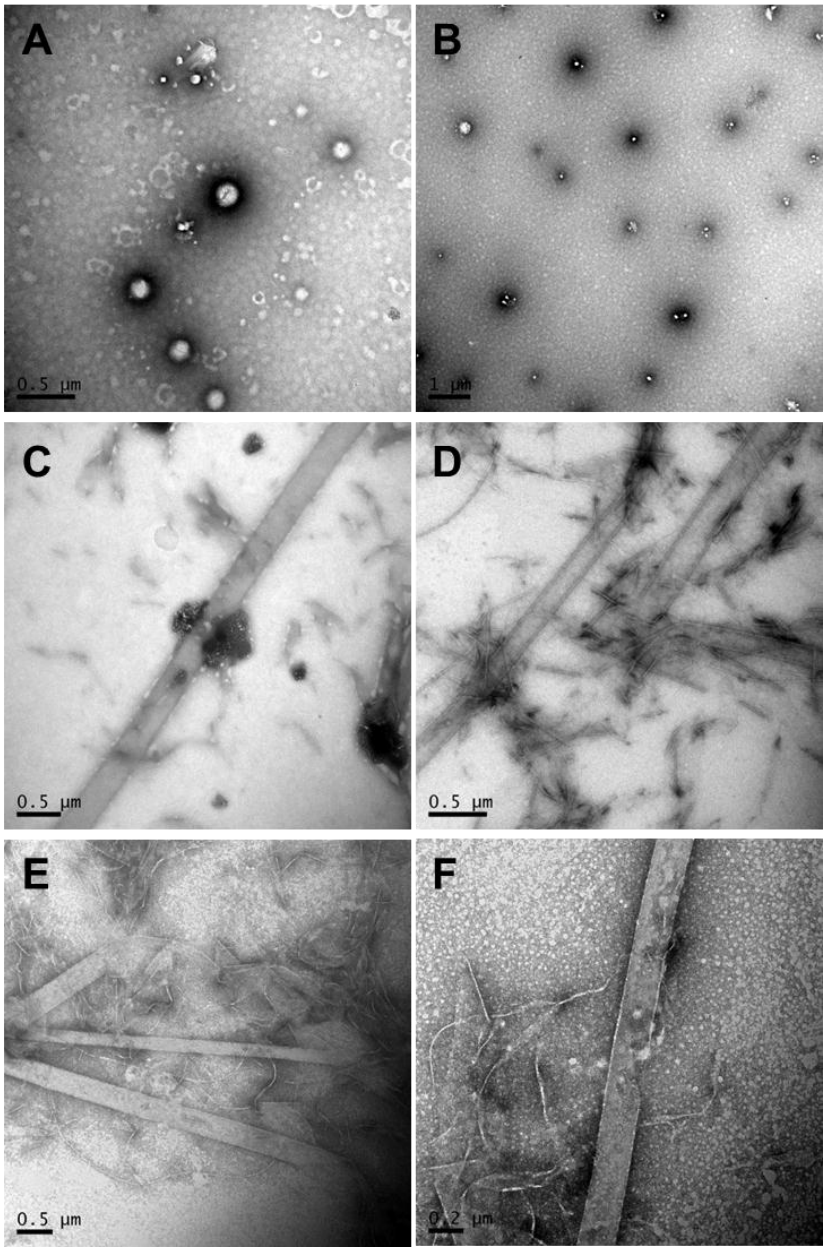

Figure 6-19. TEMs of 4mM RWLISA particles formed at neutral pH and room temperature(a and b) and a sample of 25% RWLISA particles mixed with 1mM Aβ(16-22) at neutral pH after 3 days (c and d) and 7 days (e and f).

Discussion

In Chapter 4, it was shown that the RLLLSA peptide forms particles and, in Chapter 5, these particles were shown to transform Aβ(16-22) into nanotubes under conditions where only fibers should form. Knowing that other sequences similar to RLLLSA in their amino acid composition can also form particles (RLLLLSA, RLLLAG, and RLLLVA), I mixed these with Aβ(16-22) monomer and also observe tube formation, which suggests that this is a general property of the sequence amphiphilicity. I propose that sequences sharing this charge-hydrophobic pattern should be able to form particles. Previously, it was demonstrated that removal of the Glu from KLVFFAE greatly retarded assembly, though it may have been that this peptide, KLVFFA, was assembling into small particles (Kun Lu, Thesis 2005) that were not able to be characterized using the standard methods for identifying amyloid. This sequence may also be able to modulate Aβ(16-22) assembly and deserves further investigation.

Based on my experiment with Rho110, it appears that the RLLLSA particles are able to sequester small molecules, and they may also be able to sequester other peptides to their core, though this pathway would need to be elucidated using a more sensitive method, such as fluorescence microscopy. While wild-type RLLLSA particles do not readily sequester gold nanoparticles, the biotin-labeled RLLLSA is able to create particles that can densely concentrate Strepavidin-labeled gold nanoparticles. The dense core observed by TEM in the unstained samples shows that

the particles are diffuse throughout the entire core of the particle, which suggests that they are likely not hollow, though this should be confirmed using freeze-fracture EM (cryo-etch EM). Interestingly, the biotin-RLLLSA particles have extensions between the large particles after addition of the nanoparticles (**Figure 6-5c**), similar to what is observed in the flash-frozen RLLLSA sample from Chapter 4 (**Figure 4-10**). These differences may be due to the nanoparticles changing the surface tension or the fluidity of the Biotin-RLLLSA particles, confirming their dynamic and responsive nature.

The data in Chapter 5 showed that the mixed tubes fell apart into ribbons and particles upon addition of salts, demonstrating potential electrostatic interactions being crucial to the nanotube formation and stability which is consistent with the peptides being antiparallel in-register. Here, I show that, while the addition of RLLLSA particles to Aβ(16-22) results in ribbon formation, addition of the RLLLSA particles to KLVFFAL or RLVFFAL nanotubes does not result in any significant morphological changes. At the ratio used for the mixture, I typically observe the formation of much larger tubes, which should be distinguishable from the wildtype tubes typically formed by KLVFFAL and RLVFFAL. However, since no change is observed in the sizes of the tubes and the particles are still visible on the grid, I conclude that the Glu residue is essential to promote the interactions that lead to mixed tube formation, though more work should be done to determine if the Glu is important for the tube formation or just for sequestering and concentrating monomer in the RLLLSA particle.

Among the RLLLSA sequence variants prepared in Chapter 4, RLLLSAE was the only one that could form sheets. Due to the addition of the Glu on the C-terminal end of the peptide, this sequence would be more likely to interact with Aβ(16-22) to form fibrils since the Glu would both extend the length of the peptide to seven residues, as well as position a complementary charge on the same face as the Arg residue, recapitulating the charge-hydrophobic-charge pattern of KLVFFAE. When RLLLSAE particles are mixed with Aβ(16-22), the morphology does transition over time from the mixture of particles and fibers, to fibers, to only particles and finally back to fibers. The transitions observed suggest that the peptides are able to sample more fluid conformations before "relaxing" into their most stable state. This is also interesting because the RLLLSA core may be more conformationally "flexible" than the KLVFFA core. This experiment shows that the mixture does not immediately crystallize to form fibers, but may transition several times, support that there are differences in RLLLSA and KLVFFA core sequences. The oscillation between fibers and particles also shows the plasticity of these mixed peptide structures and should be investigated in more detail.

When the mixed tubes are frozen, I observe sections within the tubes that exclude stain and are, presumably, no longer hollow. Though not shown conclusively in my experiments, these may be regions of greater structural heterogeneity that are more sensitive to temperature changes. To determine if the RLLLSA particles were the cause of these heterogeneous regions, a Rho110 dye was added to the end of the peptide. Oddly, while the addition of the biotin molecule to the RLLLSA sequence resulted in particles nearly identical to the wildtype RLLLSA

(**Figure 6-5a**), the Rho-RLLLSA peptide formed smaller particles with distinct pitting along their surface (**Figure 6-10**). This may be due to the differences in the size and rigidity between biotin, which has its moiety extended from the peptide on a longer alkyl chain, and Rhodamine 110, which has a large, bulky ring system very close to the body of the peptide. The ability of the Rho110 molecule to pack with itself may also cause non-native interactions as the particles form. When the Rho-RLLLSA is mixed with Aβ(16-22) monomer, I observe a heterogeneous mixture of nanotubes with some particles and small fibrils, which may also be a function of the Rho110 affecting the stability of the particles. The melting temperature of this mixture is depressed and could be due to the higher degree of heterogeneity in the sample.

Though the Rho-RLLLSA fluorescence correlated well with the spatial positions of the nanotubes as stained with Alexa555, this experiment did not conclusively demonstrate that the RLLLSA peptide was indeed incorporated into the tube structure. The associations of the two may have occurred after the tube formed, with the Rho-RLLLSA sticking to the surface of the tubes. By using IE-FTIR the degree of incorporation of an unlabeled ^{12}C peptide into a $^{12}C/^{13}C$ hydrogen-bonding network using a previously characterized peptide, KLV[1-^{13}C]FFAE, was determined (Kun Lu, Thesis 2005). This isotope-enriched peptide has a reproducible FTIR spectrum with significant splitting between the ^{12}C and ^{13}C frequencies due to the alignment of the F19 carbonyl position within the antiparallel, in-register β-sheet packing of the Aβ(16-22) fibers. I show that mixing unlabeled Aβ(16-22) into this peptide results in a significant change in the frequencies, consistent with the dilution

of the ^{13}C in the network due to the incorporation of more ^{12}C peptide into the β-sheets. While more structural characterization is necessary, the lack of change in the FTIR spectra upon mixing KLV[1-^{13}C]FFAE and RLLLSA demonstrates that the peptide is not being incorporated into the nanotube structure at concentrations above the detection limit for this technique. A more sensitive technique would be needed to determine if small amounts of RLLLSA are indeed becoming part of the structure.

The RLLLSA peptide particles appear to be acting as a passive agent for desolvation that allows Aβ(16-22) to access morphologies with more extended lamination, such as nanotubes. As shown in the CD melting experiment, the mixed tubes are not as thermostable as the pure Aβ(16-22) fibers formed in the absence of RLLLSA, suggesting that these tubes are a kinetic trap for Aβ(16-22) that is stable under these conditions. These experiments demonstrate that the morphology of Aβ(16-22) can be significantly altered without major rearrangements in the packing of its peptide core and that Aβ(16-22) can be affected by other peptide sequences while the final morphologies are primarily composed of the Aβ(16-22) sequence. This mechanism is very powerful in the context of disease, with amyloid β peptide being the major component of plaques. The conformations of the original amyloid nucleus may be greatly affected by surrounding proteins without them needing to be incorporated into the final structure.

Materials and Methods

All chemicals were purchased from Sigma-Aldrich (St. Louis, MO) unless stated otherwise.

Peptide Synthesis and Purification

All peptides used were synthesized using standard FMOC solid-phase peptide synthesis (SPPS) protocols with both N- and C-termini capped using microwave synthesis (CEM Liberty Peptide Synthesizer, North Carolina, USA). The peptides were cleaved from the solid support using a cleavage cocktail of TFA/anisole (95/5, v/v). The resulting solution was filtered from the resin and precipitated using excess chilled anhydrous ethyl ether. The centrifuged pellet was dried under house vacuum before purification. They were purified by reverse-phase HPLC (RP-HPLC) to greater than 99% and their mass was confirmed using TOF-MALDI mass spectrometry. Capped blade and hairpin sequences from the G-protein crystal structure (PDB: 1A0R) were synthesized using the same SPPS protocols and were purified and confirmed using previously described methods.

Synthesis of Rho-RLLLSA and Biotin-RLLLSA

Peptide was prepared on a solid support resin using FMOC microwave-assisted peptide synthesis with final deprotection of the FMOC, leaving a free –NH2 on the N-terminus of the peptide. The resin was washed with DCM before the coupling reaction. For coupling of Rhodamine 110, a 3x molar equivalent (assuming a 0.1mmol scale for peptide synthesis) of Rhodamine 110 was added to a minimal

volume of DCM and stirred to dissolve. To this solution was added 8 equivalents of DIPEA. After 10 minutes, 3 equivalents of HBTU was added to the Rhodamine solution for activation. After another 10 minutes, the resin slurry was added to this Rhodamine solution. Reaction was stirred overnight under N_2 gas in an ice bath and was monitored by TLC. Biotin coupling was performed by first dissolving biotin in a minimal volume of a 1:1 DMF-DMSO solution with gentle warming. To this was added 0.3mL DIPEA. After 5 minutes, 2.1mL of 0.45M HBTU/HOBt was added to the biotin solution for activation. After 5 minutes the peptide resin slurry was added to this biotin solution. The reaction was stirred overnight under N_2 gas in an ice bath and was monitored by TLC. Following either reaction, the resin was washed with 1:1 DMF:DMSO (2x), DMF (2x) and DCM (2x) to remove excess Rhodamine 110 or biotin from the resin. Resins were then dried and the peptides cleaved as previously described.

Peptide Assembly Conditions

For assembly, the peptides were dissolved in 40% acetonitrile/60% water to a final concentration of 1.0 mM unless otherwise stated. pH was adjusted to near pH 7.0 using pH paper and the solutions were allowed to mature at room temperature for the indicated time periods. To rapidly dissolve the peptide, the suspension was vortexed at high speed for 30s and sonicated at 40kHz in a room temperature water bath for 1-2min. This process was repeated 3-4 times till the solution was clear, generally requiring less than 20 min to ensure complete dissolution.

Peptide Mixing

For a monomer pool, the purified peptide was dissolved in HFIP to disrupt any preformed nuclei and then the solvent was evaporated using N_2 gas. The peptide monomer was resuspended at a concentration of 1mM in a 40% acetonitrile/60% water solution that was then adjusted to pH 7.0 using 500μM NaOH. Mature assemblies were sonicated for 20 minutes and then the molar percentage indicated of each was added to the resuspended Aβ(16-22) monomer. The solutions were incubated at room temperature for a minimum of 2 weeks and assembly progress was monitored by TEM and CD signatures at 200nm and 215nm.

Rhodamine 110 Spin-Down Experiment

A stock solution of 500μM Rhodamine 110 was prepared in 40% acetonitrile/60% water at neutral pH. From this, aliquots of Rho110 were prepared at 20μM and the peptide concentrations for KLVFFAL tubes and RLLLSA particles was arrayed from 0mM, 0.2mM, 1mM, 2mM using stock solutions originally at 4mM. The mixtures were incubated for 30 minutes before being centrifuged at 13k rpm for 30 minutes. Intensity of the absorbance peak at 498nm was used to calculate the total and remaining concentration of Rho110 using extinction coefficient ε= 81,000 $cm^{-1}M^{-1}$.

Transmission Electron Microscopy

Samples were allowed to adsorb on a TEM grid (carbon/copper) for at least 1 min. Excess peptide solution was wicked away with filter paper. A 2-wt % uranyl acetate

solution was added to TEM grids and incubated for 3-5 minutes before wicking away. Samples were then placed in a desiccator overnight. TEM micrographs were recorded with a Hitachi 7500 TEM at magnifications ranging from 2000x to 200,000x with a Tungsten filament at an accelerating voltage of 75 kV.

Concentration of Strepavidin-Gold Nanoparticle Conjugate

A 5mM stock solution of Strepavidin-conjugated gold nanoparticles was purchased and contained 50 mM potassium phosphate, 75 mM NaCl buffer, pH 7.4 with 20% glycerol. To remove some of the salts, the stock solution was centrifuged for 20 minutes and resuspended in the same volume of filtered ddH_2O. 1mL of this was diluted to give a working concentration of about 2.5mM gold nanoparticles. Biotin-RLLLSA particles were allowed to incubate at 2.5mM for 1 week before mixing 1:1 with the gold nanoparticle solution.

Two-Photon Excitation Fluorescence Microscopy

Two-photon fluorescence images were acquired on a previously described home built two photon microscope.S3 All images were acquired with 780 nm excitation and detected using photomultiplier tubes (H7421) from Hamamatsu. For FCS measurements, the fluorescence signals were detected using an avalanche photodiode (APD) (EG&G, Vaudreuil, Canada). Sample positioning was controlled using a motorized stage ASI MS200 (Applied Scientific Instrumentation, S4 Eugene, Oregon). Samples were mounted either within an eight-well chambered cover glass (Naglenunc International, Rochester, New York) or on glass slides with 22×30mm

cover slips (Corning Life Science). Dual-color imaging under 780nm two-photon excitation used a 570nm dichroic mirror and bandpass emission filters of 530/50 and 645/75 to separate the Rh17-22 and Alexa555 signals. FCS measurements were performed both shortly after the samples were mixed and during maturation. Generally about 20min was required for sample preparation (vortex and sonication cycles) and to prepare the slides for imaging. For samples below the critical concentration, only monomeric peptide could be detected in solution and we did not attempt to further define the precise timing post-mixing. For samples in which the peptide concentrations exceeded the critical concentration, aggregates are already present at the earliest time points, approximately 20 min after mixing, and these aggregates were present throughout the first 24hr post mixing. The time scale over which the soluble aggregates turn into mature amyloid ranged from a few days to a month, depending on the original peptide concentration. Any sample that shows no evidence for assembly after one month is classified as unable to assemble.

Isotope-Edited FTIR

Isotope-Edited Fourier Transform Infrared (IE-FTIR) spectroscopy was used to confirm peptide incorporation. A solution of mature KLV[1-^{13}C]FFAE fiber assemblies was mixed at the indicated ratio with either unlabeled KLVFFAE or unlabeled RLLLSA peptide particles after each had been sonicated for 10 minutes. The mixtures were allowed to incubate for at least 3 weeks until the appearance of nanotubes was observed in the RLLLSA mixture by TEM. Sample aliquots (300μL) were centrifuged for 30 minutes at 13,000 rpm and frozen in a bath of dry ice and

acetonitrile bath (-40°C) for 20 minutes before lyophilizing overnight. The IR spectra were acquired using a Jasco FT-IR 4100 ATR with a diamond crystal at room temperature and averaging 256 scans with $4cm^{-1}$ resolution. Background spectra were acquired immediately before each sample and were subtracted from each sample spectrum. Data was imported into OriginPro for graphing and analysis.

Chapter 7

Conclusions

Peptide Sequence and Conformation

Though the amino acids that make up proteins are relatively simple molecular entities, their arrangement within a sequence gives rise to much greater complexity and the prediction of the characteristics of a peptide or protein simply by using its sequence is a challenge that has interested bioengineers and biochemists for years. Many computational methods have been developed to assist in these predictions and have gotten more accurate(McGuffin, Bryson et al. 2000; Al-Lazikani, Jung et al. 2001; Rohl, Strauss et al. 2004; Söding, Biegert et al. 2005), though the discovery of proteins with completely divergent sequences that still maintain the same secondary and tertiary folds demonstrates how much there is still to learn about the sequence-structure relationship (Chung and Subbiah 1996; Friedberg and Margalit 2002; Jordan, Kondrashov et al. 2005). Protein folds that are modular with repeating units, such as the β-propeller, can be used to discern the properties of sequences and their roles in the context of the full protein fold. In Chapter 4, individual sequences of the GPBS are shown to have distinct morphologies when removed from the context of the rest of the protein fold and the variety of these from different strand positions suggest that protein folding of even modular units may be more complex than previously thought. Hence, peptide sequences exist as an intricate balance of the properties of their sequences within context of the whole, which is more than simply the sum of the parts. It would be interesting to know if the patterns observed in the

aggregation propensities of the individual strands of the GPBS β-propeller, as discussed in Chapter 2, are also present in other β-sheet rich folds, such as β-barrels or β-sandwiches.

β-Propeller Folds: Platforms for Peptide-Peptide Interactions

The β-propeller fold is a key component of many cellular signaling pathways and serves as a platform for interactions between multiple protein subunits (Fülöp 1999). The ability of this fold to both dock with other proteins and maintain flexibility in order to transduce a signal to its opposite face is a critical adaptation for cellular communication in tissues (Adams, Kelso et al. 2000; Marinissen and Gutkind 2001; van Nocker 2003). Recently, G Protein Coupled Receptors, which have a β-propeller component, have been shown to play a role in many diseases and are currently one of the largest drug targets in pharmaceutical research (Klabunde and Hessler 2002; Dorsam and Gutkind 2007; Lagerstrom and Schioth 2008; Jorgensen, Peng et al. 2009). The data in Chapters 3 and 4 show that some GPBS propeller segments have a propensity for aggregation into amyloid and dynamic particles. Data within Chapter 3 suggests that the addition of the D strand significantly slows the rate of assembly, but it will also be determine whether this is specific to the D strand sequence or if other sequences have a similar effect. The aggregation of the strands from the GPBS described in Chapter 4 correlate well to the predicted aggregation propensities determined in Chapter 2. These properties have not been previously described in the context of signal transduction or protein

conformational flexibility, but these experiments offer evidence as to why the folding of these proteins is often chaperone-mediated and why the folding landscape of the protein may be significantly altered by either mutations or off-target interactions with other proteins.

Learning the Rules of Self-Assembly

Though the focus of this work has largely been disease-oriented, the lessons learned here will be useful for understanding protein engineering as well as bio-inspired materials. It is known that some self-assembling systems that contain reactive side chains are able to catalyze reactions (Tolu Omosun, unpublished results) and the assembled systems described in Chapters 3 and 4 may also have catalytic properties that differ depending on their peptide packing. The mixed nanotubes described in Chapters 5 and 6 would have a very different surface than the other nanotubes previously characterized as they are the only example of nanotubes having an antiparallel in-register peptide arrangement. Also, the ability to control the dimensions of these nanotubes simply by altering their mixing ratio is very powerful, and these structures could be used as scaffolds for attachment of photosensitive molecules in light-harvesting materials or as biologically-derived responsive materials for use in tissue engineering applications. Here I have described a simple, two-component self-assembling peptide system that is malleable at the molecular level and that could be further functionalized with the scaffold assembling in a predictable and reproducible manner.

The Shallow Energy Landscape for Amyloid Assembly

It has been proposed by Dobson and coworkers that all proteins can form amyloid given the right conditions (Chiti and Dobson 2009). In this thesis, I show that, while some sequences from the GPBS β-propeller fold readily assemble into amyloid, others aggregate into non-crystalline morphologies that persist for significant lengths of time even though they are not as thermostable as the amyloid fibrils. These morphologies may represent possible intermediates on pathway to forming amyloid or they may be aggregates that can mediate assembly of off-pathway structures. Chapter 5 presents evidence that the B strand of blade one of the GPBS, RLLLSA, can mediate a significant change in the morphology of Aβ(16-22), forming nanotubes under conditions where only fibers form. Multiple sequence variants of RLLLSA also self-assemble into particles, including RLLLSAE, which forms sheets at slightly higher concentrations. In these initial experiments, the characteristics important for forming and maintaining the dynamic particle morphology are not clear and future work should be done to understand mutations or environmental conditions that contribute to this interesting structure.

In the context of disease, self-nucleation is believed to be the major mechanism of amyloid deposition, wherein the most influential molecular entity for the templating of amyloid β monomer is another amyloid β sequence (Glabe 2001; Meyer-Luehmann, Coomaraswamy et al. 2006; Eisele, Obermüller et al. 2010; Langer, Eisele et al. 2011). This proposition is in contrast to the data presented in Chapters 5 and 6. Aβ(16-22), the central nucleating core of amyloid β, is clearly sensitive to the addition of exogenous peptide sequences, and in this case, those that

form particles. Chapter 6 summarizes that evidence for the RLLLSA particles sequestering small molecules within a dynamic interior, suggesting that Aβ(16-22) forms nanotubes within the unique particle environment. This first example of the Aβ(16-22) peptide forming antiparallel in-register nanotubes argues for the access to kinetic assembly products that remain trapped in their aqueous environment. It is also significant that the RLLLSA particles do not appear to interact with Aβ(16-22) E22L or RLVFFAL nanotubes—future work should determine if the RLLLSA particles may more readily interact with the monomers of these two peptides.

It is remarkable that the RLLLSA particles are able to convert the mature Aβ(16-22) fibrils into a stable, presumably kinetically trapped morphology. The fiber should be the most thermodynamically stable product within this mixture, which may mean that this may be a new thermodynamic product. I determined that the mixed tubes were a kinetic product based on the depressed melting temperature (63.8±0.3°C) when compared to the fibers (83.8±0.2°C), but the melting of the tubes may be altered by the solvation of the hollow region within the structure or the rate of the melt may have been slow enough to allow for re-equilibration of the sample, resulting in a population of structures. Regardless, in this simple, two peptide mixture we observe a transition from a fiber, which has a unique surface due to the peptide packing, to a much larger tube that has a different surface. The packing of the Aβ(16-22) core did not appear to change despite the macromolecular structure appearing different than a fiber, suggesting that Aβ(16-22)'s morphology can be modulated significantly without necessarily needing to incorporate the templating species. These two polymorphs of Aβ(16-22) could certainly have varying

interactions with their environments, and consequently these peptide mixing experiments highlight the importance of characterizing not only the physiological environment of amyloid assembly, but also the assembly context (i.e. what protein surfaces are able to interact with Aβ(16-22).

In my first generation model of β-propeller template amyloid nucleation, I proposed that the mutations within the blade could result in the exposure of internal β-strands that could serve as a preorganized template for the nucleation of Aβ(16-22) (**Figure 7-1**).

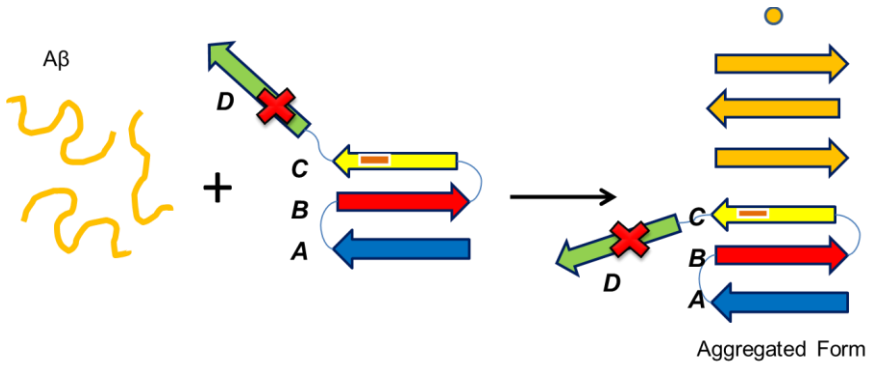

Figure 7-1. First generation model discussed in Chapter 4 showing that the blade of the β-propeller may serve as a preorganized template for the nucleation of Aβ(16-22) monomer.

However, based on the mixing experiments shown in Chapter 5, the sequences capable of self-assembling into crystalline morphologies were not able to template Aβ(16-22) as I had predicted. More interestingly, the non-crystalline, more conformationally dynamic B strand RLLLSA was able to not only nucleate Aβ(16-

22), but also result in a changed morphology. This result shows that a preorganized template is not necessary for Aβ nucleation and that desolvation of the peptide may be all that is required for it to organize into a nucleus capable of propagation. In the context of the fully-folded protein, this may mean that a mutation that leads to the local blade region unfolding into a more conformationally-flexible state may be able to act as a hydrophobic patch to desolvate amyloid β monomer and allow it to propagate (**Figure 7-2**).

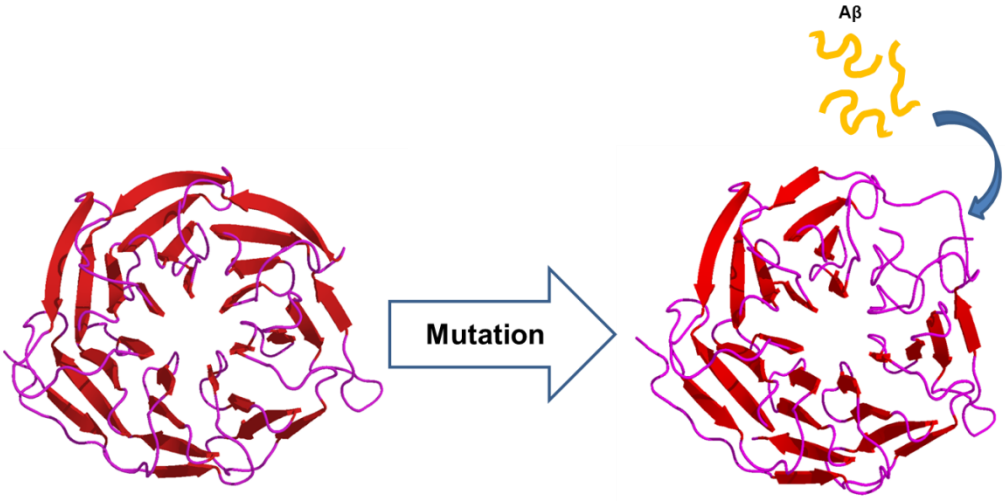

Figure 7-2. New mechanism of β-propeller mediated amyloid β nucleation wherein mutations within the β-propeller may create a hydrophobic, conformationally-flexible region on the surface of the protein where Aβ can desolvate.

In the context of diseases such as Alzheimer's and glaucoma, this simple mechanism to alter morphological heterogeneity may well be the source for a self-propagating form with great etiological significance. Future work should be done to characterize the surfaces of these kinetically trapped structures as well as to

understand if these are able to nucleate generations of structures, either similar to the parents or possibly new morphologies not yet observed.

Appendix I

FASTA Sequence of Myocilin, MYOC:

>sp|Q99972|MYOC_HUMAN Myocilin OS=Homo sapiens GN=MYOC PE=1 SV=2
MRFFCARCCSFGPEMPAVQLLLLACLVWDVGARTAQLRKANDQSGRCQY
TFSVASPNESSCPEQSQAMSVIHNLQRDSSTQRLDLEATKARLSSLESLLHQ
LTLDQAARPQETQEGLQRELGTLRRERDQLETQTRELETAYSNLLRDKSV
LEEEKKRLRQENENLARRLESSSQEVARLRRGQCPQTRDTARAVPPGSREV
STWNLDTLAFQELKSELTEVPASRILKESPSGYLRSGEGDTGCGELVWVGE
PLTLRTAETITGKYGVWWMRDPKPTYPYTQETTWRIDTVGTDVRQVFEYDL
ISQFMQGYPSKVHILPRPLESTGAVVYSGSLYFQGAESRTVIRYELNTETVK
AEKEIPGAGYHGQFPYSWGGYTDIDLAVDEAGLWVIYSTDEAKGAIVLSK
LNPENLELEQTWETNIRKQSVANAFIICGTLYTVSSYTSADATVNFAYDTG
TGISKTLTIPFKNRYKYSSMIDYNPLEKKLFAWDNLNMVTYDIKLSKM

FASTA Sequence of Optineurin, OPTN:

>sp|Q96CV9|OPTN_HUMAN Optineurin OS=Homo sapiens GN=OPTN PE=1 SV=2
MSHQPLSCLTEKEDSPSESTGNGPPHLAHPNLDTFTPEELLQQMKELLTEN
HQLKEAMKLNNQAMKGRFEELSAWTEKQKEERQFFEIQSKEAKERLMAL
SHENEKLKEELGKLKGKSERSSEDPTDDSRLPRAEAEQEKDQLRTQVVRL
QAEKADLLGIVSELQLKLNSSGSSEDSFVEIRMAEGEAEGSVKEIKHSPGPT
RTVSTGTALSKYRSRSADGAKNYFEHEELTVSQLLLCLREGNQKVERLEVA
LKEAKERVSDFEKKTSNRSEIETQTEGSTEKENDEEKGPETVGSEVEALNL
QVTSLFKELQEAHTKLSKAELMKKRLQEKCQALERKNSAIPSELNEKQELV
YTNKKLELQVESMLSEIKMEQAKTEDEKSKLTVLQMTHNKLLQEHNNAL
KTIEELTRKESEKVDRAVLKELSEKLELAEKALASKQLQMDEMKQTIAKQE
EDLETMTILRAQMEVYCSDFHAERAAREKIHEEKEQLALQLAVLLKENDA
FEDGGRQSLMEMQSRHGARTSDSDQQAYLVQRGAEDRDWRQQRNIPIHS
CPKCGEVLPDIDTLQIHVMDCII

FASTA Sequence of WDR36:

>sp|Q8NI36|WDR36_HUMAN WD repeat-containing protein 36 OS=Homo sapiens GN=WDR36 PE=1 SV=1

MCCTEGSLRKRDSQRAPEAVLCLQLWQRTVPLDTLKGLGTCFPSGPELRG
AGIAAAMERASERRTASALFAGFRALGLFSNDIPHVVRFSALKRRFYVTTC
VGKSFHTYDVQKLSLVAVSNSVPQDICCMAADGRLVFAAYGNVFSAFARN
KEIVHTFKGHKAEIHFLQPFGDHIISVDTDGILIIWHIYSEEEYLQLTFDKSV
FKISAILHPSTYLNKILLGSEQGSLQLWNVKSNKLLYTFPGWKVGVTALQQ
APAVDVVAIGLMSGQVIIHNIKFNETLMKFRQDWGPITSISFRTDGHPVMA
AGSPCGHIGLWDLEDKKLINQMRNAHSTAIAGLTFLHREPLLVTNGADNA
LRIWIFDGPTGEGRLLRFRMGHSAPLTNIRYYGQNGQQILSASQDGTLQSF
STVHEKFNKSLGHGLINKKRVKRKGLQNTMSVRLPPITKFAAEEARESDW
DGIIACHQGKLSCSTWNYQKSTIGAYFLKPKELKKDDITATAVDITSCGNF
AVIGLSSGTVDVYNMQSGIHRGSFGKDQAHKGSVRGVAVDGLNQLTVTT
GSEGLLKFWNFKNKILIHSVSLSSSPNIMLLHRDSGILGLALDDFSISVLDIET
RKIVREFSGHQGQINDMAFSPDGRWLISAAMDCSIRTWDLPSGCLIDCFLL
DSAPLNVSMSPTGDFLATSHVDHLGIYLWSNISLYSVVSLRPLPADYVPSIV
MLPGTCQTQDVEVSEETVEPSDELIEYDSPEQLNEQLVTLSLLPESRWKNLL
NLDVIKKKNKPKEPPKVPKSAPFFIPTIPGLVPRYAAPEQNNDPQQSKVVNL
GVLAQKSDFCLKLEEGLVNNKYDTALNLLKESGPSGIETELRSLSPDCGGSI
EVMQSFLKMIGMMLDRKRDFELAQAYLALFLKLHLKMLPSEPVLLEEITN
LSSQVEENWTHLQSLFNQSMCILNYLKSALL

FASTA Sequence of the GPBS:

>1A0R:B|PDBID|CHAIN|SEQUENCE

XSELDQLRQEAEQLKNQIRDARKACADATLSQITNNIDPVGRIQMRTRRTL
RGHLAKIYAMHWGTDSRLLLSASQDGKLIIWDSYTTNKVHAIPLRSSWVM
TCAYAPSGNYVACGGLDNICSIYNLKTREGNVRVSRELAGHTGYLSCCRFL
DDNQIVTSSGDTTCALWDIETGQQTTTFTGHTGDVMSLSLAPDTRLFVSG
ACDASAKLWDVREGMCRQTFTGHESDINAICFFPNGNAFATGSDDATCR
LFDLRADQELMTYSHDNIICGITSVSFSKSGRLLLAGYDDFNCNVWDALK
ADRAGVLAGHDNRVSCLGVTDDGMAVATGSWDSFLKIWN

Sequences used for the Aggrescan analysis from the following PDB structures: 1TBG, 2TRC, 1ERJ, 1JV2, 2CE8, 1RI6, 3FGB, 3HXJ, 1DFC, 3C5M. Sequences that were less than 5 amino acids long were omitted for consistency.

A Strands	B Strands	C Strands	D Strands
IYAMHW	RLLVSA	KLIIWD	NKVHAIP
VVCCVK	RLLLSA	KLIIWD	SLVARLS
GFAVDF	EYLATG	TTQVYR	RCQPIEF
VYSLDW	RMFLLVG	QVLKCD	QKTHAIK
VYSLDW	RIVSAS	RLIVWN	NKEHALT
VLCMDW	NWIVSAS	KVIVWD	NKEHAVT
VLCMDW	RHIVSSS	SIRVYD	LKGHEGP
VLCMDW	RIVSSS	DNICSIYN	SRELA
HLCICD	RIVSSS	DNICSIYN	VMILQ
WVMTCA	LLFTG	DRLIRIWD	TVEYA
WVMTCA	KFLATG	GTCFLQD	SRMLT
YIRSVC	KILACA	SVCSIFS	SRILT
FGASVR	SVACGG	DSACSIFN	KRQVA
WVMTCA	QIVTSS	HSIKVWD	KKSVA
WVMACA	QIVTSS	TTCALWD	QQTTTF
WVMACA	KLVSGS	RTVRIWD	QCSLTL
ESICYN	RVLLGG	GQLISDQ	NNQLAT
LSCCRFL	HLITSS	QTCILWD	VFGGEF
LSCCRFL	RLITSS	STCAIWD	QRISIF
IYSLDYF	NLILTGS	GTCALWD	QLIQNF
GFSIDFT	QILTAS	KTIKVWD	ECKYTL
VSCCQYV	KYLFSG	ASAKLWD	RAVRTFH
VSSCQYV	RLFVSGA	RAVRVWD	MCRQTFT
MSCCTFL	RLFVSGA	GMVYIYD	RAVRTYH
LSACSFT	KYIAAGS	STARLWD	QCVQSFE

A Strands	B Strands	C Strands	D Strands
LSACSFT	DFVSGV	KKAMVWD	QCVQAFE
VHTVLLN	NWFISGS	GTCRLYD	RCNYTLK
VMSLSLA	DVFIGA	ATCRLYD	ELMTY
VMSLSLA	RFGTGS	FNCNVWD	CEVTY
VTTVAVS	RFGTGS	RGVLFWD	TTKLN
GYSVAVG	RlLLAG	NTCYVWD	QVCVY
VLSVSIS	EYILSG	YTINVWD	EVAIY
VQSVSIN	RLLFAG	NTIKIWD	RAGVLA

References

Adams, J., R. Kelso, et al. (2000). "The kelch repeat superfamily of proteins: propellers of cell function." Trends in cell biology **10**(1): 17-24.

Akpek, E. K. and J. D. Gottsch (2003). "Immune defense at the ocular surface." Eye **17**(8): 949-956.

Al-Lazikani, B., J. Jung, et al. (2001). "Protein structure prediction." Current Opinion in Chemical Biology **5**(1): 51-56.

Alberti, S., R. Halfmann, et al. (2009). "A systematic survey identifies prions and illuminates sequence features of prionogenic proteins." Cell **137**(1): 146-158.

Albinsson, B. and B. Norden (1992). "Excited-state properties of the indole chromophore: electronic transition moment directions from linear dichroism measurements: effect of methyl and methoxy substituents." The Journal of Physical Chemistry **96**(15): 6204-6212.

Alward, W. L. M., Y. H. Kwon, et al. (2003). "Evaluation of optineurin sequence variations in 1,048 patients with open-angle glaucoma." American Journal of Ophthalmology **136**(5): 904-910.

Anthony, N. R., D. G. Lynn, et al. (2012). "The Role of Interfaces in the Nucleation of Amyloid Nanotubes." Biophysical journal **102**(3, Supplement 1): 442a.

Balaratnasingam, C., W. H. Morgan, et al. (2009). "Heterogeneous Distribution of Axonal Cytoskeleton Proteins in the Human Optic Nerve." Investigative ophthalmology & visual science **50**(6): 2824-2838.

Balbach, J. J., Y. Ishii, et al. (2000). "Amyloid Fibril Formation by Aβ16-22, a Seven-Residue Fragment of the Alzheimer's β-Amyloid Peptide, and Structural Characterization by Solid State NMR†." Biochemistry **39**(45): 13748-13759.

Band, L. R., C. L. Hall, et al. (2009). "Intracellular Flow in Optic Nerve Axons: A Mechanism for Cell Death in Glaucoma." Investigative ophthalmology & visual science **50**(8): 3750-3758.

Bayer, A. U., O. N. Keller, et al. (1999). "Association of Glaucoma With Neurodegenerative Diseases With Apoptotic Cell Death: Alzheimer's Disease and Parkinson's Disease." Science: 135-137.

Bergenholtz, J. and N. J. Wagner (1996). "Formation of AOT/Brine Multilamellar Vesicles." Langmuir **12**(13): 3122-3126.

Bodén, M. and T. L. Bailey (2006). "Identifying sequence regions undergoing conformational change via predicted continuum secondary structure." Bioinformatics **22**(15): 1809-1814.

Bond, L. M., A. A. Peden, et al. (2011). "Myosin VI and its binding partner optineurin are involved in secretory vesicle fusion at the plasma membrane." Molecular Biology of the Cell **22**(1): 54-65.

Burns, J. N., S. D. Orwig, et al. (2010). "Rescue of Glaucoma-Causing Mutant Myocilin Thermal Stability by Chemical Chaperones." ACS Chemical Biology **5**(5): 477-487.

Carper, D. A., J. K. Sun, et al. (1999). "Oxidative stress induces differential gene expression in a human lens epithelial cell line." Investigative ophthalmology & visual science **40**(2): 400-406.

Carrell RW, L. D. L. (1997). "Conformational disease." Lancet **350**: 134-138.

Chaudhuri, I., J. Söding, et al. (2008). "Evolution of the beta-propeller fold." Proteins **71**(2): 795-803.

Chen, S., B. D. Spiegelberg, et al. (2004). "Interaction of Gβg with RACK1 and other WD40 repeat proteins." Journal of molecular and cellular cardiology **37**(2): 399-406.

Cheon, M., I. Chang, et al. (2007). "Structural reorganisation and potential toxicity of oligomeric species formed during the assembly of amyloid fibrils." PLoS computational biology **3**(9): 1727-1738.

Chesler, M. (2003). "Regulation and Modulation of pH in the Brain." Physiological Reviews **83**(4): 1183-1221.

Chi, Z.-L., F. Yasumoto, et al. (2010). "Mutant WDR36 directly affects axon growth of retinal ganglion cells leading to progressive retinal degeneration in mice." Human molecular genetics **19**(19): 3806-3815.

Chi, Z.-L., F. Yasumoto, et al. (2010). "Mutant WDR36 directly affects axon growth of retinal ganglion cells leading to progressive retinal degeneration in mice." Human molecular genetics **19**(19): 3806-3815.

Chien, P., A. H. DePace, et al. (2003). "Generation of prion transmission barriers by mutational control of amyloid conformations." Nature **424**(6951): 948-951.

Childers, W. S., A. K. Mehta, K. Lu, D. G. Lynn (2009). " Templating Molecular Arrays in Amyloid's Cross-Beta Grooves." J. Am. Chem. Soc. **131**: 10165-10172.

Childers, W. S., N. R. Anthony, et al. (2012). "Phase Networks of Cross-β Peptide Assemblies." Langmuir **28**(15): 6386-6395.

Childers, W. S., A. K. Mehta, et al. (2010). "Peptides organized as bilayer membranes." Angewandte Chemie (International ed. in English) **49**(24): 4104-4107.

Chiti, F. and C. M. Dobson (2009). "Amyloid formation by globular proteins under native conditions." Nat Chem Biol **5**(1): 15-22.

Chung, S. Y. and S. Subbiah (1996). "A structural explanation for the twilight zone of protein sequence homology." Structure **4**(10): 1123-1127.

Conchillo-Sole, O., N. de Groot, et al. (2007). "Aggrescan: a server for the prediction and evaluation of "hot spots" of aggregation in polypeptides." BMC Bioinformatics **8**(1): 65.

Conway, K. A., J. D. Harper, et al. (2000). "Fibrils Formed in Vitro from α-Synuclein and Two Mutant Forms Linked to Parkinson's Disease are Typical Amyloid†." Biochemistry **39**(10): 2552-2563.

Cruz, L., B. Urbanc, et al. (2005). "Solvent and mutation effects on the nucleation of amyloid β-protein folding." Proceedings of the National Academy of Sciences of the United States of America **102**(51): 18258-18263.

Decatur, S. M. (2006). "Elucidation of residue-level structure and dynamics of polypeptides via isotope-edited infrared spectroscopy." Accounts of chemical research **39**(3): 169-175.

Dong, J., J. M. Canfield, et al. (2007). "Engineering metal ion coordination to regulate amyloid fibril assembly and toxicity." Proceedings of the National Academy of Sciences of the United States of America **104**(33): 13313-13318.

Dong, J., K. Lu, et al. (2006). "Controlling amyloid growth in multiple dimensions." Amyloid : the international journal of experimental and clinical investigation : the official journal of the International Society of Amyloidosis **13**(4): 206-215.

Dong, J. J. M. C., Anil K. Mehta, Jacob E. Shokes, Bo Tian, W. Seth Childers, James A. Simmons, Zixu Mao, Robert A. Scott, Kurt Warncke, and David G. Lynn (2007). " Engineering metal ion coordination to regulate amyloid fibril assembly and toxicity." Proc. Nat. Acad. Sci. **104**(33): 13313-13318.

Dorsam, R. T. and J. S. Gutkind (2007). "G-protein-coupled receptors and cancer." Nat Rev Cancer **7**(2): 79-94.

Eanes, E. D. and G. G. Glenner (1968). "X-Ray Diffraction Studies on Amyloid Filaments." Journal of Histochemistry & Cytochemistry **16**(11): 673-677.

Eisele, Y. S., U. Obermüller, et al. (2010). "Peripherally applied Aβ-containing inoculates induce cerebral β-amyloidosis." Science (New York, N.Y.) **330**(6006): 980-982.

Elam, J. S., A. B. Taylor, et al. (2003). "Amyloid-like filaments and water-filled nanotubes formed by SOD1 mutant proteins linked to familial ALS." Nat Struct Mol Biol **10**(6): 461-467.

Engel, M. F. M., L. Khemtémourian, et al. (2008). "Membrane damage by human islet amyloid polypeptide through fibril growth at the membrane." Proceedings of the National Academy of Sciences **105**(16): 6033-6038.

Evers, F., C. Jeworrek, et al. (2009). "Elucidating the mechanism of lipid membrane-induced IAPP fibrillogenesis and its inhibition by the red wine compound resveratrol: a synchrotron X-ray reflectivity study." Journal of the American Chemical Society **131**(27): 9516-9521.

FarzadFard, F., N. Gharaei, et al. (2008). "β-Sheet capping: Signals that initiate and terminate β-sheet formation." Journal of structural biology **161**(1): 101-110.

Fautsch, M. P., A. M. Vrabel, et al. (2006). "The identification of myocilin-associated proteins in the human trabecular meshwork." Experimental eye research **82**(6): 1046-1052.

Fawzi, N. L., J. Ying, et al. (2010). "Kinetics of amyloid β monomer-to-oligomer exchange by NMR relaxation." Journal of the American Chemical Society **132**(29): 9948-9951.

Ferreira, S. T., M. N. N. Vieira, et al. (2007). "Soluble protein oligomers as emerging toxins in Alzheimer's and other amyloid diseases." IUBMB life **59**(4-5): 332-345.

Footz, T. K., J. L. Johnson, et al. (2009). "Glaucoma-associated WDR36 variants encode functional defects in a yeast model system." Human molecular genetics **18**(7): 1276-1287.

Friedberg, I. and H. Margalit (2002). "Persistently conserved positions in structurally similar, sequence dissimilar proteins: Roles in preserving protein fold and function." Protein Science **11**(2): 350-360.

Fülöp, V. and D. T. Jones (1999). "β propellers: structural rigidity and functional diversity." Current opinion in structural biology **9**(6): 715-721.

Fülöp, V. D. T. J. (1999). "β Propellers: structural rigidity and functional diversity." Current Opinion in Structural Biology **9**: 715-721.

Gettemans, J. K. M., Joël Vandekerckhove, and Veerle De Corte (2003). "A Kelch β Propeller Featuring as a Gβ Structural Mimic: Reinventing the Wheel?" Science's STKE **191**: 1-5.

Giacomelli, C. E. and W. Norde (2005). "Conformational changes of the amyloid β-peptide (1-40) adsorbed on solid surfaces." Macromolecular bioscience **5**(5): 401-407.

Gitter, B. D., L. N. Boggs, et al. (2000). "Regulation of Cytokine Secretion and Amyloid Precursor Protein Processing by Proinflammatory Amyloid Beta (Aβ)." Annals of the New York Academy of Sciences **917**(1): 154-164.

Glabe, C. (2001). "Intracellular mechanisms of amyloid accumulation and pathogenesis in Alzheimer's disease." Journal of Molecular Neuroscience **17**(2): 137-145.

Glabe, C. G. (2006). "Common mechanisms of amyloid oligomer pathogenesis in degenerative disease." Neurobiology of aging **27**(4): 570-575.

Glenner, G. G. and C. W. Wong (1984). "Alzheimer's disease: Initial report of the purification and characterization of a novel cerebrovascular amyloid protein." Biochemical and Biophysical Research Communications **120**(3): 885-890.

Goldstein, L. E., J. A. Muffat, et al. (2003). "Mechanisms of disease Cytosolic β-amyloid deposition and supranuclear cataracts in lenses from people with Alzheimer's disease." The Lancet **361**.

Guo, L. S., TE; Luong, V; Wood, N; Cheung, W; Maass, A; Ferrari, G; Russo-Marie, F; Sillito, AM; Cheetham, ME; Moss, SE; Fitzke, FW; Cordeiro, MF (2007). "Targeting amyloid-β in glaucoma treatment." Proc. Natl. Acad. Sci. U.S.A. **104**: 13444-13449.

Haass, C. and D. J. Selkoe (2007). "Soluble protein oligomers in neurodegeneration: lessons from the Alzheimer's amyloid β-peptide." Nature reviews. Molecular cell biology **8**(2): 101-112.

Halverson, K. J., I. Sucholeiki, et al. (1991). "Location of 8-Sheet-Forming Sequences in Amyloid Proteins." Macromolecules **130**(4): 6701-6703.

Harper, J. D. and P. T. Lansbury (1997). "Models Of Amyloid Seeding In Alzheimer's Disease And Scrapie:Mechanistic Truths and Physiological Consequences of the Time-Dependent Solubility of Amyloid Proteins." Annual review of biochemistry **66**(1): 385-407.

Hauser, M. a., R. R. Allingham, et al. (2006). "Distribution of WDR36 DNA sequence variants in patients with primary open-angle glaucoma." Investigative ophthalmology & visual science **47**(6): 2542-2546.

Hellstrand, E., B. Boland, et al. (2009). "Amyloid β-Protein Aggregation Produces Highly Reproducible Kinetic Data and Occurs by a Two-Phase Process." ACS Chemical Neuroscience **1**(1): 13-18.

Hewitt, A. W., D. P. Dimasi, et al. (2006). "A Glaucoma Case-control Study of the WDR36 Gene D658G Sequence Variant." American Journal of Ophthalmology **142**(2): 324-325.

Hills, R. D. and C. L. Brooks (2007). "Hydrophobic cooperativity as a mechanism for amyloid nucleation." Journal of molecular biology **368**(3): 894-901.

Hindo, S. S., A. M. Mancino, et al. (2009). "Small molecule modulators of copper-induced Aβ aggregation." Journal of the American Chemical Society **131**(46): 16663-16665.

Hoffmann, H., C. Thunig, et al. (1994). "Surfactant Systems with Charged Multilamellar Vesicles and Their Rheological Properties." Langmuir **10**(11): 3972-3981.

Hope, M. J., M. B. Bally, et al. (1985). "Production of large unilamellar vesicles by a rapid extrusion procedure: characterization of size distribution, trapped volume and ability to maintain a membrane potential." Biochim Biophys Acta **812**(1): 55-65.

Höppener, J. W. M., B. Ahrén, et al. (2000). "Islet Amyloid and Type 2 Diabetes Mellitus." New England Journal of Medicine **343**(6): 411-419.

Hull, R. L., G. T. Westermark, et al. (2004). "Islet Amyloid: A Critical Entity in the Pathogenesis of Type 2 Diabetes." Journal of Clinical Endocrinology & Metabolism **89**(8): 3629-3643.

Ishii, T., S. Haga, et al. (1975). "Identification of components of immunoglobulins in senile plaques by means of fluorescent antibody technique." Acta Neuropathologica **32**(2): 157-162.

Iwatsubo, T., A. Odaka, et al. (1994). "Visualization of Aβ42(43) and Aβ40 in senile plaques with end-specific Aβ monoclonals: Evidence that an initially deposited species is Aβ42(43)." Neuron **13**(1): 45-53.

Jacobson, N., M. Andrews, et al. (2001). "Non-secretion of mutant proteins of the glaucoma gene myocilin in cultured trabecular meshwork cells and in aqueous humor." Human molecular genetics **10**(2): 117-125.

Jones, D. T. (1999). "Protein secondary structure prediction based on position-specific scoring matrices." Journal of molecular biology **292**(2): 195-202.

Jordan, I. K., F. A. Kondrashov, et al. (2005). "A universal trend of amino acid gain and loss in protein evolution." Nature **433**(7026): 633-638.

Jorgensen, N. D., Y. Peng, et al. (2009). "The WD40 domain is required for LRRK2 neurotoxicity." PloS one **4**(12): e8463-e8463.

Jousma, H., H. Talsma, et al. (1987). "Characterization of liposomes. The influence of extrusion of multilamellar vesicles through polycarbonate membranes on particle size, particle size distribution and number of bilayers." International Journal of Pharmaceutics **35**(3): 263-274.

Juhász, T., Z. Szeltner, et al. (2005). "Unclosed β-propellers display stable structures: implications for substrate access to the active site of prolyl oligopeptidase." Journal of molecular biology **346**(3): 907-917.

Kayed, R., E. Head, et al. (2003). "Common structure of soluble amyloid oligomers implies common mechanism of pathogenesis." Science (New York, N.Y.) **300**(5618): 486-489.

Khakshoor, O., B. Demeler, et al. (2007). "Macrocyclic β-Sheet Peptides That Mimic Protein Quaternary Structure through Intermolecular β-Sheet Interactions." Journal of the American Chemical Society **129**(17): 5558-5569.

Kim, H. C., S; Lee, D; Chromy, B; Lee, SC; Park, Y; Klein, WL; Krafft, GA; Hong, S (2003). "Selective neuronal degeneration induced by soluble oligomeric amyloid β protein." The FASEB Journal **17**(1): 118-120.

Klabunde, T. and G. Hessler (2002). "Drug Design Strategies for Targeting G-Protein-Coupled Receptors." ChemBioChem **3**(10): 928-944.

Kolde, G., R. Bachus, et al. (1996). "Skin involvement in amyotrophic lateral sclerosis." The Lancet **347**(9010): 1226-1227.

Kumar, S. W., Jochen (2011). "Phosphorylation of amyloid beta (Aβ) peptides – A trigger for formation of toxic aggregates in Alzheimer's disease." Aging **3**(8): 803-812.

Kwon, Y. H., J. H. Fingert, et al. (2009). "Primary open-angle glaucoma." The New England journal of medicine **360**(11): 1113-1124.

Laganowsky, a., C. Liu, et al. (2012). "Atomic View of a Toxic Amyloid Small Oligomer." Science **335**(6073): 1228-1231.

Lagerstrom, M. C. and H. B. Schioth (2008). "Structural diversity of G protein-coupled receptors and significance for drug discovery." Nat Rev Drug Discov **7**(4): 339-357.

Langer, F., Y. S. Eisele, et al. (2011). "Soluble Aβ Seeds Are Potent Inducers of Cerebral β-Amyloid Deposition." The Journal of Neuroscience **31**(41): 14488-14495.

Lassen, N., W. J. Black, et al. (2008). "The role of corneal crystallins in the cellular defense mechanisms against oxidative stress." Seminars in Cell & Developmental Biology **19**(2): 100-112.

Lazo, N. D., M. A. Grant, et al. (2005). "On the nucleation of amyloid β-protein monomer folding." Protein Science: 1581-1596.

Lee, H. G., X. Zhu, et al. (2006). "Amyloid β: the alternate hypothesis." Current Alzheimer research **3**(1): 75-80.

Lei, G. and R. C. MacDonald (2003). "Lipid bilayer vesicle fusion: intermediates captured by high-speed microfluorescence spectroscopy." Biophysical journal **85**(3): 1585-1599.

Liang, Y., P. Guo, et al. (2008). "Light harvesting antenna on an amyloid scaffold." Chemical communications (Cambridge, England)(48): 6522-6524.

Liang, Y., P. Guo, et al. (2008). "Light harvesting antenna on an amyloid scaffold." Chemical Communications(48): 6522-6524.

Liang, Y., D. G. Lynn, et al. (2010). "Direct Observation of Nucleation and Growth in Amyloid Self-Assembly." Journal of the American Chemical Society **132**(18): 6306-6308.

Liang, Y., D. G. Lynn, et al. (2010). "Direct observation of nucleation and growth in amyloid self-assembly." Journal of the American Chemical Society **132**(18): 6306-6308.

Liang, Y., S. V. Pingali, et al. (2008). "Cross-Strand Pairing and Amyloid Assembly." Biochemistry **47**(38): 10018-10026.

Liang, Y., S. V. Pingali, et al. (2008). "Cross-strand pairing and amyloid assembly." Biochemistry **47**(38): 10018-10026.

Libby, R. T., D. B. Gould, et al. (2005). "Complex Genetics of Glaucoma Susceptibility." Annual Review of Genomics and Human Genetics **6**(1): 15-44.

Linse, S., C. Cabaleiro-Lago, et al. (2007). "Nucleation of protein fibrillation by nanoparticles." Proceedings of the National Academy of Sciences of the United States of America **104**(21): 8691-8696.

Liu, C., M. R. Sawaya, et al. (2011). "Characteristics of Amyloid-Related Oligomers Revealed by Crystal Structures of Macrocyclic β-Sheet Mimics." Journal of the American Chemical Society **133**(17): 6736-6744.

Lomakin, a. (1996). "On the nucleation and growth of amyloid β-protein fibrils: Detection of nuclei and quantitation of rate constants." Proceedings of the National Academy of Sciences **93**(3): 1125-1129.

Lu, K., J. Jacob, et al. (2003). "Exploiting amyloid fibril lamination for nanotube self-assembly." Journal of the American Chemical Society **125**(21): 6391-6393.

Mao, G. L., X. (2005). Resolving the Thickness and Micromechanical Properties of Lipid Bilayers and Vesicles Using AFM, John Wiley & Sons, Inc.**:** 181-200.

Marinissen, M. J. and J. S. Gutkind (2001). "G-protein-coupled receptors and signaling networks: emerging paradigms." Trends in pharmacological sciences **22**(7): 368-376.

Markesbery, W. R. (1997). "Oxidative stress hypothesis in Alzheimer's disease." Free radical biology & medicine **23**(1): 134-147.

Masters, C. S., G; Weinman, NA; Multhaup, G; McDonald, BL; Beyreuther, K (1985). "Amyloid plaque core protein in Alzheimer disease and Down syndrome." Proc Natl Acad Sci U S A. **82**(12): 4245–4249.

Mayer, L. D., M. J. Hope, et al. (1986). "Vesicles of variable sizes produced by a rapid extrusion procedure." Biochimica et Biophysica Acta (BBA) - Biomembranes **858**(1): 161-168.

McGowan, D. P., W. van Roon-Mom, et al. (2000). "Amyloid-like inclusions in Huntington's disease." Neuroscience **100**(4): 677-680.

McGuffin, L. J., K. Bryson, et al. (2000). "The PSIPRED protein structure prediction server." Bioinformatics **16**(4): 404-405.

Meda, L., P. Baron, et al. (1999). "Proinflammatory profile of cytokine production by human monocytes and murine microglia stimulated with β-amyloid[25–35]." Journal of Neuroimmunology **93**(1–2): 45-52.

Mehta, A. K., K. Lu, et al. (2008). "Facial symmetry in protein self-assembly." Journal of the American Chemical Society **130**(30): 9829-9835.

Meyer-Luehmann, M., J. Coomaraswamy, et al. (2006). "Exogenous Induction of Cerebral ß-Amyloidogenesis Is Governed by Agent and Host." Science **313**(5794): 1781-1784.

Miller, D. L., I. A. Papayannopoulos, et al. (1993). "Peptide compositions of the cerebrovascular and senile plaque core amyloid deposits of Alzheimer's disease." Archives of biochemistry and biophysics **301**(1): 41-52.

Miyazawa, A., N. Fuse, et al. (2007). "Association between primary open-angle glaucoma and WDR36 DNA sequence variants in Japanese." Mol Vis **13**: 1912-1919.

Monemi, S., G. Spaeth, et al. (2005). "Identification of a novel adult-onset primary open-angle glaucoma (POAG) gene on 5q22.1." Human Molecular Genetics **14**(6): 725-733.

Nagy, I. (2003). "Expression and characterization of the olfactomedin domain of human myocilin." Biochemical and Biophysical Research Communications **302**(3): 554-561.

Nakano, M., Y. Ikeda, et al. (2009). "Three susceptible loci associated with primary open-angle glaucoma identified by genome-wide association study in a Japanese population." Proceedings of the National Academy of Sciences **106**(31): 12838-12842.

Nelson, G. a., D. P. Edward, et al. (1999). "Ocular amyloidosis and secondary glaucoma." Ophthalmology **106**(7): 1363-1366.

Nelson, R., M. R. Sawaya, et al. (2005). "Structure of the cross-β spine of amyloid-like fibrils." Nature **435**(7043): 773-778.

Ni, R., W. S. Childers, et al. (2012). "Remodeling Cross-β Nanotube Surfaces with Peptide/Lipid Chimeras." Angewandte Chemie International Edition **51**(27): 6635-6638.

NIH Diagram of Healthy Eye. NEA11. National Eye Institute Website, National Institutes of Health. **2.1MB:** A clear fluid flows continuously in and out of the anterior chamber and nourishes nearby tissues. The fluid leaves the chamber at the open angle where the cornea and iris meet. When the fluid reaches the angle, it flows through a spongy meshwork and leaves the eye.

Nikkhah, M., Z. Jawad-Alami, et al. (2006). "Engineering of β-propeller protein scaffolds by multiple gene duplication and fusion of an idealized WD repeat." Biomolecular engineering **23**(4): 185-194.

Park, B.-C., M. Tibudan, et al. (2007). "Interaction between two glaucoma genes, optineurin and myocilin." Genes to Cells **12**(8): 969-979.

Petty, S. a. and S. M. Decatur (2005). "Experimental evidence for the reorganization of β-strands within aggregates of the Aβ(16-22) peptide." Journal of the American Chemical Society **127**(39): 13488-13489.

Podlisny, M. B., D. T. Stephenson, et al. (1992). "Synthetic amyloid β-protein fails to produce specific neurotoxicity in monkey cerebral cortex." Neurobiology of aging **13**(5): 561-567.

Prelli, F., E. Castano, et al. (1988). "Differences Between Vascular and Plaque Core Amyloid in Alzheimer's Disease." Journal of Neurochemistry **51**(2): 648-651.

Rezaie, T., A. Child, et al. (2002). "Adult-Onset Primary Open-Angle Glaucoma Caused by Mutations in Optineurin." Science **295**(5557): 1077-1079.

Richardson, J. S. and D. C. Richardson (2002). "Natural β-sheet proteins use negative design to avoid edge-to-edge aggregation." Proceedings of the National Academy of Sciences **99**(5): 2754-2759.

Rohl, C. A., C. E. M. Strauss, et al. (2004). Protein Structure Prediction Using Rosetta. Methods in enzymology. B. Ludwig and L. J. Michael, Academic Press. **Volume 383:** 66-93.

Ryu, J., K. Girigoswami, et al. (2008). "Influence of multiple metal ions on β-amyloid aggregation and dissociation on a solid surface." Biochemistry **47**(19): 5328-5335.

Sakono, M. and T. Zako (2010). "Amyloid oligomers: formation and toxicity of Aβ oligomers." FEBS Journal **277**(6): 1348-1358.

Šali, A., L. Potterton, et al. (1995). "Evaluation of comparative protein modeling by MODELLER." Proteins: Structure, Function, and Bioinformatics **23**(3): 318-326.

Santoso, A., P. Chien, et al. (2000). "Molecular basis of a yeast prion species barrier." Cell **100**(2): 277-288.

Scherzinger, E., A. Sittler, et al. (1999). "Self-assembly of polyglutamine-containing huntingtin fragments into amyloid-like fibrils: Implications for Huntington's disease pathology." Proceedings of the National Academy of Sciences **96**(8): 4604-4609.

Schuetz, A., A. Allali-Hassani, et al. (2006). "Structural basis for molecular recognition and presentation of histone H3 by WDR5." The EMBO journal **25**(18): 4245-4252.

Shamsi, F. A., I. A. Chaudhry, et al. (2007). "L-Carnitine Protects Human Retinal Pigment Epithelial Cells from Oxidative Damage." Current Eye Research **32**(6): 575-584.

Shorter, J., Lindquist, S. (2005). "Prions as adaptive conduits of memory and inheritance." Nat Rev Gen **6**: 435-450.

Skarie, J. M. and B. A. Link (2008). "The Primary open-angle glaucoma gene WDR36 functions in ribosomal RNA processing and interacts with the p53 stress–response pathway." Human molecular genetics **17**(16): 2474-2485.

Söding, J., A. Biegert, et al. (2005). "The HHpred interactive server for protein homology detection and structure prediction." Nucleic Acids Research **33**(suppl 2): W244-W248.

Soto, C. (2003). "Unfolding the role of protein misfolding in neurodegenerative diseases." Nature reviews. Neuroscience **4**(1): 49-60.

Springer, T. a. (2002). "Predicted and experimental structures of integrins and β-propellers." Current opinion in structural biology **12**(6): 802-813.

Stine, W. B., K. N. Dahlgren, et al. (2003). "*In Vitro* Characterization of Conditions for Amyloid-β Peptide Oligomerization and Fibrillogenesis." Journal of Biological Chemistry **278**(13): 11612-11622.

Stone, E. M., J. H. Fingert, et al. (1997). "Identification of a Gene That Causes Primary Open Angle Glaucoma." Science **275**(5300): 668-670.

Strohmeyer, R. and J. Rogers (2001). "Molecular and cellular mediators of Alzheimer's disease inflammation." Journal of Alzheimer's Disease **3**(1): 131-157.

Sunde, M., L. C. Serpell, et al. (1997). "Common core structure of amyloid fibrils by synchrotron X-ray diffraction." Journal of molecular biology **273**(3): 729-739.

Surguchev, A. and A. Surguchov (2010). "Conformational diseases: looking into the eyes." Brain research bulletin **81**(1): 12-24.

Tamm, E. R. (2002). "Myocilin and glaucoma: facts and ideas." Progress in retinal and eye research **21**(4): 395-428.

Valeyev, N. V., A. K. Downing, et al. (2008). "Electrostatic and functional analysis of the seven-bladed WD β-propellers." Evol Bioinform Online **4**: 203-216.

van Nocker, S. P. L. (2003). "The WD-repeat protein superfamily in Arabidopsis: conservation and divergence in structure and function." BMC Genomics **4**(50).

Verdier, Y., M. Zarándi, et al. (2004). "Amyloid β-peptide interactions with neuronal and glial cell plasma membrane: binding sites and implications for Alzheimer's disease." Journal of Peptide Science **10**(5): 229-248.

Viard, M., J. Gallay, et al. (2001). "Origin of laurdan sensitivity to the vesicle-to-micelle transition of phospholipid-octylglucoside system: a time-resolved fluorescence study." Biophysical journal **80**(1): 347-359.

Wang, X., Y. Huang, et al. (2008). "Structural-symmetry-related sequence patterns of the proteins of β-propeller family." Journal of molecular graphics & modelling **26**(5): 829-833.

Wirths, O., G. Multhaup, et al. (2004). "A modified β-amyloid hypothesis: intraneuronal accumulation of the β-amyloid peptide – the first step of a fatal cascade." Journal of Neurochemistry **91**(3): 513-520.

Witarto, a. B. and K. Sode (2001). "Increasing the hydrophobic interaction between terminal W-motifs enhances the stability of Salmonella typhimurium sialidase. A general strategy for the stabilization of beta-propeller protein fold." Protein engineering **14**(11): 891-896.

Wormell, R. (1954). New fibres from proteins., Academic Press**:** 106.

Wu, C., M. T. Bowers, et al. (2010). "Molecular Structures of Quiescently Grown and Brain-Derived Polymorphic Fibrils of the Alzheimer Amyloid Aβ(9-40) Peptide: A Comparison to Agitated Fibrils." PLoS Comput Biol **6**(3): e1000693.

Wu, X.-H., R.-C. Chen, et al. (2010). "The Effect of Asp-His-Ser/Thr-Trp Tetrad on the Thermostability of WD40-Repeat Proteins." Biochemistry **49**(47): 10237-10245.

Wu, X.-H., H. Zhang, et al. (2010). "Is Asp-His-Ser/Thr-Trp tetrad hydrogen-bond network important to WD40-repeat proteins: A statistical and theoretical study." Proteins: Structure, Function, and Bioinformatics **78**(5): 1186-1194.

Wurth, C., N. K. Guimard, et al. (2002). "Mutations that Reduce Aggregation of the Alzheimer's Aβ42 Peptide: an Unbiased Search for the Sequence Determinants of Aβ Amyloidogenesis." Journal of molecular biology **319**(5): 1279-1290.

Yadid, I. and D. S. Tawfik (2007). "Reconstruction of functional β-propeller lectins via homo-oligomeric assembly of shorter fragments." Journal of molecular biology **365**(1): 10-17.

Yadid, I. and D. S. Tawfik (2011). "Functional β-propeller lectins by tandem duplications of repetitive units." Protein engineering, design & selection : PEDS **24**(1-2): 185-195.

Yin, H., L. Chen, et al. (2008). "Soluble amyloid β oligomers may contribute to apoptosis of retinal ganglion cells in glaucoma." Medical hypotheses **71**(1): 77-80.

Yin, H. C., L.; Chen X., Liu, X. (2008). "Soluble amyloid beta oligomers may contribute to apoptosis of retinal ganglion cells in glaucoma." Medical Hypotheses **71**: 77-80.

Zheng, J., C. Liu, et al. (2011). "Macrocyclic β-Sheet Peptides That Inhibit the Aggregation of a Tau-Protein-Derived Hexapeptide." Journal of the American Chemical Society **133**(9): 3144-3157.